Master Thesis, Department of Geosciences

Experimental study on CO_2 monitoring and saturation with combined acoustic velocity and electrical resistivity in sandstone reservoirs

Omolo, Lamech Omondi

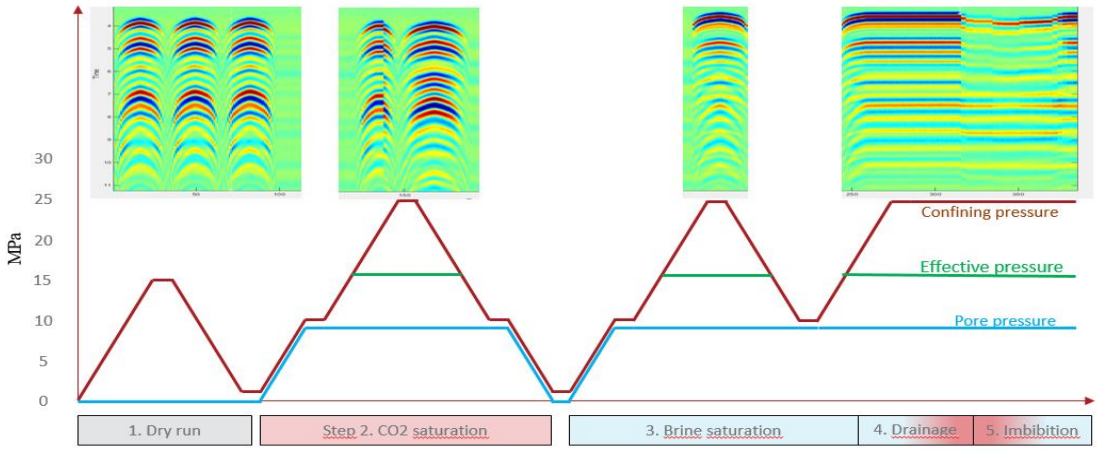

UNIVERSITY OF OSLO
FACULTY OF MATHEMATICS AND NATURAL SCIENCES

Experimental study on CO_2 monitoring and saturation with combined acoustic velocity and electrical resistivity in sandstone reservoirs

Omolo, Lamech Omondi

Master Thesis in Geosciences
Discipline: Environmental Geology and Geohazard
Department of Geosciences

Faculty of Mathematics and Natural Sciences

University of Oslo

June 2015

© Omolo, Lamech Omondi, 2015

This work is published digitally through DUO – Digitale Utgivelser ved UiO

http://www.duo.uio.no

It is also catalogued in BIBSYS (http://www.bibsys.no/english)

All rights reserved. No part of this publication may be reproduced or transmitted, in any form or by any means, without permission.

Preface

This thesis is part of the FME (Centre for Environment-friendly Energy Research) Centre name SUCCESS (SUbsurface CO_2 storage-Critical Element and Superior Strategy). The research was conducted at the Department of Geosciences, University of Oslo in close collaboration with Norwegian Geotechnical Institute (NGI) under Petroleum Geomechanics and Geophysics (PGG) Division during the period September 2014 to May 2015 under the supervision of Dr. Nazmul Haque Mondol (Associate professor at UiO and Advisor, adjunct position at PGG, NGI) and Dr. Øistein Johnsen (Senior Researcher at Polytec – formerly at PGG, NGI).

Acknowledgements

I am eternally grateful to God for the gift of life!

I am forever grateful to my supervisors Nazmul Haque Mondol and Øistein Johnsen for their patience, support, endless enthusiasm, guidance and friendship throughout the duration of this project. Thanks to the Petroleum Geomechanic and Geophysics (PGG) Division at NGI especially Magnus and Heidi for their help in the laboratory, Joonsang, and Guillaume for the discussions.

I wish to express my special gratitude to Oluwakemi Yetunde Ogulebo and Mohammed Koochak Zadeh for their suggestions and critics for further improvement on my thesis. My sincere thanks to my colleague Tran Truong with whom we spent several hours in the NGI laboratory to meet the deadline and for the discussions we had. All my helpful and caring friends and classmates deserve special thanks for their emotional supports.

I am thankful beyond words for the support and wishes from my parents and family members.

I would like to dedicate this work to Sofie whose hard work and sacrifice kept me going.

Abstract

CO_2 storage is considered as one of the most promising solutions to overcome global increase in temperature. In order to ensure the safety of the sequestrated CO_2, several geophysical monitoring methods are required, among them electrical resistivity and seismic velocity which depends on porosity, texture, mineralogy and fluid saturation. However, seismic data seldom allow us to estimate saturation accurately in geological reservoirs. On the other hand, resistivity is very sensitive to porosity and help to calculate fluid saturation. A combined use of both electrical resistivity and seismic velocity enables two complementary measurements: Seismic velocity measurement, which has better resolution efficiency in fluid mapping in geological reservoirs compared to electrical resistivity while the latter has a better precision in terms of quantifying relative saturation levels of immiscible fluids. The main challenge is to combine these two data sources to monitor CO_2 storage where water saturation varies due to CO_2 injection.

Using an advanced experimental setup, a series of laboratory experiments have been carried out to monitor P-wave velocity and resistivity simultaneously in selected porous sandstones during liquid CO_2 injection. The sandstones studied are medium to fine grained Red Wildmoor (RW) and medium grained Berea. For the Red Wildmoor, two core plugs: one drilled perpendicular and the other drilled parallel to the layering were used. There experiments were conducted by simulating the reservoir conditions at depth of about 1000 m. A constant pore pressure of 10 MPa and confining pressure of 25 MPa were maintained throughout the flooding of liquid CO_2. Prior to CO_2 flooding, the sandstone core plugs were saturated with CO_2 and brine. Multidirectional acoustic velocity and resistivity measurements were then taken during drainage and imbibition processes. The laboratory results were compared with Gassmann's model based on CO_2 saturation estimated by Resistivity Index (RI) assuming that the samples were brine saturated prior to CO_2 injection.

The results show that resistivity increased throughout the injection process and the P-wave velocity decreased drastically after the start of CO_2 injection. It is observed that the layering of core plugs influenced the fluid distribution pattern and saturation level. The observed velocities are in good agreement with predicted velocities using the Gassmann Fluid Substitution Model with the exception of the Berea sandstone. By comparing the velocity-saturation relation estimated by Gassmann and RI models, P-wave velocities becomes less sensitive after injecting 2 PV CO_2 for vertical Red Wildmoor, 1 PV for horizontal Red Wildmoor and 0.4 PV for Berea while resistivity kept increasing with increase in CO_2 saturation. The study shows that electrical resistivity measurements can efficiently track the development of CO_2 front during injection and effectively complement the difficulty of P-wave velocity on quantifying the stored CO_2.

Table of Contents

List of figures

List of tables

Chapter 1: Introduction

1.1 Background and motivation

Carbon Capture and Storage (CCS) is gradually becoming an important technology to reduce greenhouse gas emission, in addition to other options like use of renewable energy, nuclear energy and energy efficiency improvement. Several studies have been carried out to find the best subsurface geological storages in which the injected volume of CO_2 can be safely stored for hundred or even thousands of years. Some of these geological storages include depleted oil and gas reservoirs, deep saline aquifer and deep coal deposits. According to Chadwick et al. (2004) and Holt et al. (1995a) deep saline aquifer offers the largest storage potential of all geological CO_2 storage options and are widely distributed throughout the globe in sedimentary basins (Fig. 1.1). Given the wide range of temperature and pressure conditions in the sedimentary basins, CO_2 can be stored as a gas, liquid, or supercritical fluid.

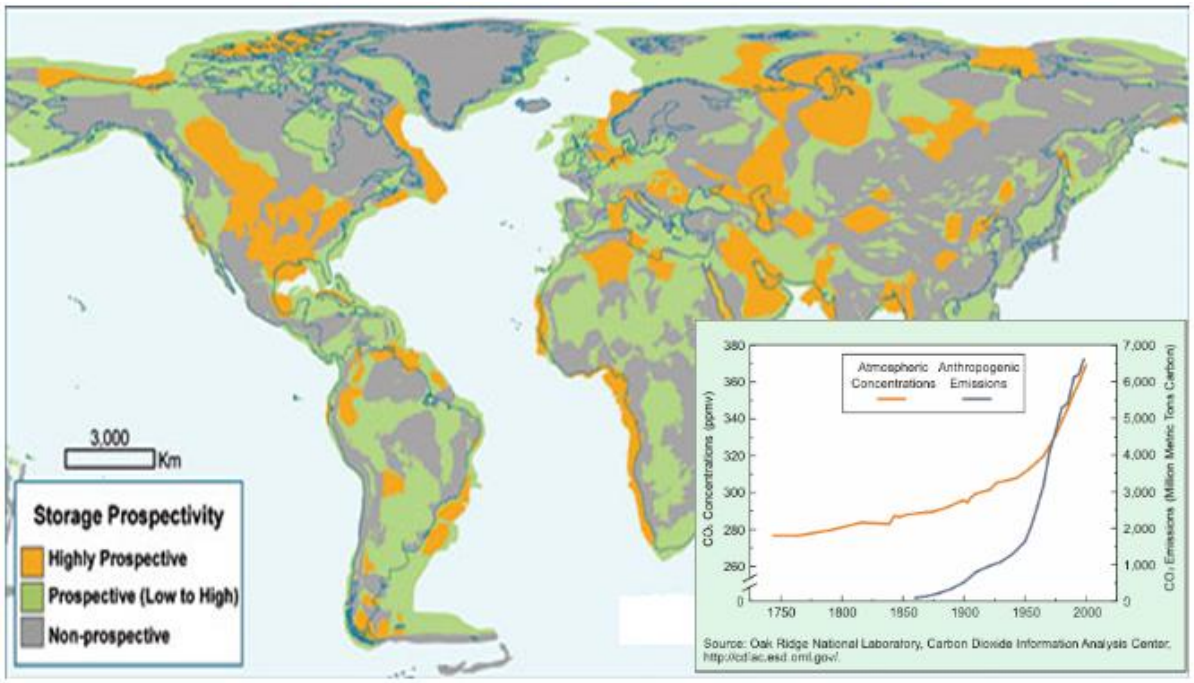

Figure 1.1 Prospective areas in sedimenatry basins where suitable saline formations, depleted oil and gas fields and coal beds may be found. The figure is based on partial data and could change from time to time (Courtesy of Geoscience Australia). Inset figure; atmospheric concentrations and anthropogenic emissions of CO_2 from 1750 to 2000 (source: IPCC, 2005).

For efficient injection and storage, CO_2 should be pumped into geological storage reservoirs greater than 800 m depth (Huppert and Neufeld, 2014). According to Bachu et al. (1994), these depths ensures that the CO_2 is stored in supercritical conditions which is denser than the gaseous, hence more CO_2 per volume is stored. The overall, general CCS process involves three elements:

1) **Capture:** Preferably, CO_2 is captured from large static point sources. Large power stations generate the bulk of all CO_2 emissions. The capture of CO_2

can be divided into three main categories (Feron and Hendriks, 2005; IPCC, 2005); *post combustion, pre-combustion* and *oxyfuel* combustion.

2) **Transport:** CO_2 can be transported by ship, pipeline and road. According to IEA (International Energy Agency), the most favourable means depends on distance, amount of CO_2, period and storage location.
3) **Storage:** There are several geological formations for storing CO_2 underground. Among them depleted oil and gas reservoirs (Gorgon, Australia) to enhance oil and gas recovery (Cranfield, USA), coal bed seams (IEA Greenhouse Gas R&D Programme), shallow (Sleipner, offshore Norway) and deep (Ketzin, Germany) saline aquifers, and salt caverns (Klaus et al., 2008; Nalinee and Martin, 2011).

According to IPCC (2005) anthropogenic CO_2 emissions is the major cause for the rise in global temperature with its main source being fossil fuel combustion in the power generation, industrial, residential and transport sectors (Bachu and Adams, 2003; Li et al., 2006). The engineered injection of CO_2 into subsurface geological formation was first undertaken in Texas, USA, in the early 1970's, as part of enhanced oil recovery (EOR) projects. In a little over a decade, geological storage of CO_2 has grown from a concept of limited interest to one that is quite widely regarded as potentially important mitigation option. There are several reasons for this. First, as research has progressed and as demonstration and commercial projects has been successfully undertaken, the level of confidence in the technology has increased. Second, there is consensus that broad portfolios of mitigation options are needed. The first commercial application of CO_2 storage in an offshore saline aquifer has been operational at the Sleipner gas field, Norway since 1996. There are also some pilot scale CO_2 sequestration tests such as the K12B (Netherlands, gas reservoir, started in 2004), Otway (Australia, gas reservoir, 2006), RECOPOL (Poland, coal seam, 2004) and Hokkaido (Japan, enhanced coal bed methane, 2004). To realize this potential, the technique must be safe, environmentally sustainable, cost-effective and capable of being broadly applied.

For efficient and safe storage of CO_2, it is necessary to monitor the CO_2 distribution and migration behaviour for risk assessment and to quantify the CO_2 volume in a reservoir. In most CO_2 storage sites, seismic survey has been conducted to monitor injected CO_2 among them Sleipner and Weyburn (Arts et al., 2004; Davis, 2003) where seismic data show great results for monitoring the distribution and migration of injected CO_2 in the reservoirs. At Nagaoka pilot site, time-lapse well logging was used to monitor the behaviour of injected CO_2 in supercritical condition (Xue et al., 2006). Crosswell seismic and EM surveys have been successfully applied to map the movement of injected CO_2 at the Nagaoka and Frio pilot sites (Daley et al., 2008; Saito et al., 2006).

This study focusses on electrical resistivity and acoustic velocity as a means of monitoring and assessing the effect of CO_2 injection into saline formation. Electrical resistivity in this context depends on the resistance to the flow of electric current in pore fluid, connectivity of the pore spaces in addition to the bulk porosity while acoustic velocity measurement during CO_2 injection in the reservoir is primarily controlled by bulk property of solid fraction and fluid phase (Peter et al., 1993). A combination of both electrical resistivity and seismic velocity measurements enables two complementary measurements: Seismic velocity measurement, which has better resolution efficiency in fluid mapping in geological reservoirs compared to electrical resistivity while the latter has a better precision in terms of quantifying relative saturation levels of immiscible fluids (Nakatsuka et al., 2010; Xue et al., 2009).

1.2 Aim and objectives

The aim of this thesis is to run experiments where we can study the effect of sub-core scale heterogeneities on the fluid distribution pattern and influence of injected CO_2 on acoustic velocity and electrical resistivity in sandstone reservoirs. The experimental setup allows us to measure axial and radial resistivity and acoustic velocity simultaneously. The data acquired in this study help to investigate:

- Relationship between experimental results and theoretical predictions
- Effect of fluid flow rate on CO_2 saturation level and
- Relationship between P-wave velocity and CO_2 saturation

1.3 Database and softwares

Two well-known sandstones (Red Wildmoor from UK and Berea from Western Pennsylvania, USA) were used to perform the laboratory experiments. The Red Wildmoor sandstone sample was drilled in two directions; perpendicular and parallel to the bedding plane. Both Berea and Red Wildmoor sandstones have been used for many core-flooding experiments to characterize the oil production sandstone reservoirs during primary, secondary and tertiary phases (Baudracco and Aoubouazza, 1995; Dawson et al.; Han et al., 2015; Moghadam et al., 2014; Shi et al., 2011). Several popular softwares (e.g. Microsoft excel, MATLAB, PSWaves (Fig 1.2) etc.) were utilized in different phases of data acquisition, processing and interpretation.

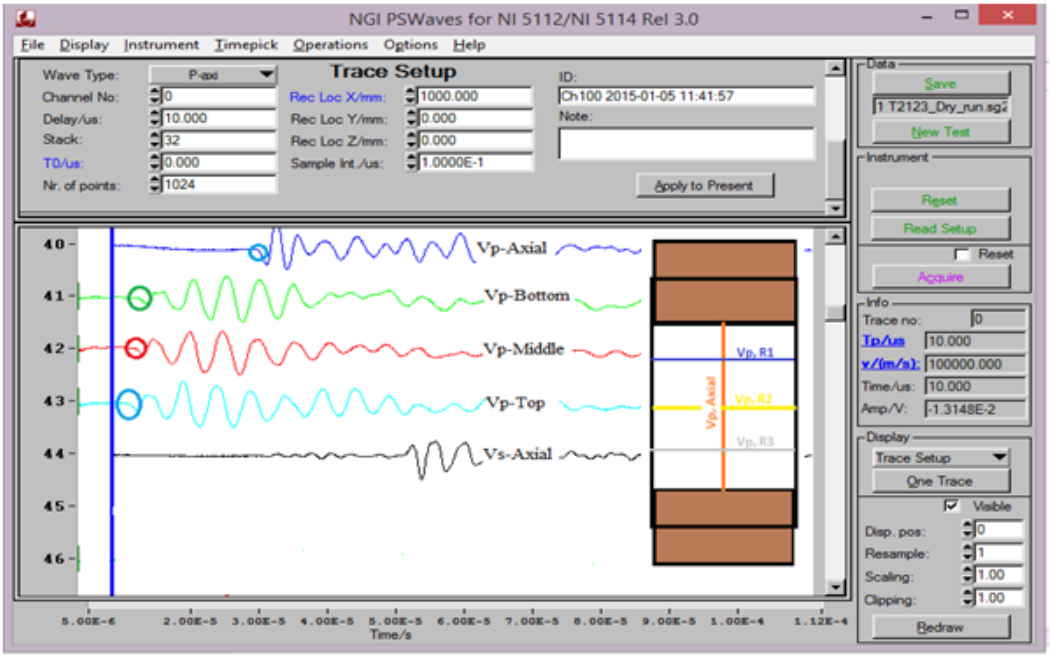

Figure 1.2 PSWaves software for recording Vp and Vs and also determining the first wave arrival (Courtesy of NGI). The circles shows the arrival of different wave forms. From top, Vp-axial, bottom, middle and top Vp-axials and Vs-axial. Inset figure represents a sketch of configuration of velocity measurements.

In order to determine the P- and S-wave first arrivals, we utilized Matlab code written by NGI to produce a text (.txt) file. This was then imported and read into Microsoft excel then dates were correlated to the mechanical data file output obtained for each test. The same procedure was followed for resistivity measurements. Figure 1.3 shows a screenshot from the Matlab Variable Density Log (VDL) plot. VDL is a presentation of acoustic waveform at a receiver of an ultrasonic measurement, in which the amplitude is presented in colour or the shades of a grey scale. The first seismic image represents three loading unloading cycles of dry (Pp = 0 MPa), CO_2 and brine-saturated conditions. The fourth image represents CO_2 drainage and brine imbibition scenarios.

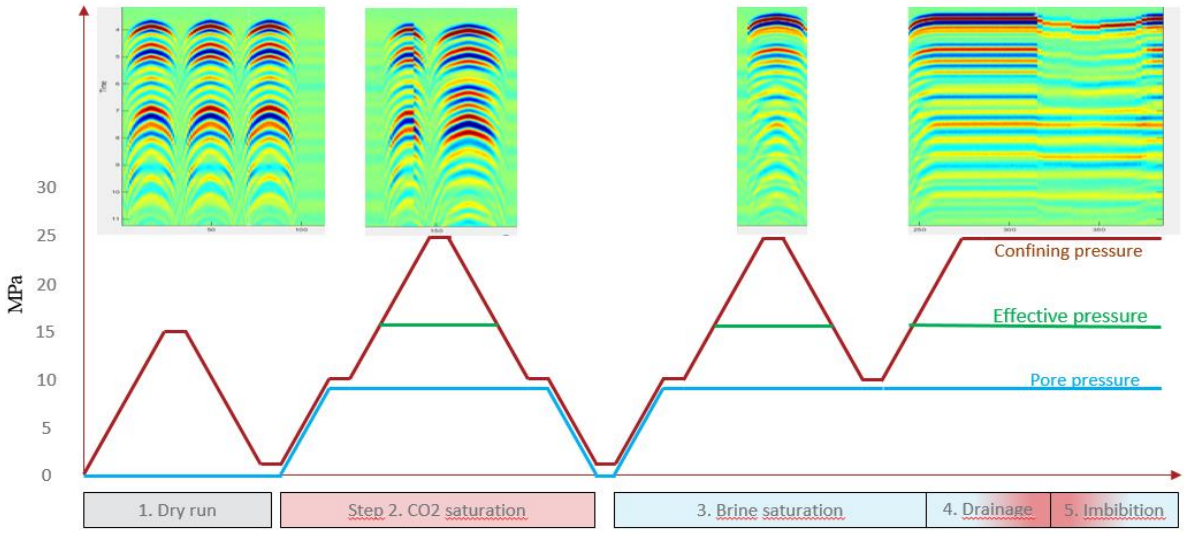

Figure 1.3 VDL screenshot showing seismic waves from dry run to different phases of CO_2 flooding.

1.4 Limitations and future works

Due to time limit, this study focuses mainly on sandstone reservoirs. It could have been of great significance to compare the results with other type of reservoirs like carbonates in order to study the most suitable reservoir type for CO_2 stage. Uncertainties during data acquisition and interpretation like picking the exact first arrival of P- and S-waves may not be ruled out. Measured resistivities for the vertical Red Wildmoor core plug were ambiguously higher than expected and as a result, the values were normalised. Previous laboratory results shows that potential of CO_2 storage varies with porosity, temperature and pressure hence future work should focus on these areas with different CO_2 conditions and describe more precisely the flow rate effect on various samples under different temperature and pressure conditions.

1.5 Chapter descriptions

The first chapter gives a general introduction of this study including an overview of current CCS activities both in small and large scales. It also highlights the motivation, and the objectives of the research. At the end of the chapter, the limitations for the study and suggestions for future research in some particular directions are given.

Chapter 2 focuses on the literature review and theoretical background whereby properties of CO_2 including water solubility and density are highlighted. Different trapping mechanisms including physical and geochemical parameters are elaborated. The chapter end with discussion on petrophysical analysis and rock physics diagnosis including possible applications of Gassmann's equation.

Chapter 3 describes in detail laboratory setup and procedure for the experiments under different pressure conditions. Discussion on sample preparation and determination of mineralogy of the samples is also included in this chapter. This includes mineral

characterization using SEM (Scanning Electron Microscope) and XRD (X-Ray Diffraction) techniques.

Chapter 4 focuses on experimental results, analysis of the acquired data and discussions of the acoustic wave velocities of the three samples. These results are compared with previous laboratory works to identify any similarities. At the end, a comparison is made between the measured and Gassmann-modelled velocities.

Chapter 5 describes laboratory results and discussion of measured electrical resistivity and calculated saturations based on Archie's law discussed in chapter 2. Influence of factors like mineralogy, anisotropy and Vp – CO_2 saturation are also elaborated.

Chapter 6 gives a summary and conclusions of the study by analysing the findings and general trends of the three samples including the effect of change in flow rate, influence of anisotropy and mineralogy on CO_2 flooding, Vp-Vs relation and possible applications of these methods to monitor CO_2 storage.

Chapter 2: Literature review and theoretical background

2.1 Literature review

Much of the experiences for safe CCS have been gained through Enhanced Oil (CO2EOR) in hydrocarbon industry. However, apart from standard CO2EOR operations there are other existing operations that serve as useful trial cases of CCS. This includes commercial scale projects such as Sleipner (Norway), Weyburn (Canada), In Salah (Algeria) and Snøhvit (Norway). At Sleipner, CO_2 is captured from an offshore natural gas processing platform and injected into a saline formation. Several 3D seismic surveys were acquired including in 1994 (base survey), 1999, 2001, 2002, 2004 and 2006 for monitoring the injected CO_2 in Sleipner field shown in Figure 2.1 (Wynn et al., 2003). Seismic images have clearly shown the CO_2 plume migration in the formation and verified its containment. Weyburn is an enhanced oil recovery (EOR) project.

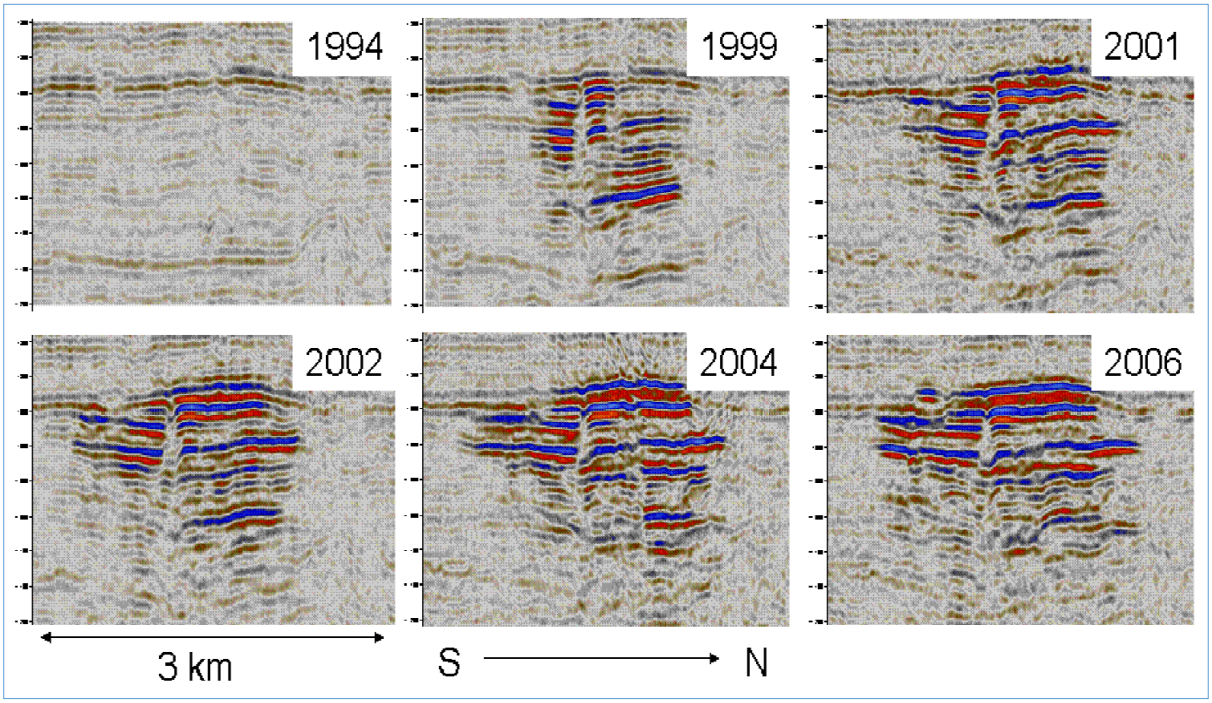

Figure 2.1 Seismic images of the Sleipner plume showing its development from 1994 (pre-injection) through to 2006. Denote the main feeder chimneys in the plume in several 3D time lapse surveys.

The influence of CO_2 saturation on the acoustic properties and electrical resistivity of reservoir rocks has been a subject of intensive study in recent years (e.g. Wang and Nur, 1989; Wang et al. 1998; Xue et al. 2002; Xue and Lei, 2006; Shi et al. 2007b; Moghadam et al. (2014)). This is because injection of CO_2 in different phases into brine-saturated sandstones affects the petrophysical, mechanical and acoustic properties of rock. Wang and Nur (1989) measured ultrasonic velocities in seven sandstones saturated with n-hexadecane before and after flooding with CO_2. They observed that Vp and Vs measured for different sandstones varied with porosity, temperature and effective pressure. They noted Vp

decreased greatly as compared to Vs. Their measured velocities matched with those calculated using Gassmann's equation. They concluded that CO_2 seismic response could be used to monitor its storage.

Later, Wang et al. (1998) used eight dolostones from different location representing different porosity and permeability ranges. At the start, the samples were saturated with a mixture of hydrocarbon oil (Carnation) then water before CO_2 flooding. Using a constant confining pressure of 20 MPa, with a varying pore pressure from 8.3 to 17.9 MPa and temperature of 31^oC, they discovered that P-wave velocities reduction varied between 3-10% while reduction in S-wave velocities varied from 3.3 to 9.5%. They also noted that P-wave velocity is sensitive to both CO_2 and pore pressure change while S-wave velocity is particularly sensitive to pore pressure change. The largest P-wave and S-wave changes were observed with high porosity and high permeability rocks and they suggested that it might be possible to distinguish high porosity and high permeability zones seismically if the sizes of the zones are within seismic resolution based on velocity changes.

Xue et al. (2002) monitored the movement of CO_2 front during flooding experiment using gaseous CO_2 in water-saturated sandstones and measured P-wave velocities under hydrostatic pressure. The P-wave velocities were reduced by order of 10%. Later Xue and Ohsumi (2004) modified the setup to test the effect of different phases of CO_2. They observed that the largest velocity change was with supercritical CO_2. Xue and Lei (2006) used differential arrival time to display the velocity changes during the injection test by P-wave velocity tomograms. The results showed variation in P-wave velocities across the sample as the CO_2 swept through the core. They also recorded the highest velocity decrease during supercritical CO_2 injection and lowest during gaseous CO_2 injection and concluded that observed difference in P-wave velocity images was due to heterogeneity of pore spaces distribution in the rock and injected CO_2 phases.

Shi et al. (2007b) studied dynamic behaviour of P-wave velocity during supercritical CO_2 injection and concluded that the velocity reduction depends on final state of saturation as either homogenous, or patchy. Based on observed velocity reduction and Gassmann modelling for uniform and patchy saturation models, they suggested that regions closest to injection points reached uniform saturation while large patchy saturations occurred farthest from the injection points. Mikhaltsevitch et al. (2014) measured the elastic and inelastic properties of Donybrook Sandstone flooded with supercritical CO_2. They varied the confining pressure from 10 MPa to 60 MPa with a pore pressure not more than 0.1 MPa for dry and 10 MPa for fluid saturated states. They observed a 5% reduction in P-wave velocities between water-saturated and dry samples and concluded that Gassmann's fluid substitution theory is applicable for the interpretation of measured data.

Moghadam et al. (2014) carried out a laboratory study to investigate the response of CO_2 saturated Red Wildmoor sandstone under varying temperature (22^oC, 30^oC, 40^oC) and pressure (1-17 MPa). The study concluded that regardless of temperature, introducing CO_2 into the sample reduced the wave velocity of the rock up to the critical pressure. Their laboratory observations are in agreement with calculated velocities using Gassmann's equation.

The utility of the marine controlled-source electromagnetic CSEM method for identifying hydrocarbon reservoirs was first demonstrated in a test by Statoil over the Girassol prospect, Angola (Ellingsrud et al., 2002). Constable and Weiss (2006) carried out feasibility study of

CSEM for reservoir monitoring by showing that CSEM response are sensitive to the lateral extent and thickness of resistive bodies. Later Arnold et al. (2009) extended Lien and Mannseth (2008) work by examining the applicability of marine controlled source electromagnetic (CSEM) method to the reservoir monitoring by analysing 2D models. Their study shows that measurable changes in CSEM responses are observed when 10% of the resistive reservoir is replaced by conductive pore fluid.

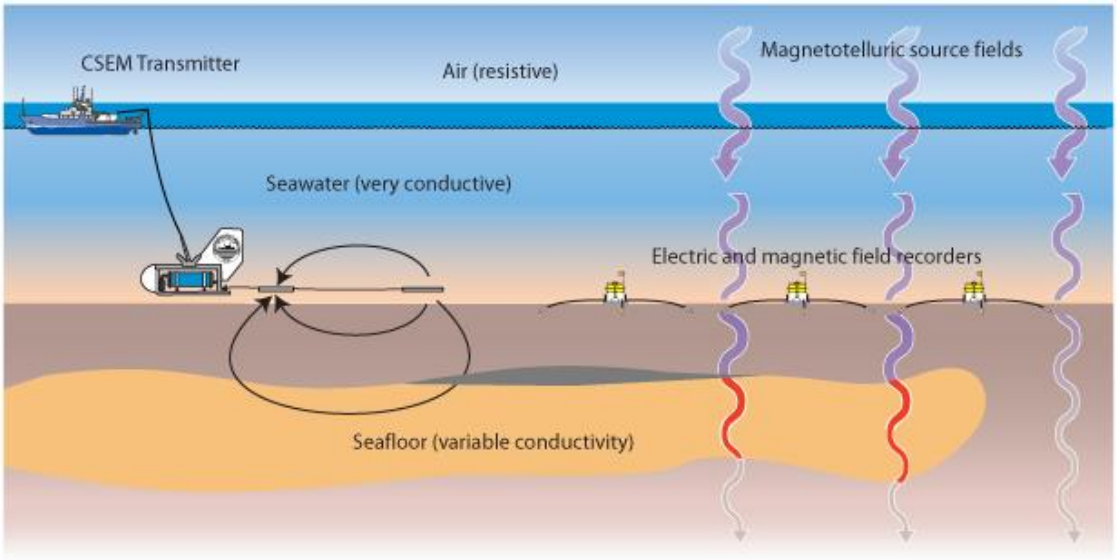

Figure 2.2 Concept diagram for marine controlled source EM (CSEM) and marine magnetotellutic (MT) method (Smith et al 2012).

2.2 Theoretical background

2.2.1 Properties of CO_2 and brine

CO_2 is a colourless, odourless, non-combustible, and relatively non-reactive gas under ambient temperature and pressure conditions. From the CO_2 phase diagram shown in Figure 2.3, solid CO_2 is stable under low temperatures and elevated pressures. Liquid CO_2 forms at pressure above 0.5 MPa and increasing the temperature at low pressure will change solid CO_2 directly into gaseous CO_2 through sublimation. The triple point of carbon dioxide, where the solid, liquid and gaseous phase coexists is at a pressure of 0.51 MPa and temperature of -56.6^{o}C while the critical point is at temperature of 31.1^{o}C and pressure of 7.39 MPa. The mixing of CO_2 with water results in two immiscible phases, a H_2O-rich liquid phase and a CO_2-rich compressed gas phase supercritical fluid, that contains only small amount of water usually <2 mol% (Spycher and Pruess, 2005). Volume change of fluids in response to applied pressure is expressed as their compressibility and compared to water; supercritical CO_2 has a very high compressibility (Hao et al., 2004) thus any relatively insignificance change in temperature and pressure can significantly change the density.

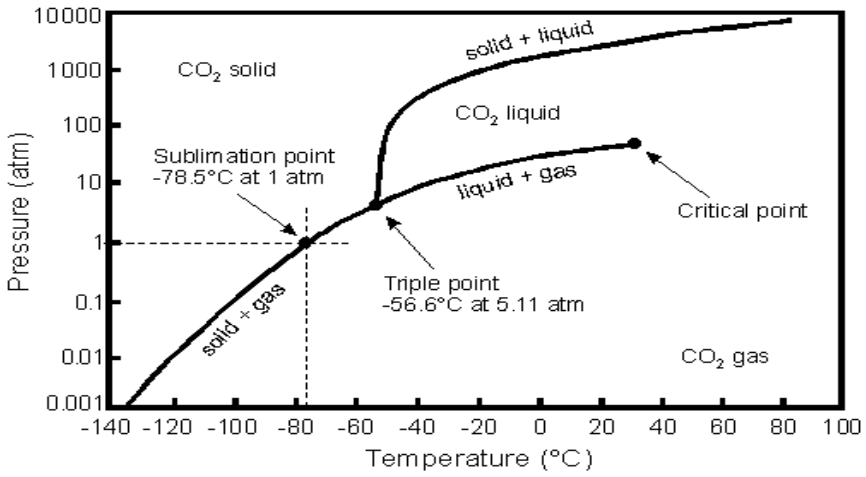

Figure 2.3 CO_2 phase diagram (IPCC, 2005).

CO_2 has a lower viscosity compared to formation water (about 15-20 times less viscous than brine at a depth of 1000 m). This causes an upward movement via viscous fingering (Garcia and Pruess, 2003) a term used to refer to the finger-shaped flow patterns resulting from the injection of low viscosity fluid into a more viscous one causing the CO_2 injected to spread and accumulate above the formation water phase (Suekane et al., 2005). The relationship between the dissolved and free-phase CO_2 determines how far the CO_2 will migrate before it is eventually trapped in solution. Some of the factors that influence how far the dissolved CO_2 will migrate include stratigraphic heterogeneities (e.g. siltstones, shales and clay in the reservoir), geochemical reactions and temperature.

Temperature, pressure and salinity are some of the factors that affect CO_2 solubility. During storage, CO_2 is injected into sandstone reservoirs at a depth greater than 800 m in supercritical condition (sCO_2) where it exists in supercritical state (Holloway, 2005; Holt et al., 1995b; Izgec et al., 2008). Under normal atmospheric temperature and pressure conditions, CO_2 is in the gas phase. Under super critical conditions, CO_2 can act both as gas and as a liquid and can therefore occupy the same pore space than a less denser gas would and this explains why it is often injected at formation depths where it keeps these properties (IPCC, 2005).

2.2.2 Water solubility

CO_2 is soluble in water and brine, which are commonly present in soil and sedimentary rocks. Figure 2.4 shows variation of CO_2 with temperature at different pressure conditions. CO_2 solubility tends to increase as pressure increases but decreases sharply as temperature and salinity increase (Jarrell and Engineers, 2002; Prutton and Savage, 1945; Wiebe and Gaddy, 1939). Salinity is affected by numerous variables including temperature, pressure, pH, and soil or rock lithology and it tends to increase with increasing depth thus if water has more salt in it, it will tend to be heavy and tend to sink.

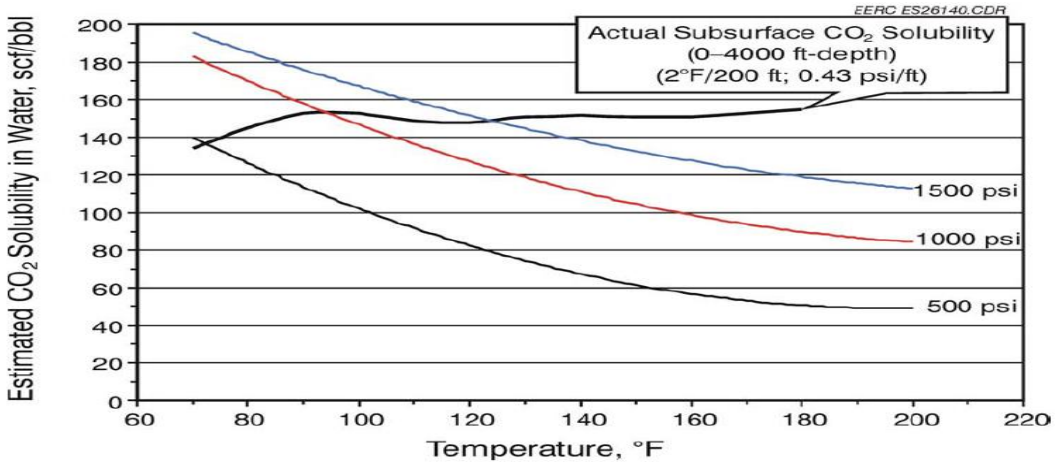

Figure 2.4 Variation of CO_2 solubility in water as a function of temperature and pressure

2.2.3 Density and viscosity

CO_2 is a dense and supercritical liquid above its critical point temperature of 33 ^oC and pressure of 7.4 MPa (Fig. 2.5). In its supercritical state, CO_2 has a density and viscosity less than that of water. After CO_2 injection ends, buoyancy will drive its mobility. Its buoyancy will cause the CO_2 to migrate to the top of the injection zone. The net result will be a two-phase system of lower-density CO_2-rich fluid, which will flow upwards, and a higher density aqueous phase containing dissolved CO_2 which will flow downwards (Oldenburg et al., 2001; White et al., 2003). The mobility of dissolved CO_2 is controlled by the rate of the bulk water flow through the geologic sink. As CO_2-saturated water migrates upward towards the surface, the temperature and pressure will decrease, and the CO_2 will be separated from the solution, resulting in the formation of bubbles of CO_2 gas that will rise quickly under buoyancy forces (Oldenburg et al., 2002; Tsang et al., 2001; White et al., 2003).

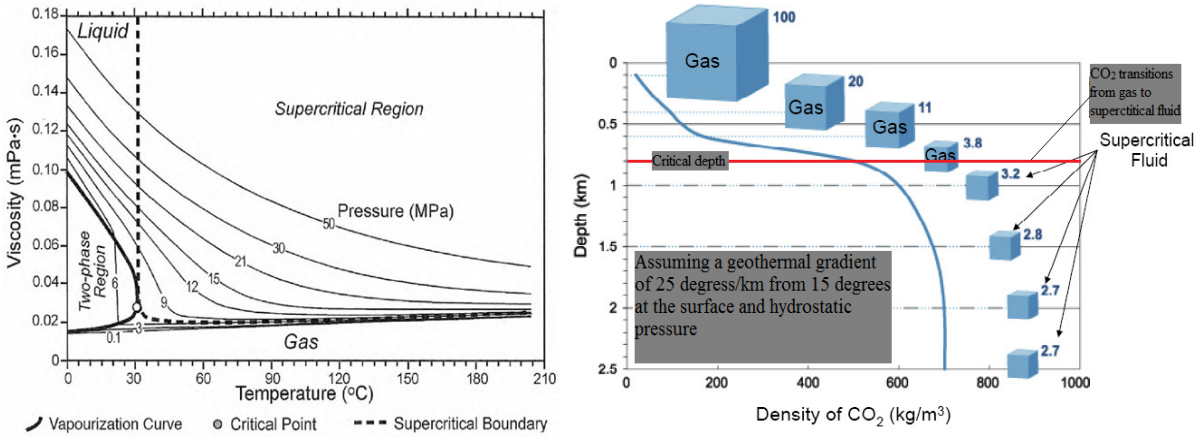

Figure 2.5 Variation of CO_2 viscosity as a function of temperature and pressure (Bachu and Adams, 2003) (left). Variation of CO_2 density with depth (right), assuming hydrostatic pressure and a geothermal gradient of 25^oC/km and surface temperature 15^oC (based on the density data of Angus et al. (2013). Cubes represent the relative volume occupied by the CO_2

and down to 800 m; this volume can be seen to dramatically decrease with depth. At depth below 1.5 km, the density and specific volume become nearly constant.

2.2.4 Diffusivity

Transport of CO_2 especially in the shallow subsurface may be controlled by molecular diffusivity. The molecular diffusivity of the CO_2 in air is comparable to other gases and is approximately 1.65×10^{-5} m^2 s^{-1} at 25 ^oC and 1 atm (0.1 MPa) (Vargaftik et al., 1996). Increasing pressure tends to decrease diffusivity, while increasing temperature increases it (Oldenburg et al., 2002). The molecular diffusivity decreases as CO_2 becomes denser and more liquid-like as pressure increases.

2.3 Factors influencing CO_2 storage

There are several factors that influence the storage potential of CO_2 in a geological formation among them:

2.3.1 Anisotropy

Lithological factors such as shape, size, orientation and packing of grains may originate anisotropy of a formation (Gelius and Johansen, 2010). There are two major types of anisotropy, (i) Vertical Transverse Isotropy (VTI) and (ii) Horizontal Transverse Isotropy (HTI). Vertical Transverse Isotropy (VTI) occurs when there is horizontal alignment with vertical axis of symmetry (Fig. 2.6) whereas Horizontal Transverse Isotropy (HTI) occurs when there is vertical alignment with horizontal axis of symmetry. Certain material properties like sound velocity, permeability, electrical resistivity are directionally controlled by anisotropy (Winterstein, 1990). In VTI media, seismic waves travel faster in the horizontal direction than vertical direction whereas in HTI media, seismic waves travels faster vertically than horizontally and elastic properties are uniform in a vertical plane parallel to fractures but may vary in the direction perpendicular to the fractures (Armstrong et al., 1994).

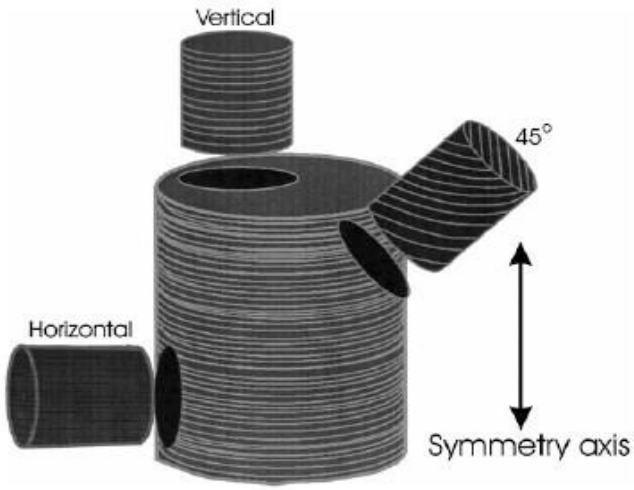

Figure 2.6 Traditional three-plug method for measuring transverse isotropy in laboratory core plug (Wang, 2002). In our study, we u vertically and horizontally drilled core plugs.

2.3.2 Salinity

The phase behaviour of the CO_2/brine mixture can influence CO_2 storage and this depends upon brine salinity. According to Duan and Sun (2003), solubility of CO_2 in formation water decreases with increasing salinity considerably. High-salinity brines improve the impact of gravitational forces; while reducing the solubility trapping and lower the injectivity.

2.3.3 Wettability

Wetting can be defined as the preference a solid surface will have for one fluid over another and it is determined by the force balance between adhesive and cohesive forces, which can be estimated by determining the contact angle, and spreading coefficient (Fig. 2.7). The contact angle (θ) is the angle at which the liquid-vapour interface meets the solid-liquid interface and is determined by the result between adhesive and cohesive forces. A contact angle less that 90^o usually indicate that wetting of the surface is very favourable, and the fluid will spread over a large area of surface while angles greater than 90^o generally means that wetting of the surface is unfavourable. For water, a wettable surface may be termed as hydrophilic and a non-wettable surface as hydrophobic.

Depending on the wetting properties of the fluids, there are essentially two different types of displacement in two-phase flow in porous media. In this thesis, we are considering drainage displacements where a non-wetting invading fluid (liquid CO_2) displaces a wetting fluid (brine). The opposite case, imbibition, occurs when a wetting fluid displaces a non-wetting fluid. Usually wetting phase tends to spread out on the solid, and a non-wetting phase does not. According to Suman and Knight (1997), wettability is found to have the dominant effect on resistivity.

Figure 2.7 Example of water wetting and non-wetting phases. For the water wetting phase a drop of water spreading on a solid, with a contact angle less than 90 degrees (left) while for the non-wetting phase a drop of water resting on a solid (right), with a contact angle greater than 90 degrees(Suman and Knight, 1997).

2.3.4 Capillary pressure

Capillary pressure (*Pc*) is the pressure difference across the interface between two immiscible fluids arising from the capillary forces (surface and interfacial tension). In porous media, the capillary pressure is the difference between the pressure in the wetting and non-wetting phase. It is defined by Equation 2.1,

$$P_c = P_{nonwetting} - P_{wetting} \qquad \text{Eq. 2.1}$$

Thus for this study, above equation can be written as;

$$P_c = P_{CO_2} - P_{brine} \qquad \text{Eq. 2.2}$$

High capillary forces require a high injection pressure for a given injection rate and reduces gravity segregation, thus giving a more homogenous CO_2 plume, which improves the dissolution of CO_2. For given petrophysical characteristics, simulations indicate that high capillary forces create a CO_2 plume that is larger in the lateral extent (Ide et al., 2007). This allows CO_2 to have more contact with brine, causing more solubility trapping in the short term. High gravitational forces, however, make CO_2 migrate upwards and accumulate beneath the cap rock, leading to more contact with brine in the long term through convective mixing (Ott et al., 2012).

2.3.5 Temperature

Solubility of CO_2 in brine and the viscosity of brine increases with an increase in temperature. At higher temperatures, a greater percentage of injected CO_2 goes to aqueous phase. Alkan et al. (2010) ran a series of simulations with various pressure-temperature conditions and modified salinity and capillary pressure curves. They found out that, with the injection pressures similar for both cold and warm basins at a given injection rate, CO_2 dissolves about 10% more in the warm basin than in the cold basin. The simulations show

higher storage capacity for warm basins due to decreased CO_2 density with temperature. Higher dissolution lowers the injection pressure compensating the disadvantage of low CO_2 density and compressibility for storage in warm basins

2.3.6 Permeability

Considering a porous rock filled with a pore fluid like brine or CO_2, wherever there exists a spatial gradient in the hydraulic potential of the pore fluid, the fluid will flow though the rock in response to this gradient. Darcy's law gives the relationship between the potential gradient and the flow rate, and permeability is the constitutive coefficient that relates the flow rate to potential gradient in Darcy's law. Darcy's law is only valid for low flow rates, thus for higher flow rates, defined as those which the Reynolds number is greater than unity, the pressure gradient is generally found to be quadratic rather than linear function of the flow rate. The influence of the pore fluid on the flow rate is contained solely in the viscosity term. Hence, permeability coefficient is a property of the rock, not in the fluid and depends on the pore geometry of the rock. The permeability of the reservoir rock can alter the capillary pressure curve. If the value of the permeability is lower, the pore size is smaller, and the capillary pressure is higher.

2.4 Trapping mechanisms

There are several trapping mechanisms for CO_2 when it accumulates under the cap rock (Fig 2.8). A combination of chemical and physical trapping mechanisms ensures that the CO_2 injected does not leak from the reservoir to the surface for at least thousands of years (IPCC, 2005) and this is made possible by a thick and very low permeable cap rock.

2.4.1 Physical trapping

Physical trapping is where CO_2 is trapped as a buoyant supercritical CO_2 'bubble' and still keeps the physical properties it had during the injection (IPCC, 2005). The two main types are structural where the CO_2 is trapped under low permeable layer such as anticline or a tilted fault block, and the residual trapping, which is often present in saline formation where fluid flow is slow and as a result, the residually trapped CO_2 dissolves into the formation water. According to Bachu et al. (2007) structural trapping poses the highest risk in the event of existence of faults close to storage site.

2.4.2 Geochemical trapping

Geochemical trapping includes solubility and mineral trapping. Solubility trapping occurs when CO_2 dissolves in brine. As more CO_2 dissolves in brine, the brine becomes denser and sinks towards the bottom of the reservoir and with time the amount of dissolved CO_2 in formation water increases. Mineral trapping occurs when the dissolved CO_2 reacts with the reservoir rocks; it forms a mild (carbonic) acid, which as a result lowers pH (~3.0 up to neutral) of the formation brine. The acid then undergoes chemical reaction with silicate-rich minerals like Ca, Mg and Fe to form carbonate minerals (Bachu et al., 1994; Czernichowski-Lauriol et al., 2006; Gunter et al., 1996).

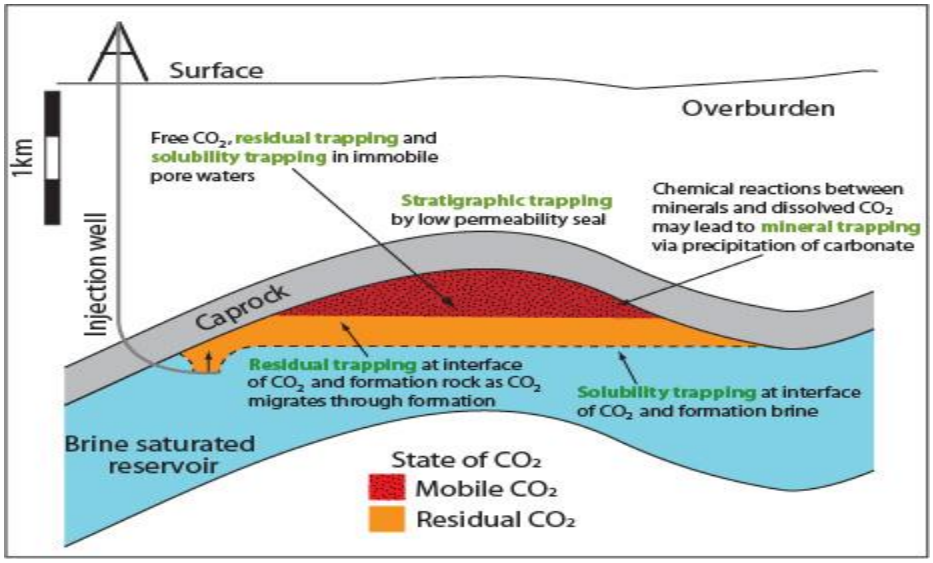

Figure 2.8 CO_2 trapping mechanisms (Burnside and Naylor, 2014).

2.5 Petrophysical analysis of reservoir rocks

The petrophysical analysis helps to evaluate reservoir parameters such as porosity (φ), lithology, saturation, and permeability and their effect on seismic and electric properties like Vp, Vs, density, resistivity and elastic moduli.

2.5.1 Porosity estimation

Porosity is the fraction of pore space volume to the total rock volume and it is usually determined using density, sonic and neutron logs. In this study, porosity was calculated using Scanning Electron Microscope (SEM) although this method is not the most accurate in terms of identifying mineral composition. XRD was used to analyse the mineral composition in more details.

2.5.2 Saturation calculation

Electrical resistivity measurements are commonly used to estimate in-situ water saturation in hydrocarbon reservoirs. The interpretation of these measurements is usually based on Archie's equation (Archie, 1942). The method gives reasonably accurate estimates of water saturation in sandstone and carbonate reservoirs with low clay-mineral content. Presence of shale in sandstone influences the electrical conductivity of the formation water due to the presence of clay minerals like kaolinite and illite, which also contribute to the electrical conduction. Because of this, more complicated electrical models and equations should be used to estimate water saturation for shaly sandstone reservoir.

Archie (1942) established that the ratio of the conductivity of the pore fluid to the bulk conductivity of the fully saturated clean sandstones corresponds to the formation factor *F*. This equation relates the resistivity index *I* of a partially saturated rock to the level of water saturation *Sw*

$$I = S_w^{-n} \qquad \text{Eq. 2.3}$$

Where *I* is the resistivity index ($I = R_t/R_o$), *Rt* and *Ro* are the resistivities of the partially and fully water-saturated rock, respectively at the same temperature and pressure, and *n* is the saturation exponent. It is also related to porosity and can be expressed by

$$\mathrm{F} = \frac{\mathrm{a}}{\phi^{\mathrm{m}}} \qquad \text{Eq. 2.4}$$

a is the coefficient and it's value close to 1 introduced by Wyllie and Gregory (1953). *F* is the formation resistivity factor and *m* is the cementation exponent. The *a* coefficient may be considered a reservoir constant according to Worthington (1993), although originally Wyllie and Gregory (1953) considered it a function of porosity and formation factor of the original unconsolidated aggregate before cementation. Resistivity of partially saturated rock (R_t) with formation water and resistivity of the fully saturated rock (*Ro*) with water can be expressed by

$$R_o = \varphi^{-m} \cdot R_w \qquad \text{Eq. 2.5}$$

$$R_t = a \cdot R_w \cdot \varphi^{-m} \cdot S_w^{-n} \qquad \text{Eq. 2.6}$$

By combining the two equations, the water saturation can be determined as;

$$S_w = \sqrt[n]{\frac{a \cdot R_w}{R_t \cdot \varphi^m}} \qquad \text{Eq. 2.7}$$

n is saturation component, *m* is cementation factor and varies around 2, *a* is the tortuosity factor, assumed as 1, *F* is formation resistivity factor and R_t is the resistivity of the rock (measured resistivity). R_o is electrical resistivity of the saturated formation, R_w is resistivity of brine, S_w is water saturation and ϕ is the porosity.

In order to use Equation 2.7, several parameters should be known before computing saturation. The heterogeneity of the reservoir must be taken into account. Nakatsuka et al. (2009) suggested the use of Resistivity Index (*RI*), which relates to Archie's second law. Because resistivity increases due to injection of CO_2, saturation computed by the relation of partially and fully saturated can be considered as Equation 2.8.

$$\mathrm{RI} = \frac{\mathrm{R}}{\mathrm{R_0}} = (\mathrm{S_w})^{-\mathrm{n}} \qquad \text{Eq. 2.8}$$

Equation 2.9 shows the formula to compute the CO_2 saturation from RI in Equation 2.8. According to Bassiouni (1994), the resistivity of a rock is influenced by (i) shale volume, (ii) porosity, (iii) water saturation, (iv) formation water resistivity and (v) metallic minerals.

$$S_{CO_2} = 1 - Sw = 1 - \left(\frac{R_o}{R}\right)^{\frac{1}{n}} \quad \text{Eq. 2.9}$$

In saturation calculation, a combination of Equation 2.8 and Equation 2.9 were utilized where *Ro* is the resistivity of brine saturated sandstone.

2.5.3 Vp –Vs relationships

Shear velocity is an important parameter for rocks physics analysis. Vs can be estimated using several empirical relations including Castagna et al. (1985), Han (1986), Castagna and Backus (1993), Fawad et al. (2011) and Krief et al. (1990). Castagna et al. (1985) derived an empirical linear relationship also known as mudrock line equation between Vp and Vs velocity for both sandstone and shale formations,

$$Vs = 0.8621Vp - 1.1724 \text{ [km/s]} \quad \text{Eq. 2.10}$$

Later, Han et al. (1986) while working on the effect of clay and porosity content came up with a new relation for Vp and Vs, where:

$$Vs = 0.7934Vp - 0.7868 \text{ (km/s)} \quad \text{Eq. 2.11}$$

Krief et al. (1990) suggested a relationship between the squares of Vp and Vs, where:

$$Vp^2 = aVs^2 + b \text{ (km/s)} \quad \text{Eq. 2.12}$$

Table 2.1 A summary of the regression coefficients a and b from Krief's formula.

Lithology	a	b
Sandstone (wet)	2.213	3.857
Sandstone (Gas)	2.282	0.902
Limestone	2.872	2.755
Sandstone (Shaly)	2.033	4.894

Castagna and Backus (1993) introduced a new relation of least square linear fit expression for clastic rock where:

$$Vs = 0.8042Vp - 0.8559 \text{ (km/s)} \quad \text{Eq. 2.13}$$

Mavko et al. (2009) suggested several equations for relating Vp and Vs depending on the lithology.

i. Unconsolidated sand: $Vs = 0.79Vp - 0.79$ (km/s)
ii. Sandstone with Vsh < 0.25: $Vs = 0.754Vp - 0.657$ (km/s)
iii. Sandstone with Vsh > 0.25: Vs = 0.842Vp-1.099
iv. Sandstone with porosity < 0.15: Vs = 0.835Vp – 1.137

v. Sandstone with porosity > 0.15: Vs = 0.756Vp - 0.662

Fawad et al. (2011) derived the following relation between Vp and Vs velocities for synthetic brine saturated sandstone samples.

$$\mathrm{Vs} = 0.8249\mathrm{Vp} - 0.9984\ (\mathrm{km/s}) \qquad \text{Eq. 2.14}$$

The bulk modulus (K) and shear modulus (μ) are calculated using

$$\mathrm{K} = \rho\left(\mathrm{Vp}^2 - \frac{4}{3}\mathrm{Vs}^2\right) \qquad \text{Eq. 2.15}$$

$$\mu = \rho\mathrm{Vs}^2 \qquad \text{Eq. 2.16}$$

Most of these velocity estimations were not used in this thesis given that they are not derived from CO_2 flooding; most of them are applicable for fully saturated conditions as opposed to patchy saturation experienced during CO_2 flooding. From the results, Vs increases with decreasing Vp for drainage and vice versa for imbibition.

2.5.4 Gassmann fluid substitution

Gassmann (1951b) equation relates the bulk modulus of a rock to its pore frame and fluid properties. The bulk modulus of a saturated rock is given by the low frequency Gassmann theory in Equation 2.17. This equation predicts a large decrease of Vp and small increase of Vs if only small amount of gas is contained in the pore space of compressible sandstone.

Fluid substitution is an important part of any seismic attribute study, as they provide a valuable tool for modelling various fluid scenarios. The following assumptions are to be made when applying Gassmann's equation:

i. Porous material is isotropic, elastic, well-connected pore spaces, and composed of one type of mineral. This assumption is violated if the rock is composed of multiple minerals with a large contrast in their elasticity.
ii. Medium is closed system with no pore fluid movement across boundaries.
iii. No chemical interaction between the fluid and rock frame meaning the shear modulus remain constant.
iv. There are no chemical interactions between the fluids and the rock frame meaning the shear modulus remains constant.
v. The pore space is fully saturated at all times and the porosity remains constant thus no cementation or dissolution with changing the geochemical conditions in the pores.
vi. Quasi-static conditions where the frequencies are sufficiently low (10-100Hz) such that the induced pressure can be equilibrated through the pore space. For higher frequencies Biot (1956) can be used.

As a step to estimate CO_2 saturation, the two important parameters μdry and $Kdry$ were evaluate. μdry is a fundamental property of solid materials. For porous sandstone, there are several effective parameters that affects it among them change in effective confining pressure (Dvorkin and Nur, 1996b). In this study, we measure Vp and Vs under dry, CO_2 saturated and brine-saturated conditions at a varying differential pressure of 1-15MPa and calculate K_{dry},

μdry and *μsat* using Equation 2.17 and Equation 2.18. *μsat* was estimated using *μdry*. According Gassmann (1951a), bulk modulus of a saturated rock, K_{sat}, is related to the rock's frame bulk modulus, K_{dry}, the minerals grain's bulk modulus, K_{min}, the pore fluid's bulk modulus, K_{fl}, and the porosity, ϕ , of the rock through:

$$\mathrm{K_{sat}} = \mathrm{K_{dry}} + \frac{\left(1 - \frac{\mathrm{K_{dry}}}{\mathrm{K_{min}}}\right)^2}{\frac{\varphi}{\mathrm{K_{fl}}} + \frac{(1-\varphi)}{\mathrm{K_{min}}} - \frac{\mathrm{K_{dry}}}{\mathrm{K_{min}^2}}} \qquad \text{Eq. 2.17}$$

The shear modulus is regarded to be independent of pore fluid since its incapable of sustaining shear forces thus shear modulus of saturated rock is the same as that of dry rock or of the saturated rock with another fluid (Eq. 2.18).

$$\mu_{\mathrm{dry}} = \mu_{\mathrm{sat}} \qquad \text{Eq. 2.18}$$

μ_{sat} is the shear modulus of the saturated rock, μ_{dry} is the shear modulus of the dry rock. The pore space of a rock is typically occupied by two or more fluid phases, and one has to calculate the bulk modulus and density of each individual fluid present. Assuming a uniform distribution of a homogenous fluid throughout the pore space, the bulk modulus of fluid can be calculate using Reus model for mixed fluid in Equation 2.19.

$$K_{fl} = \left[\frac{\mathrm{S_w}}{\mathrm{K_w}} + \frac{1 - \mathrm{S_w}}{Kco_2}\right]^{-1} \qquad \text{Eq. 2.19}$$

Kw and Kco_2 are bulk modulus for water and CO_2 respectively. In this thesis, we assume that all the above assumptions are met in order to apply Gassmann's equation. The bulk modulus of the saturated rock, *Ksat*, can be related to its compressional velocity, shear velocity, and bulk density through Equation 2.20.

$$\mathrm{K_{sat}} = \rho_{\mathrm{eff}}(\mathrm{V_{p}^2}_{sat} - \frac{4}{3}\mathrm{V_{s_{sat}}^2}) \qquad \text{Eq. 2.20}$$

ρeff is the effective bulk density of the rock, Vp_{sat} and Vs_{sat} are the compressional and shear velocity for saturated sample.

To determine the mineral grain's bulk modulus, the minerals making up the rock need to be identified. For samples, whose composition is of one or largely dominated by one mineralogy, determining *Kmin* is straightforward. For samples consisting of more than one mineral, the volume fraction of the various mineral constituents of the matrix need to be identified. The mineral type and weight percentage were determined using XRD analysis. With the mineral composition known, the bulk modulus of the sample's matrix that is composed of mixed mineral composition can be estimated using Hill's average.

$$K_{\mathrm{min}} = \frac{1}{2}(K_v + K_R) \qquad \text{Eq. 2.21}$$

Where K_V is the Voigt's average and K_R is Reuss' average. The two averages give the maximum and minimum values possible for a mixture.

$$K_v = \sum_{i=1}^{n} f_i K_i \qquad \text{Eq. 2.22}$$

$$\frac{1}{K_R} = \sum_{i=1}^{n} \frac{f_i}{K_i} \qquad \text{Eq. 2.23}$$

f_i is the fraction amount of the ith mineral, and K_i is the bulk modulus of the corresponding mineral. The bulk modulus of the fluid, K_f, can be calculated using equation.

$$K_f = \rho_f V_f^2 \qquad \text{Eq. 2.24}$$

In the case of fluid mixtures, the overall bulk modulus of pore fluid can be calculated from averaging the contribution of the individual fluids using Voigt's or Reuss' average equation. The overall fluid bulk density from the mixture is given by;

$$\rho_f = \sum_{i=1}^{n} f_i \rho_i \qquad \text{Eq. 2.25}$$

In terms of using an empirical relation, Dvorkin and Nur (1996a) suggested that between low porosity and critical porosity, there is a linear trend for the dry moduli as a function of porosity. The critical porosity separates whether the rock is in grain-load bearing ($\phi<\phi_c$) or a fluid –load bearing ($\phi>\phi_c$) domain. For most reservoir rocks, the grains are load bearing and critical porosity serves as a limiting case. The bulk and dry moduli for dry rocks are given by:

$$\mathrm{K_{dry}} = \mathrm{K_{min}}\left(1 - \frac{\phi}{\phi_c}\right) \text{ where } \phi \leq \phi c \qquad \text{Eq. 2.26}$$

$$\mu_{\mathrm{dry}} = \mu_{\mathrm{min}}\left(1 - \frac{\phi}{\phi_c}\right) \text{ where } \phi \leq \phi c \qquad \text{Eq. 2.27}$$

(Krief et al., 1990) also suggested a formula for calculating K_{dry}

$$\mathrm{K_{dry}} = \mathrm{K_{min}}(1-\phi)^{(1-\phi+A)/(1-\phi)} \qquad \text{Eq. 2.28}$$

Where A is an empirical constant set at 3. From Gassmann's Equation 2.17, K_{dry} can be derived from fluid saturated K_{sat} (Zhu and McMechan, 1990):

$$K_{dry} = \frac{K_{sat}\left(\frac{\phi K_{min}}{K_{fl}} + 1 - \phi\right) - K_{min}}{\frac{\phi K_{min}}{Kfl} + \frac{K_{sat}}{K_{min}} - 1 - \phi} \qquad \text{Eq. 2.29}$$

Han and Batzle (2004) carried out study on different sandstone samples to calculated *Kdry* and came up with two suggestions;

$$K_{dry} = (1 - A \times \phi + B \times \phi^2 - C \times \phi^3) \times K_{min} \qquad \text{Eq. 2.30}$$

A = 3.206, B = 3.349, C = 1.143. Equation 2.30 can be simplified if porosity is not too high (ϕ <30%):

$$K_{dry} = (1 - D \times \phi)^2 \times K_{min} \qquad \text{Eq. 2.31}$$

D for clean sandstone equals 1.52 and it represents in the first order, the correlation of porosity to bulk modulus for relatively clean sandstone and clastic sediments.

Table 2.2 Compiled empirical relations and relative D-porosity models for different rocks (Castagna et al., 1985; Mavko et al., 2009)

		Kd = (1-Axϕ +Bxϕ ^{3})xK$_o$			K$_d$ = (1-Dxϕ)^{2}xK*o*
Rock type	*V*-emp.relation P$_e$ = 40 MPa	A	B	C	D
Dry shale sandstone	Vp = 5.41-6.35xϕ Vs = 3.57-4.57xϕ	3.053	3.070	1.016	1.450 (Ko = 32.5 GPa)
Dry clean sandstone	Vp = 5.97-7.85xϕ Vs = 4.03-5.85xϕ	3.206	3.349	1.143	1.523 (Ko = 37.0 GPa)
Silicate clastic	Vp = 5.81-9.42xϕ Vs = 3.89-7.07xϕ	3.283	3.284	1.014	1.583 (Ko = 36.0 GPa)
Dry vuggy sandstone	Vp = 6.47-5.84xϕ Vs = 3.39-3.03xϕ	2.815	2.639	0.824	1.340 (Ko = 71.9 GPa)
Dry limestone	Vp = 6.19-9.80xϕ Vs = 3.20-4.90xϕ	4.244	5.820	2.605	1970 (Ko = 66.8 GPa)
Dry dolomite	Vp = 6.78-9.80xϕ Vs = 3.72-5.20xϕ	3.578	4.020	1.358	1.705 (Ko = 94.4 GPa)

Table 2.3 Table of constants used in the study adapted from Mavko et al. (2009)

		Unit	Pore pressure	Temperature
Density of water	1.02	[g/cm^3]		
Bulk modulus water	2.25	[Gpa]		
Density of gas	0.25	[g/cm^3]		
Bulk modulus gas	0.25	[GPa]		
Density of quartz and dry clay	2.65	[g/cm^3]		

Bulk modulus of quartz	37	[Gpa]		
Bulk modulus clay	20.7	[GPa]		
Velocity of liquid CO_2	411	[m/s]	10MPa	27 ^oC
Density of liquid CO_2	0.805	[g/cm^3]	10MPa	27 ^oC
Bulk modulus liquid CO_2	0.13598	[Gpa]	10MPa	27 ^oC
Bulk modulus sand	40	[GPa]		

Chapter 3: Materials and methods

This chapter focusses on the materials used in the laboratory and the methods used for the petrophysical analysis and mineral characterisation including XRD and SEM. Experimental setup and protocols are also elaborated in the chapter including data acquisition techniques.

3.1 Sample characterization

The sandstone core plugs used in this study are from two different localities: the horizontally and vertically drilled Red Wildmoor Sandstone plugs from England and the low permeable (15-20 mD) vertically drilled Berea Sandstone plug from USA. These samples were selected since they represent typical sandstone reservoirs in terms of porosity and permeability. Prior to experiments, X-Ray Diffraction (XRD) and Scanning Electron Microscope (SEM) analyses of the samples were performed to identify minerals; petrophysical parameters like, density (grain and bulk) and porosity were then calculated. Petrophysical properties of studied sandstone core plugs are show in Table 3.1.

Table 3.1 Petrophysical properties of Red Wildmoor and Berea sandstones core plugs.

Sample	Drilling direction	Porosity	Permeability [mD]	Dry density [g/cm^3]	Pore volume [mm^3]
Red Wildmoor	Vertical	22	-	1.90	19.27
Red Wildmoor	Horizontal	22	-	1.92	19.83
Berea	Vertical	20	20-40	2.28	16.87

3.1.1 SEM and XRD analyses

Scanning Electron Microscope helps to examine grain structures and micro-features quantitatively. It can produce highly magnified and resolved microscopic images of the surface of a rock through scanning the rock with a beam of electrons. JEOL JSM 6460LV scanning electron microscope with LINK INCA Energy (300 EDS) from Oxford Instruments at the department of Geology was used in this study. During SEM imaging, a beam of electron is emitted from an electron gun fitted with a filament and is accelerated by attractive forces towards an anode. Upon interaction with the surface of the sample, secondary electrons are created from ionization and scatters. These secondary electrons are recognized by a detector, and an image is produced from a number of electrons scattered from each spot on the sample's surface. Prior to imaging, the samples are prepared by coating the surface with gold powder which provides conductivity to the surface of the samples to prevent electrons from being trapped, thereby creating an overly bright image. The JEOL JSM 6460LV SEM setup has low vacuum capability, which negated the need to coat sample surfaces with an electron conductive material in order to obtain high quality images of sample surfaces. The brightness and contrast of SEM backscatter electron images gives an indication of compositional differences within the sample, with brighter regions corresponding to heavier elements and vice versa for lighter elements.

X-ray powder diffraction (XRD) is a rapid analytical technique primarily used for phase identification of crystalline materials and can provide information on unit cell dimensions. The analysed material is finely ground, homogenized, and average bulk composition is determined. X-ray diffraction is a common technique to study of crystal structures and atomic spacing and it is based on constructive interference of monochromatic X-ray and crystalline sample. The X-rays are generated by a cathode ray tube, then filtered to produce monochromatic radiation, collimated to concentrate, and directed towards the sample. The interaction of the incident rays with the sample produces constructive interference (and a diffracted ray) when conditions satisfy Bragg's Law ($n\lambda = 2d \sin \theta$). This law relates the wavelength of electromagnetic radiation to the diffraction angle and the lattice spacing in a crystalline sample (Moore and Reynolds, 1989). These diffracted X-rays are then detected, processed and counted. By scanning the sample through a range of 2θ angles usually 5^o to 70^o (Stock and Cullity, 2001), all possible diffraction directions of the lattice is attained due to the random orientation of the powdered material. Conversion of the diffraction peaks to d-spacings allows identification of the mineral because each mineral has a set of unique d-spacings. Typically, this is achieved by comparison of d-spacing with standard reference patterns. The outcomes of SEM and XRD analyses of two studied sandstones are given below:

3.1.1.1 Red Wildmoor Sandstone

XRD analysis from the laboratory shows that the core plug is quartz-rich (69%) sandstone with well-rounded grains, with some angular feldspar (19%) and rock fragments less than 4% (Table 3.2). These values agrees well with previous analysis carried out by Moghadam et al. (2014); Spears (1983), Benton et al. (2002) and Mavko et al. 2009 (Table 3.2).

Table 3.2 Mineral composition of Red Wildmoor as determined by whole rock XRD analysis in this study compared to others literature (Benton et al., 2002; Spears, 1983).

Mineral	Red Wildmoor Weight (%)	Literature average Weight (%)
Quartz	69	79
K-Feldspar	19	19
Dolomite	-	-
Siderite	-	-
Kaolinite	1.1	-
Albite	8.3	2
Mica 2M1	3	-

Table 3.3 Mineral characterization of Red Wildmoor Sandstone (Mavko et al., 2009)

Phase	wt%	μs (Gpa)	Kmin(Gpa)	Poisson ratio	K-Voigt	K-Reuss
Quartz	0.69	44	37	0.08	25.604	0.019
Kaolinite	0.01	1.5	1.4	0.14	0.0154	0.008
K-Feldspar	0.19	28.10	55.40	0.32	10.304	0.003

Albite (high)	0.08	28.60	56.90	0.28	4.7227	0.001
Mica, 2M1	0.03	41.1	61.5	0.23	1.722	0.0005

According to Bjørnevoll et al. (2002), Red Wildmoor sandstone core plugs has a mean grain diameter of 0.0107 mm with a porosity of 25%. The measured porosity of the sample was between 20.4% and 24.4% (Fig. 3.1), with an average value of 22%. The red colour is due to thin coating with pores lining smectite with microcrystals of goethite and amorphous iron around the grains.

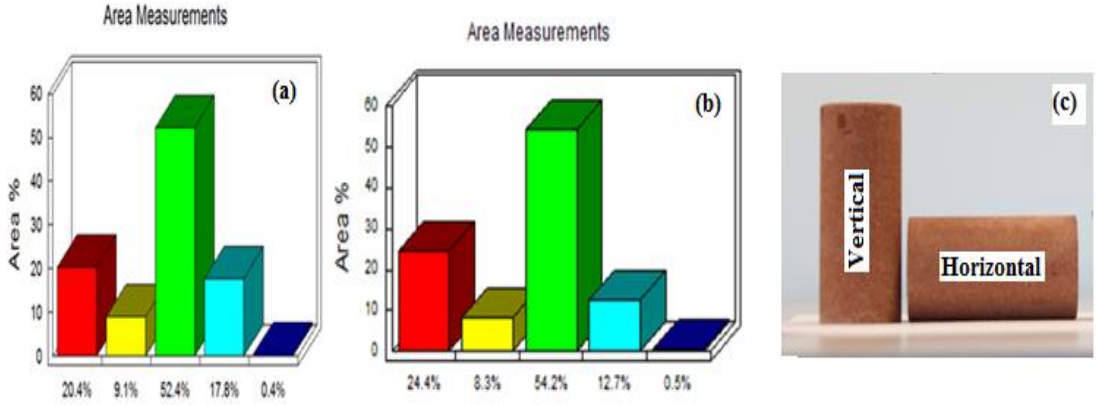

Figure 3.1 Porosity estimation for (a) horizontally and (b) vertically drilled Red Wildmoor core plugs using SEM analysis. The red column indicates porosity, yellow is kaolinite, green is quartz, light blue is k-feldspar and dark blue is heavy minerals. The drilled vertical and horizontal core plugs of Red Wildmoor Sandstone are also shown (c).

SEM analysis reveals that both vertically and horizontally drilled Red Wildmoor core plugs have similar mineral composition (Figs. 3.2 and 3.3). The grain size of the sandstones ranges from medium to very fine grained (Spears, 1983)

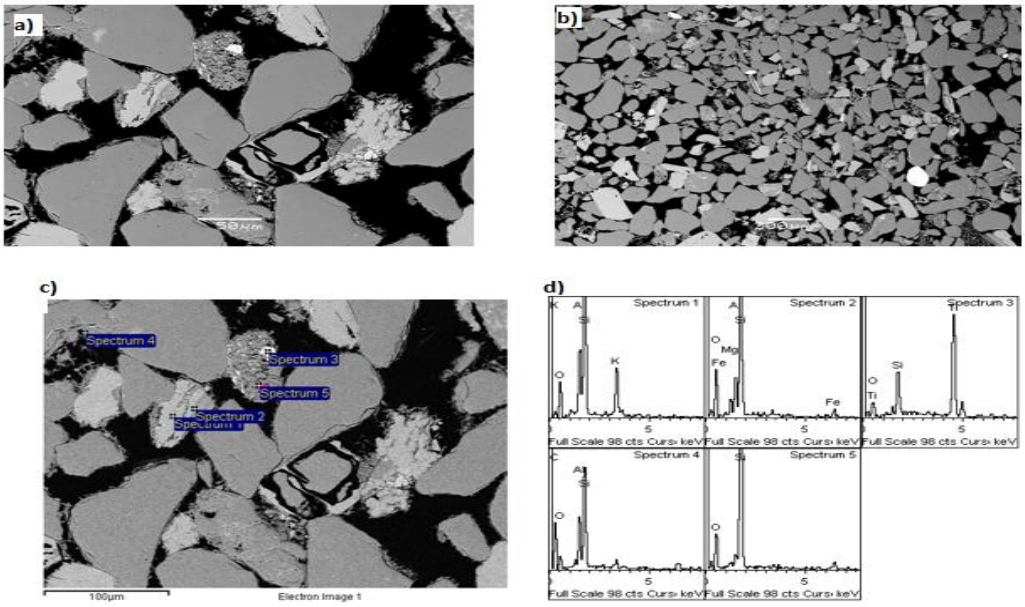

Figure 3.2 SEM images of Red Wildmoor core plugs at three different magnifications (a) 50 µm, (b) 200 µm and (c) 100 µm. d) Results from analysed section presented in (c) showing K-feldspar, Muscovite, Rutile, Illite and quartz respectively.

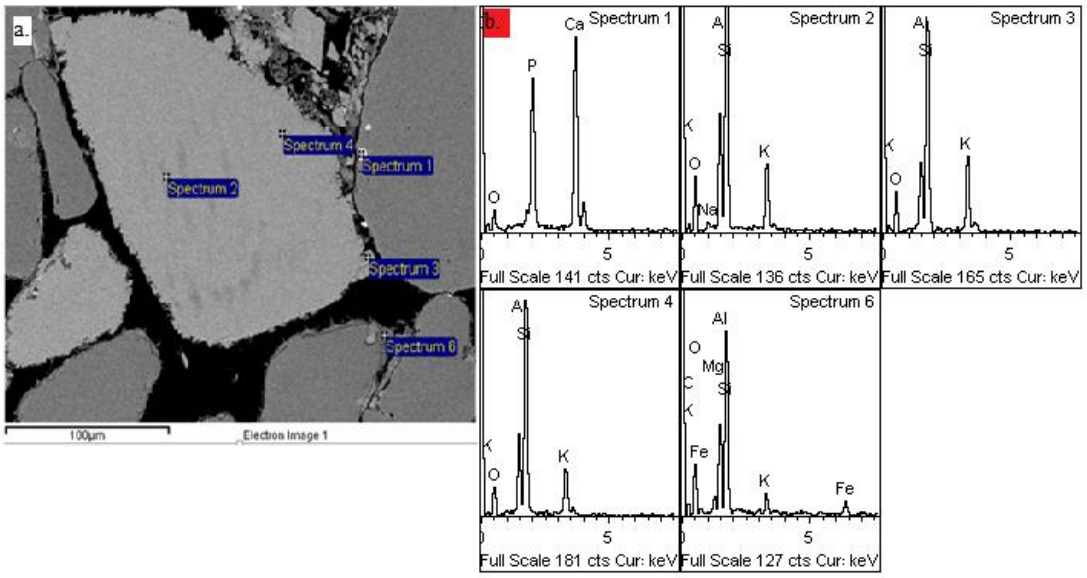

Figure 3.3 Red Wildmoor vertical core plug SEM and EDS spectra. Spectrum 1 is Appatite, spectrum 2, 3 and 4 are K-feldspar, and spectrum 6 is Smectite.

3.1.1.2 Berea Sandstone

Berea sandstone is a medium-grained Mississippian age greywacke whose grains are predominantly sand-sized and are composed of quartz held together by silica. It has relatively high permeability and porosity and this makes it a good candidate for reservoir rock. The Berea sandstone has been used in several studies (Azari and Leimkuhler, 1990a; Berryman and Blair, 1987; Dawson et al., 2014; Hart and Wang, 1995; Mathieu, 2007; Van Den Abeele et al., 2002; Wissler and Simmons, 1985; Wyllie et al., 1956). According to Hart and Wang

(1995), its grains are well sorted (155mm) and sub-angular with quartz overgrowths with a porosity of 19%. A summary of petrophysical properties of Red Wildmoor and Berea Sandstone core plugs are presented in Table 3.5.

Table 3.4 Mineral characterization of vertical Berea sandstone core plug from Mavko et al. (2009), Azari and Leimkuhler (1990b) and Dawson et al. (2014).

Phase	wt%	μs (Gpa)	Kmin(Gpa)	Poisson ratio	K-Voigt	K-Reuss
Quartz	0.70	44.00	37.00	0.08	26.018	0.019
Mica 2M1	0.05	41.1	61.5	0.23	3.062	0.0008
Kaolinite	0.05	1.5	1.4	0.14	0.064	0.0327
Siderite	0.01	51.00	123.70	0.32	1.048	0.00006
Calcite	0.00	32.00	76.80	0.32	0.214	0.00004
Albite	0.03	28.60	56.90	0.28	1.741	0.0005
Dolomite	0.11	45.00	94.90	0.30	10.771	0.001
K- Feldspar	0.05	28.10	55.40	0.32	2.537	0.0008

Table 3.5 Summery of Red Wildmoor and Berea sandstone's petrophysical properties.

Core plug	Kmin(Hills) (GPa)	μmin(Hills)(GPa)	μmin-frame(GPa)	Kframe(GPa)
Vertical RW	36.892	34.639	6.120	6.453
Horizontal RW	36.892	34.639	5.769	9.241
Berea	31.775	15.325	19.6	11.009

Rock sample surfaces were analysed using SEM-EDS to survey the sample mineralogy. SEM analysis indicated that Berea sandstone sample is predominantly quartz, and contain feldspar grains and Fe-Ca-Mg-carbonate cements (Fig. 3.4). Pore space is partially occluded by clays and carbonate cements of variable composition and this contributes to its low permeability and porosity. Standard analysis from SEM shows that the Berea sandstone contains predominantly quarts with few mica flakes as shown in Figure 3.4.

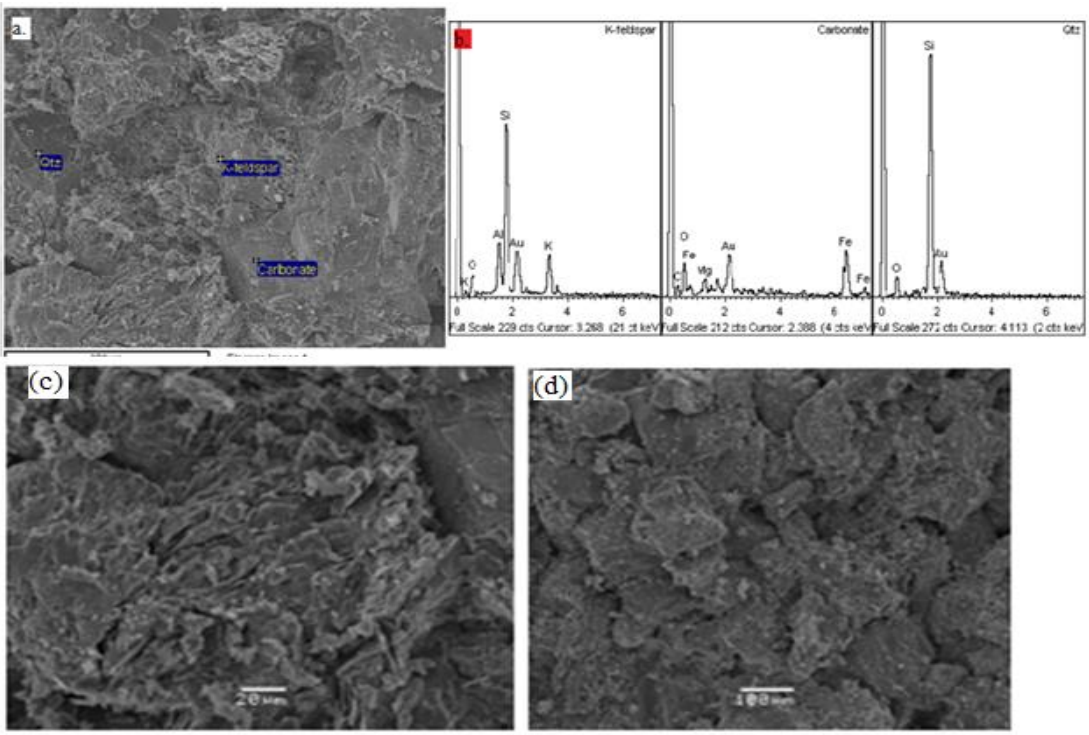

Figure 3.4 SEM analysis and EDS spectra for Berea (a and b). SEM micrograph reveals detrital grains. Most of the grains are quartz and the finer grained materials kaolinite. Sheet-like kaolinite results in low permeability due to clay cementation (c and d).

3.2 Experimental techniques

In this study, ultrasonic pulse transmission and electromagnetic techniques were used to acquire acoustic velocity and electrical resistivity measurements on two Red Wildmoor and Berea sandstone samples. In order to mimic typical in-situ field pressure conditions in injection reservoirs, the tests are conducted in a hydrostatic pressure vessel using liquid CO_2. The hydrostatic pressure cell can withstand a confining and pore pressures of up to 30 MPa and temperature up to 80^{o}C. A summary of the setup is shown in Figure 3.5

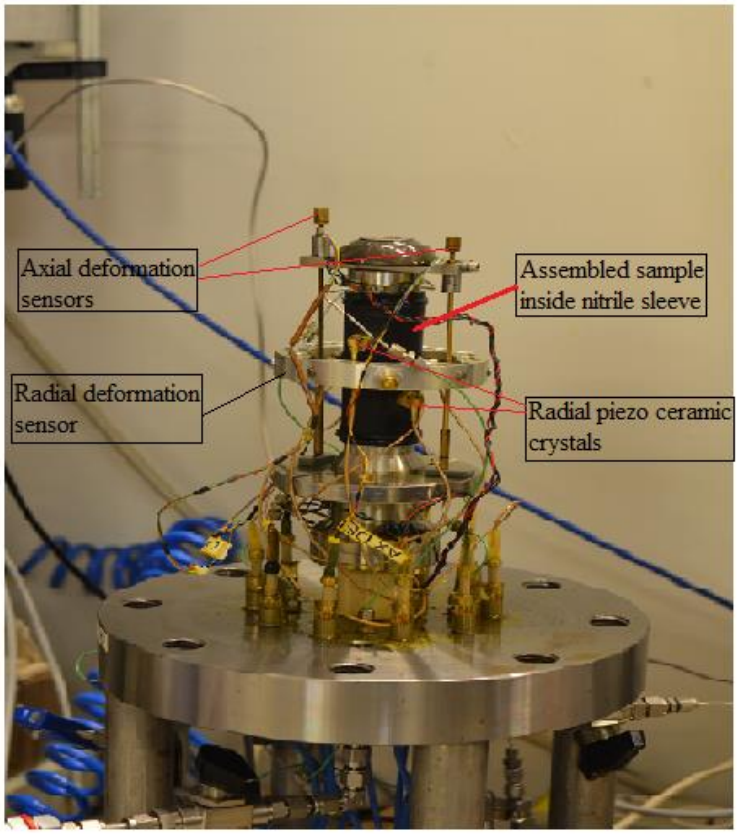

Figure 3.5 Fully prepared and assembled sample ready for measurement. The sample is placed inside a nitrile sleeve instrumented with piezo ceramics which measures radial velocity and resistivity. The axial and radial deformation sensors records axial and radial deformations respectively. O-rings are used to prevent leakage between sample and silicon oil.

3.2 Experimental setup

The pressure vessel is instrumented with pressure sensors that measure confining and pore pressure. Linear variable differential transformer (LVDT) strain gauges are directly mounted onto the nitrile sleeve and accurately measure axial and radial deformation. An array of P-wave piezo-ceramic crystals embedded onto the sleeve at three different levels across the sample cross-section (Fig. 3.7) enable measurements of radial acoustic velocities and resistivity. There are varieties of laboratory methods that can be used to determine the elastic properties in a rock sample among them stress-strain curve , forced oscillation, and pulse transmission (Shi et al., 2007a). The pulse transmission is the most widely used ultrasonic methods in rock physics.

To generate both Vp and Vs waves in ultrasonic transmission experiments, piezoelectric ceramics are usually used. These materials have the capability to produce electrical potential when subjected to a mechanical stress, and this effect is linearly reversible such that when an electrical potential is applied, the material will exhibit mechanical strain or mechanical vibration. Thus, a piezoelectric element can be used as both a transmitter and receiver. The type of vibration generated is determined by the polarization of the lattice molecules that

makes a piezoelectric crystal. If the material is axially polarized axial compression and expansion occurs in the material when voltage is applied generating out-of-plane vibration or P-waves, while if the material is laterally polarized S-waves are generated. The arrival of the wave at the receiver is detected and recorded by a digital oscilloscope.

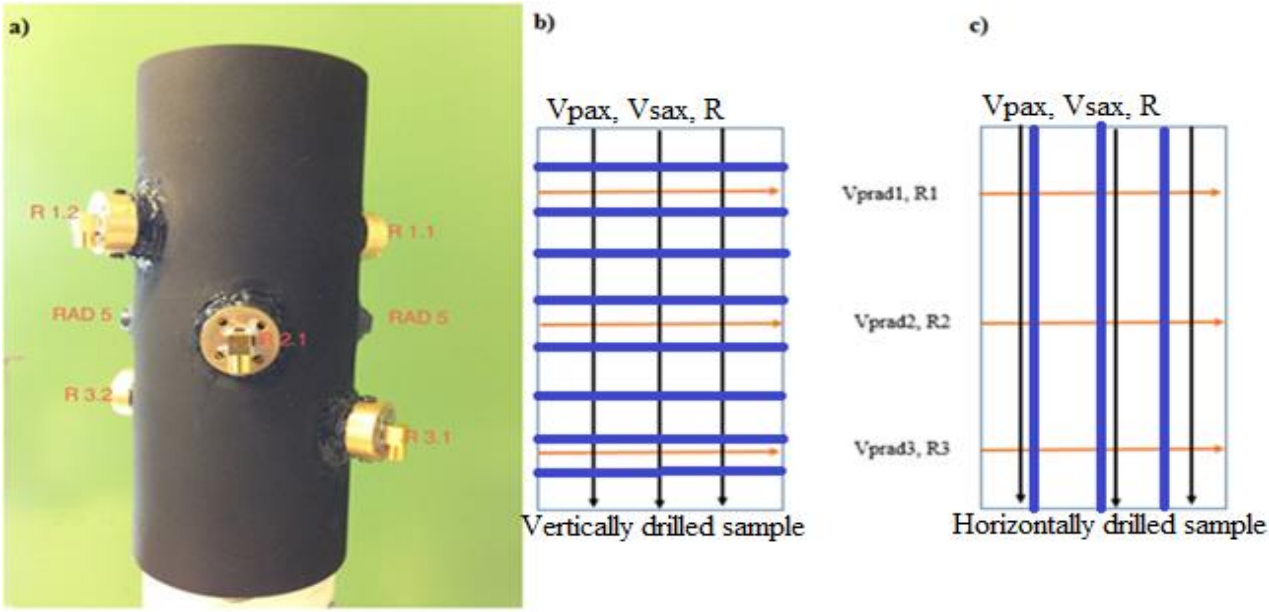

Figure 3.6 (a) Nitrile sleeve with array of P-wave piezo-ceramic crsytals. R1.1 and R1.2 are top radial transmitter and receiver sensors, R2.1 and R2.2 are middle and R3.1 and R3.2 are bottom. Rad 5 is the radial deformation sensor. (b) vertical drill configuration , and (c) horizontal drill sample configuration. The red arrow are radial measurements, the black are axial and the dark blue lines are the beddings.

Experimental setup used in this study are adopted from Alemu et al. (2011b) and Alemu et al. (2013) and resistivity measurement are based on suggestion from Wang et al. (2009). Few modifications were made to measure acoustic velocity and electrical resistivity in four directions: one axial and three radial (Fig 3.6 b and c). The main components used in the experimental setup include pressure vessel, pressure gauge, a pulse generator digital oscilloscope and a logging station where cell pressure, pore pressure, flow rate and volume are controlled and recorded.

The core plug and the transducers assemblage are placed in a silicon-oil filed vessel, which serves as the pressurizing medium for providing hydrostatic confining pressure onto the sample. The system allows continuous injection of fluids into the sample at room temperature. The confining and pore pressure systems are independent of each other such that different pressure conditions can be applied independently by using the GDS and ISCO pumps located outside the pressure vessel. Both pumps are used to keep a constant pressure and control flow rate during injection. Table 3.6 show a summary of pressure conditions during the test.

Table 3.6 Summary of runs and conditions applied for each test.

Pore fluid	Pressure conditions (MPa)			Measurement
	Effective pressure	Confining pressure	Pore pressure	
Dry	1-15	1-15	0	P- and S-wave.
CO_2	1-15	11-25	10	P- and S-wave, resistivity.
Brine	1-15	11-25	10	P- and S-wave, resistivity.
Drainage	15	25	10	P- and S-wave, resistivity.
Imbibition	15	25	10	P- and S-wave, resistivity.

Experimental setup pertaining to generating and recording of elastic waves consists of pulse generator, and a digital oscilloscope. The pressurizing system controls both confining pressure and pore pressure. The confining pressure is the external pressure applied onto the surface of the sample while pore pressure is the pressure of the fluid inside the samples' pore space. The top and bottom cap of the cell are electrically separated such that electrical resistivity across the sample can be measured. The pumps connected to the top cap are separated from the rest of the system using peek tubings to avoid current leakage during the test. Transducers are the main components of pulse transmission measurements. In order to transmit and receive an elastic wave in the laboratory, ultrasonic transducers were made to accommodate cylindrical core samples with a standard diameter of about 38 mm and height 78 mm. The main components of ultrasonic transducers are aluminium end caps, and P- and S- wave piezoelectric ceramics. During the loading and unloading tests, the samples were subjected to a series of measurements including resistivity and velocity for dry conditions, fully saturated CO_2 conditions, fully brine saturation, drainage (CO_2 reinjection) and imbibition (brine reinjection). All measurements were carried out at room temperature and all the steps involved acquisition of P and S- waveforms.

(i) Dry test

For the dry loading and unloading, the samples are tested under drained conditions ($\Delta P_{fluid} = 0$). Mechanical data is collected by increasing the cell pressure form 1-15 MPa in 7 hours then down to 1 MPa with a 30 minutes break. This procedure is repeated three times to ensure that sensors and the nitrile sleeve have a tight contact. The sample is then vacuumed. Only one GDS pump is used (Fig.3.7).

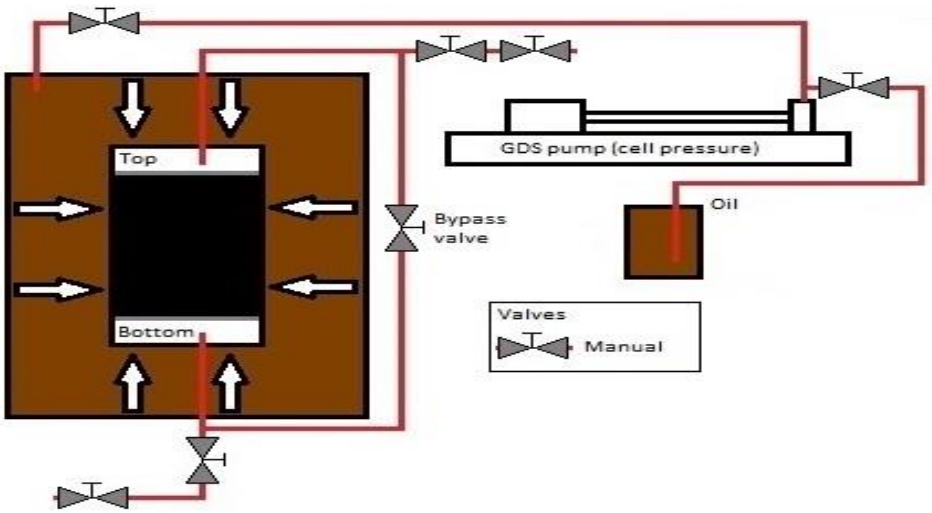

Figure 3.7 Setup for dry test.

(ii) Fully CO_2 saturated test

In this step, the sample is saturated with liquid CO_2, at 10 MPa. The cell pressure is kept at 11 MPa while injecting liquid CO_2 to achieve 1 MPa effective pressure. The GDS pump control is then used to increase the cell pressure from 11 to 25 MPa then back to 11 MPa in 7 hours with a break of 30 minutes while maintaining a constant pore pressure of 10 MPa (Fig. 3.8). This ensures that an effective pressure of 1-15 MPa is achieved during both loading and unloading. At the end of the experiment, the samples were vacuumed to expel CO_2 from the sample before injecting brine.

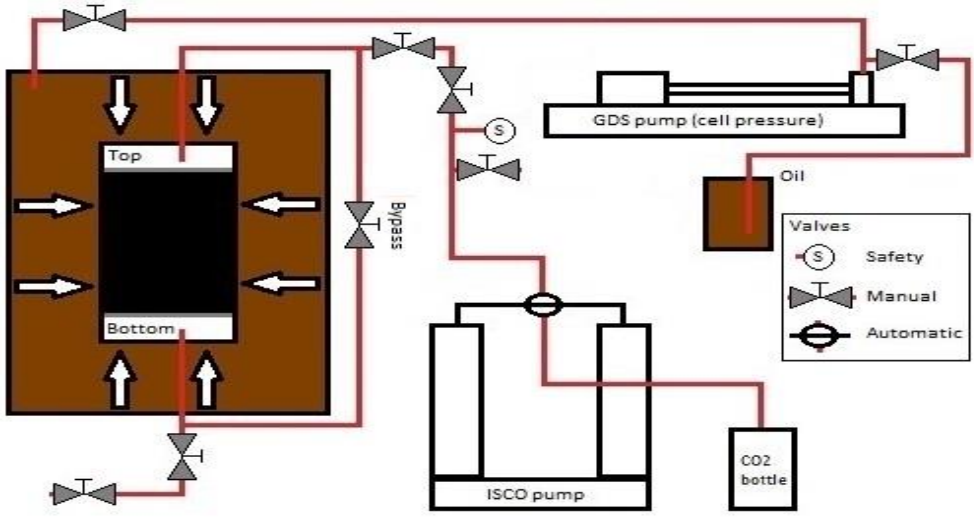

Figure 3.8 Setup for fully CO_2 saturated injection.

(iii) Fully brine-saturated test

During this step, synthetic brine solution with 30 g/l NaCl is injected into the sample. Due to brine's corroding effect on GDS pump pipes, oil-water-contact (OWC) is established as shown Figure 3.9 to prevent brine from getting into the pump. After achieving a pore pressure of 10 MPa, the same procedure as in step two for CO_2 saturated run is followed.

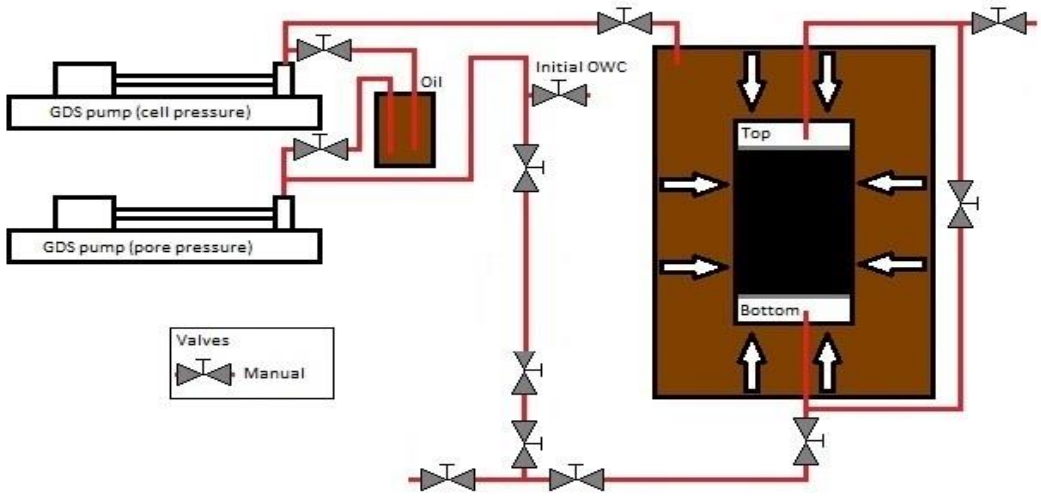

Figure 3.9 Setup for fully brine-saturated test.

(iv) Drainage (CO_2 injection into brine-saturated sample)

In this step, liquid CO_2 is reinjected from ISCO syringe pump into the brine saturated sample from the top at a cell pressure of 25 MPa, pore pressure of 10 MPa and effective pressure of 15 MPa. The bypass valve is closed and only the top and bottom valves are opened. A second GDS pump is connected to the bottom of the sample to act as a backpressure to ensure that the pore pressure is kept constant at 10 MPa. Injection is then done at increasing pore volume (PV) starting from 0.1 to 0.9 and then 1 to 10. Between 0.1 and 1PV flow rate of 0.5mL/min (120msec/mm^3) was used and, 2.5mL/min (24msec/mm^3) between 1-10 PV (Fig. 3.10). Measurements were taken for both axial and radial resistivity and velocity for each PV injected.

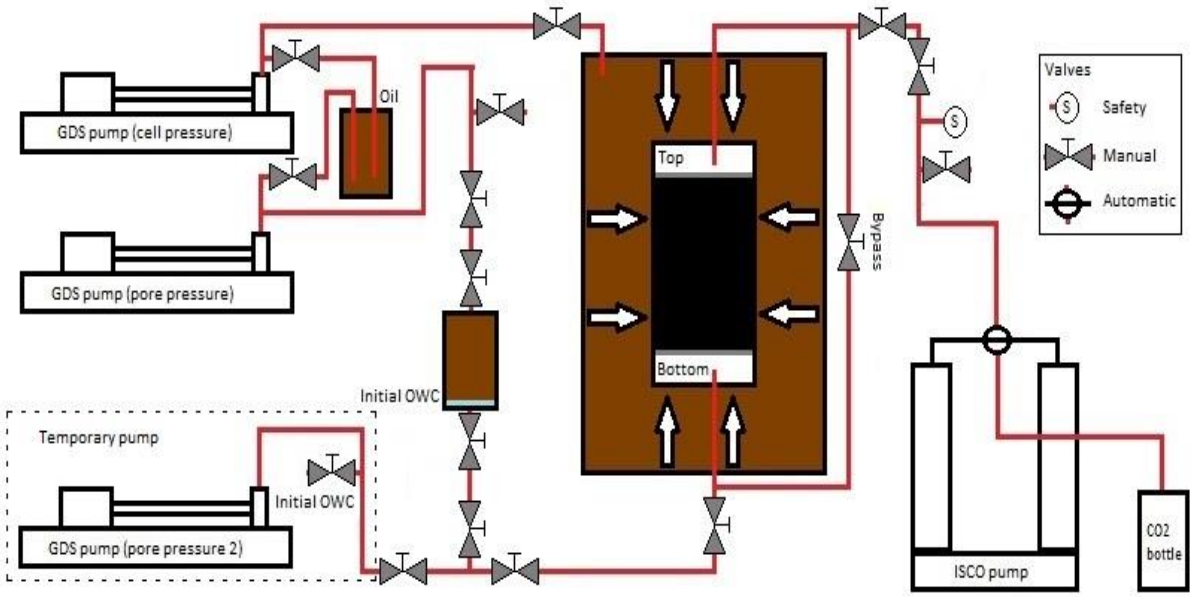

Figure 3.10 Setup for drainage.

(v) Imbibition (brine injection into CO_2 saturated sample)

In this step, injected CO_2 is pushed out of the sample from the bottom using 30g/l of synthetic brine (NaCl). A brine-CO_2 separator cylinder is used to separate CO_2 and brine from the sample. The top of the brine-CO_2 cylinder is connected to the ISCO pump while the bottom is connected to the top of the sample (Fig. 3.11). ISCO pump acts as the backpressure to ensure a constant pore pressure of 10 MPa during brine injection. The same procedure and pressure conditions were repeated similar to four above. Table 3.7 shows flow rate and pore volume injected into the core plugs during both drainage and imbibition.

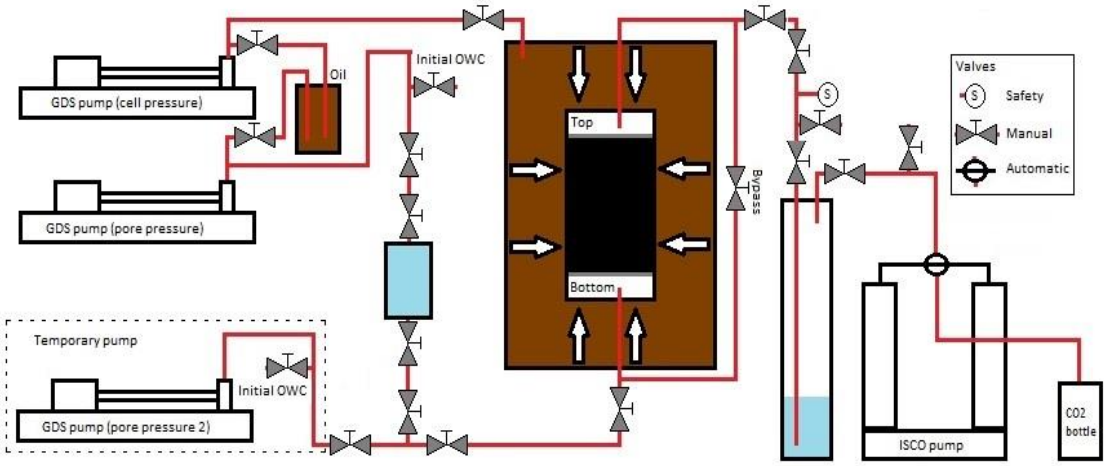

Figure 3.11 Setup for imbibition.

Table 3.7 Flow rate and pore volume (PV) steps during drainage and imbibition.

Flow rate	0.5mL/min										2.5mL/min				
PV drainage	0.1	0.2	0.3	0.4	0.5	0.6	0.7	0.8	0.9	1	2	4	6	8	9
PV imbibition	0.1	0.2	0.3	0.4	0.5	0.6	0.7	0.8	0.9	1	2	4	6	8	9

3.3 Sample preparation

Cylindrically shaped sandstone rock samples with varying diameters and heights were used. In order to minimize inaccuracy in velocity measurements, the samples were smoothened at both ends. The samples were then placed inside a nitrile configured with piezoelectric ceramic crystals to measure both axial and radial velocity and resistivity respectively. To prevent hydraulic oil from contaminating the sample, filters were used at both ends and an O-ring was placed around the nitrile sleeve to tighten it to the transducers and ensure the sample is free from leakage (Fig. 3.5).

Table 3.8 Summery of sample properties used in the study.

Sample	Mass [g]	Height [mm]	Diameter [mm]	Area [cm^2]	Volume [cm^3]	Volume [cm^3]
Red Wildmoor vertical	166.54	77.80	37.87	11.262	87.61	87.61
RedWildmoor horizontal	173.34	79.93	37.89	11.276	90.13	90.13
Berea 15-20 mD	192.31	78.91	36.89	10.689	84.34	84.34

3.4 Velocity and resistivity calculation

Prior to determining P- and S- wave velocities from the acquired waveform, the measuring instruments were calibrated. To calculate the average actual time required for signal to travel through the sample, the arrival time for P- and S- waves for both axial and radial waves were measured with and without the sample. Due to the effect of pressure, these measurements were undertaken at an effective stress of 15 MPa. This enables us to calculate the effect of aluminium buffer caps on the axial direction and nitrile sleeve along the radial direction.

Figure 3.12 shows first arrival signals for the axial and radial P- and S-wave respectively without sample under a confining pressure of 15 MPa. By determining the difference in arrival time of signal setup with sample (T_w) and the signal for setup without sample (T_{wo}), the travel time of the signal through the sample (T_f) can be determined. The velocity through the sample is then determined from the time and the length of the sample, L_s using Equation 3.1. The height and diameter of the samples are used for axial and radial velocity and resistivity calculations respectively.

$$v = \frac{L_s}{T_f} = \frac{L_s}{T_w - T_{wo}} \qquad \text{Eq. 3.1}$$

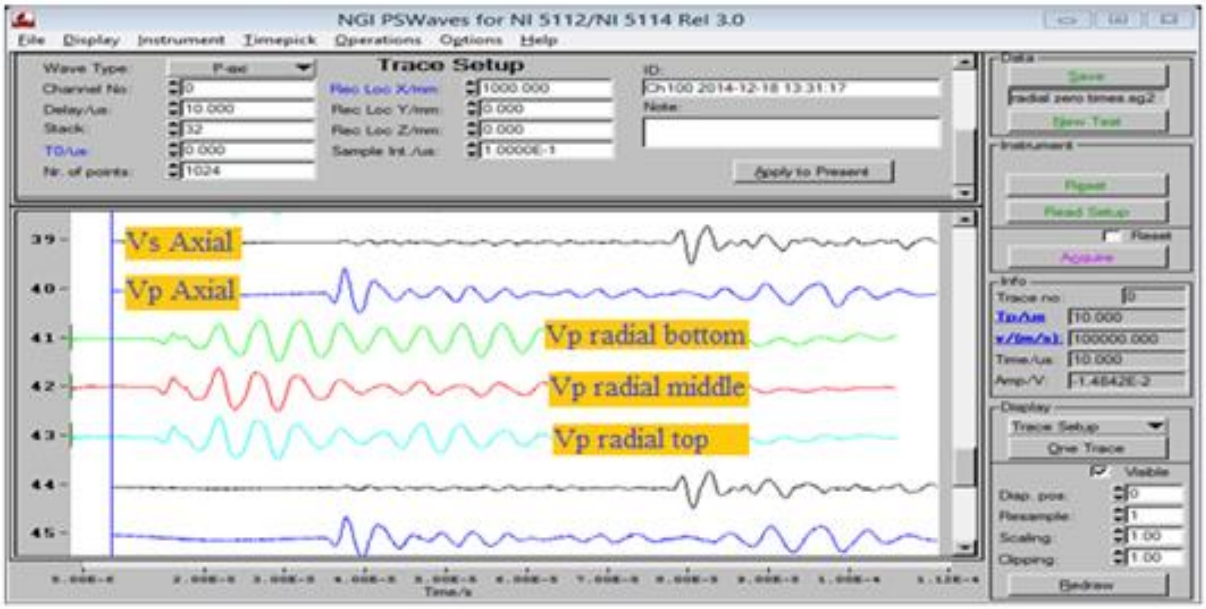

Figure 3.12 Screenshot from PSwave software for determining first arrival of radial P-waves with dummy sample.

Using measured values of electrical DC conductivity of brine saturated cores from wide variety of sand formations, Archie formulated an empirical law for the relationship between resistivity and relative saturation of porous medium.

$$I = \frac{R_t}{R_0} = \frac{b}{S_w^{-n}} \qquad \text{Eq. 3.2}$$

Where *I* is the resistivity index, *Ro* is the resistivity of the porous media fully saturated with brine, *Rt* is the resistivity of the media saturated with brine and non-wetting fluid, *Sw* is the water saturation, *b* is an empirical constant equal to 1, and *n* is the saturation exponent. For the vertical and horizontal to bedding Red Wildmoor core plugs, resistance was measured only along axial and one radial (at the middle) while for Berea, axial and three radial (top, middle, and bottom) measurements were made. Equation 3.3 was used to calculate resistivity from resistance measured in the laboratory.

$$\rho = \frac{R \cdot A}{l} \ [\Omega \cdot m] \qquad \text{Eq. 3.3}$$

To account for variation in radial resistivity due to anisotropy and tortuosity during fluid movement in the sample, a correction factor *Fcorr* (Eq. 3.6) was used to correct the measured resistivities. To perform this, one assumes that synthetic resistivity of the sample *ρknown*, the sample geometry (Eq. 3.5), and synthetic voltage difference between two radial electro-nodes u_+ and u_- are known.

$$R_{calc} = \frac{u_+ - u_-}{I_{FEM}} - \text{Calculated resistance} \qquad \text{Eq. 3.4}$$

$$F_{geo} = \frac{A}{L} = \frac{\rho_{known}}{R_{calc}} - \text{Calculated resistance} \qquad \text{Eq. 3.5}$$

$$F_{corr} = \left(\frac{F_{geo}}{\frac{A_{elecronode}}{D_{sample}}} \right) - \text{Correction factor} \qquad \text{Eq. 3.6}$$

$$R = Rs \left(\frac{A_{Electrode}}{D_{sample}} \right) F_{cor} \text{ - Calculating resistance using resistivity factor} \qquad \text{Eq. 3.7}$$

ρ is the resistivity in Ω-m, l is the length in meters, R is the resistance in Ω, *Rcalc* is calculated resistance based on electro-nodes, *Fgeo* is geometry factor which is a function of the area and length of the sample, *Aelectronode* is the area of the electrodes, *Dsample* is the height of the sample in meters and A is the cross-sectional area in m^2. Figure 3.13(a) shows the graph for determining the correction factor and (b) the finite element (FE) model showing electric field and current density arrow.

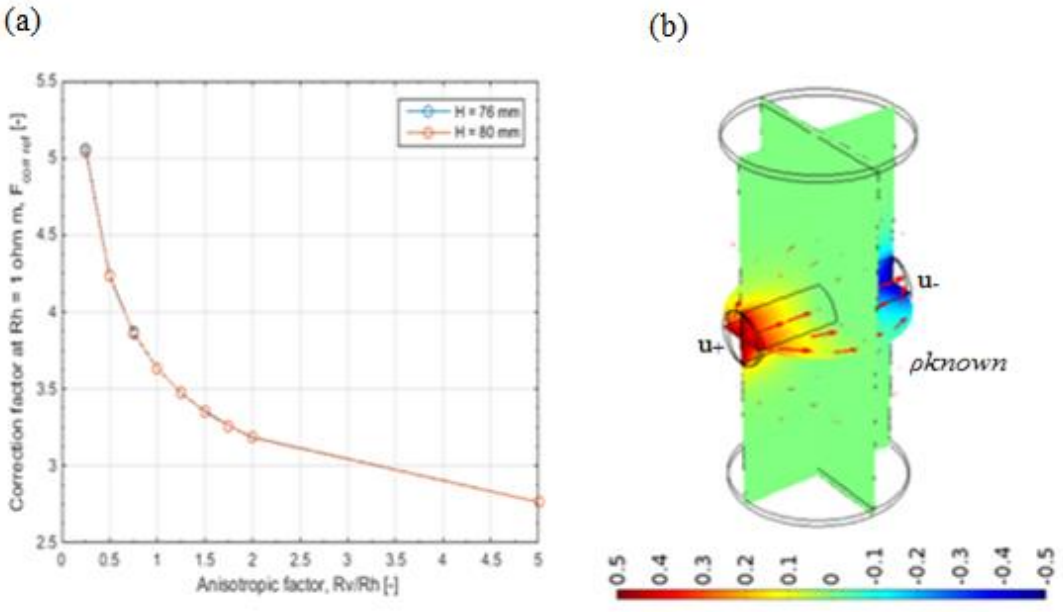

Figure 3.13 Reference correction factor and FE model.

Table 3.9 Resistivity properties for vertically drilled Red Wildmoor

	Axial	Radial	Unit
Length	79.72	37.78	[mm]
Electrode diameter	38.00	12.00	[mm]
Area of electrode	0.001134	0.000113	[m^2]
Fcorr	1	3.70	

Table 3.10 Resistivity properties for horizontally drilled Red Wildmoor

	Axial	Radial	Units
Length	77.52	37.60	[mm]
Electrode diameter	38.00	12.00	[mm]
Area of electrode	0.001134	0.000113	[m^2]
Fcorr	1.00	3.53	

Table 3.11 Resistivity properties for Berea 20-50mD

	Axial	Rad(Top)	Rad(Mid)	Rad(Bot)	Units
Length	78.83	36.8	36.8	36.8	[mm]
Electrode diameter	38.00	12.00	12.00	12.00	[mm]
Area of electrode	0.001134	0.000113	0.000113	0.000113	[m^2]
Fcorr	1	3.934	4.14	4.327	

Chapter 4: Acoustic velocity measurements

In this chapter, laboratory results on acoustic wave velocity of the three studied sandstone core plugs and petrophysical characteristics are given. Results used in this chapter were acquired from measured velocities explained in chapter 3.

4.1 Results

4.1.1 Red Wildmoor horizontal core plug

4.1.1.1. Saturated conditions

P- and S-wave velocities for dry, and fully CO_2 and brine-saturated condition were made prior to flooding. These measurements were then used to understand the saturation level of the sample during drainage and imbibition. During loading and unloading for dry conditions, Vp increased with increasing confining pressure from 1-15 MPa and Pp = 0 MPa. For CO_2 and brine-saturated conditions, the differential confining pressure was between 1-15 MPa with Pp = 10 MPa. For the saturated conditions, Vs for dry has the highest velocity followed by CO_2 then brine (Fig. 4.1). For Vp, fully brine-saturated is the highest, followed by dry then CO_2.

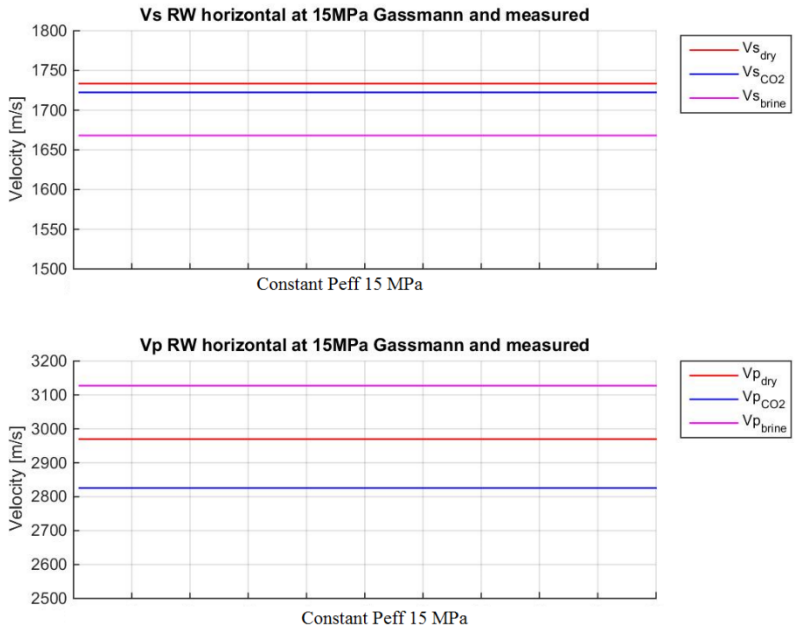

Figure 4.1 Axial P- and S-wave velocities for dry, CO_2 and brine-saturated conditions at 15MPa.

4.1.1.2. Drainage (CO_2 injection)

Both P- and S-wave velocities were measured at room temperatures (T ≈ 23 ^{o}C) where CO_2 is in liquid phase at a differential pressure of 15 MPa and pore pressure of 10 MPa. After

injecting 8 PV of CO_2 in the pore spaces, the Vs increases by 2%. In comparison to saturated conditions, measured axial Vs increases from fully brine saturated values to almost fully CO_2 saturated (Fig. 4.2). The Vp decreases significantly after injection of 1 PV CO_2 and does not seem to be affected significantly with additional injection of CO_2 beyond 4 PV. In total 8 PV of CO_2 was injected. CO_2 saturation was calculated using Equation 2.9. The Vp measured at maximum CO_2 saturation using of ca. 39% is 9% lower than fully brine-saturated velocity and only 1% higher than the value measured at 100% CO_2 saturation. In term of injection rate, there is an increase in Vs with increase in injection rate from 0.5mL/min to 2.5 mL/min.

Table 4.1 CO_2 [mL] injected into Red Wildmoor horizontal plug (1 PV = 20.73 mL).

Flow rate	0.5mL/min							2.5mL/min				
PV	0	0.1	0.3	0.5	0.7	0.9	1	2	4	6	8	9
Injected CO_2 [ml]	0	4.07	8.22	12.36	16.51	20.66	22.73	43.46	84.92	126.38	167.84	188.57

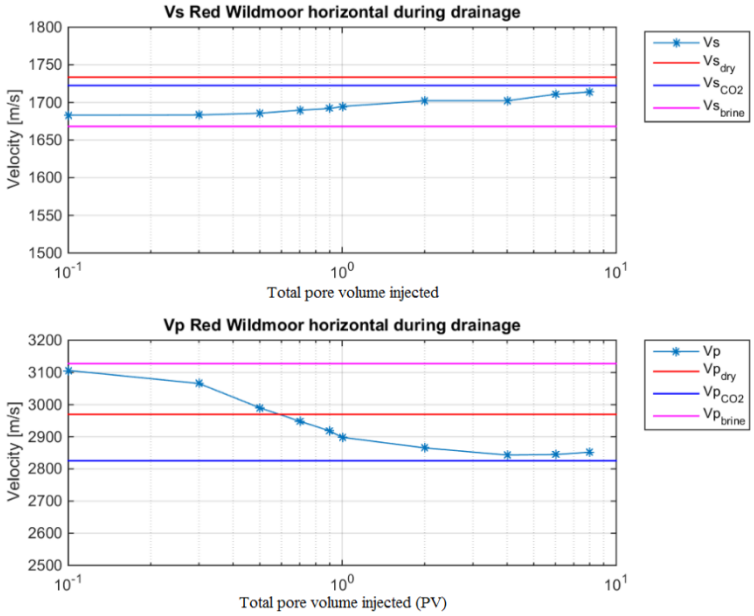

Figure 4.2 Axial P- and S-wave velocities during drainage compared with saturated conditions.

For radial P-wave velocities, top Vp decreases first followed by middle then bottom as CO_2 is injected from the top (Fig. 3.4). The radial Vp measured at maximum CO_2 (42%) decreased by -14%, -7% and -7% for the top, middle and bottom respectively from fully brine-saturated values and are 6%, 4% and 7% respectively higher full CO_2 saturation. The effect of change in flow rate is not evident for the radial measurements.

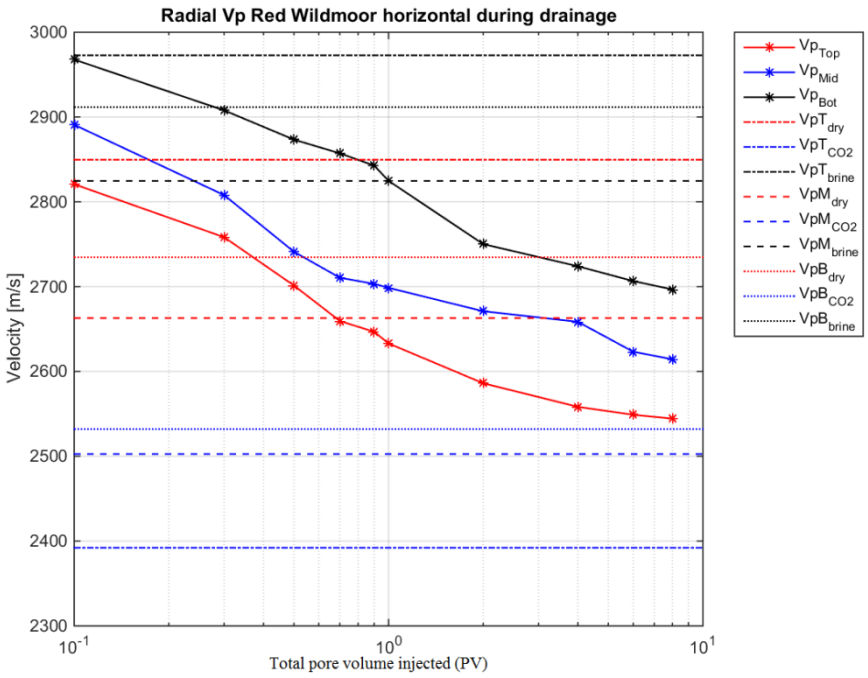

Figure 4.3 Radial P-wave velocities during drainage compared with saturated conditions for top, middle and bottom.

4.1.1.3. Imbibition (brine injection)

Figure 4.4 shows a slight decrease in axial Vs with increasing brine injection. Measured Vs decreases by -2% during imbibition and is 1% higher than Vs at fully brine-saturated conditions. P-wave velocity increases with increase in brine injection and it increases by 8% during imbibition. The measured velocity is 1% lower than measured values at fully brine-saturated. For the radial Vp velocities, there is a general increase during imbibition. Bottom Vp increases first followed by middle then top as shown in

Figure 4.5 since brine is injected from the bottom to the top of the sample. There is a significant increase in Vp with change in flow rate from 0.5ml/min to 2.5mL/min between 2-8 PV. At the end of imbibition, bottom velocity is almost equal to measured values at fully brine-saturated while the middle is 2% higher. The top velocities are 5% lower than measured values at fully brine-saturated.

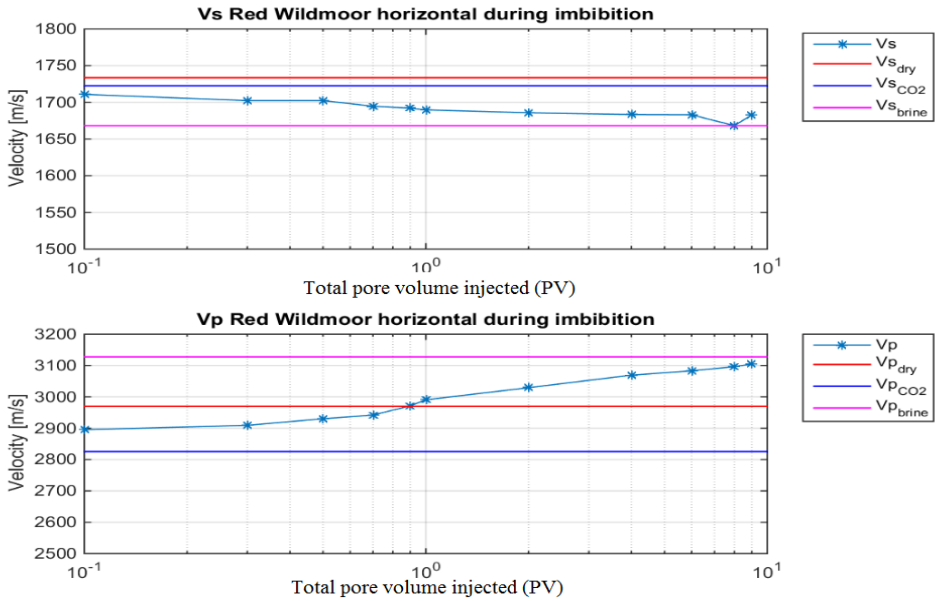

Figure 4.4 Measured axial P- and S-wave velocities during imbibition compared with saturated conditions.

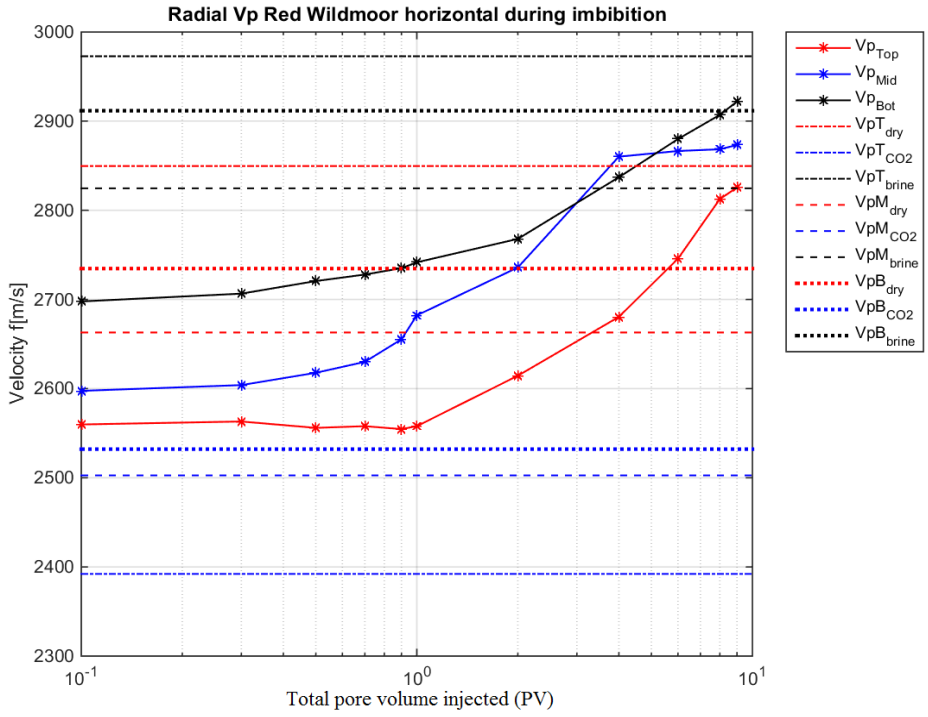

Figure 4.5 Radial P-wave velocities during imbibition compared with saturated conditions for top, middle and bottom.

4.1.2 Red Wildmoor vertical core plug

4.1.2.1 Saturated conditions

P- and S-wave velocities for dry, CO_2 and brine-saturated condition were made prior to CO_2 flooding then compared to measured velocities after drainage and imbibition. Loading and unloading tests were carried out on the sample. Similar to vertical Red Wildmoor, Vp increased with increasing confining pressure from 1-15 MPa and Pp = 0 MPa for dry conditions. Vs for the dry test is the highest while brine has the lowest Vs (Fig 4.6). For Vp, fully brine saturated test has the highest, followed by dry then CO_2.

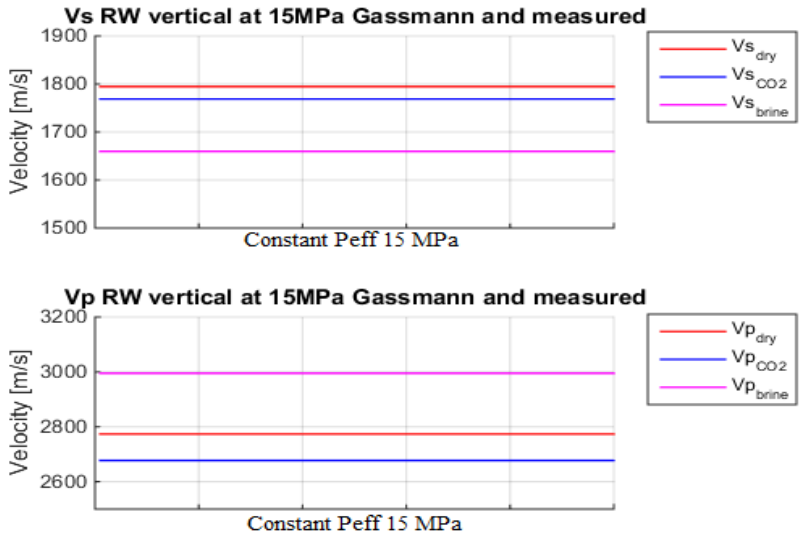

Figure 4.6 Axial P- and S-wave velocities for dry, CO_2 and brine-saturated conditions at 15 MPa.

4.1.2.2 Drainage (CO_2 injection)

From the results in Figure 4.7, Vs becomes sensitive to CO_2 after injecting 0.7 PV. In comparison to saturated conditions, axial Vs is much lower than measured dry and CO_2 saturated (Fig 4.7) and increases by 2% during drainage. Measured axial Vp decreases steadily with injection from 0 to 1 PV then decreases drastically between 2-6 PV as a result of change in flow rate from 0.5mL/min to 2.5mL/min then increases again until the end of drainage. In total 9 PV of CO_2 was injected and the Vp measured at maximum CO_2 saturation of ca. 35% is 8% lower than fully brine-saturated velocity and only 3% higher than the value measured at 100% CO_2 saturation. For the radial measurements, the top Vp drops first followed by middle then the bottom after injecting 9 PV as shown in

Figure 4.7. The radial Vp's measured at maximum CO_2 saturation (45%) decreased by -7%, -9% and -7% for the top, middle and bottom respectively from fully brine-saturated values and are 4%, 1% and 5% respectively higher than values measured at fully CO_2 saturation. The effect of change in flow rate is not evident for the radial measurements (Fig 4.8).

Table 4.2 CO_2 [mL] injected into Red Wildmoor vertical plug (1 PV = 19.00 mL)

Flow rate	0.5mL/min							2.5mL/min			
PV	0	0.1	0.3	0.5	0.7	0.9	1	2	4	6	8
Injected CO_2 [ml]	0	3.90	7.70	11.50	15.50	19.50	21.40	40.40	78.40	116.40	154.4

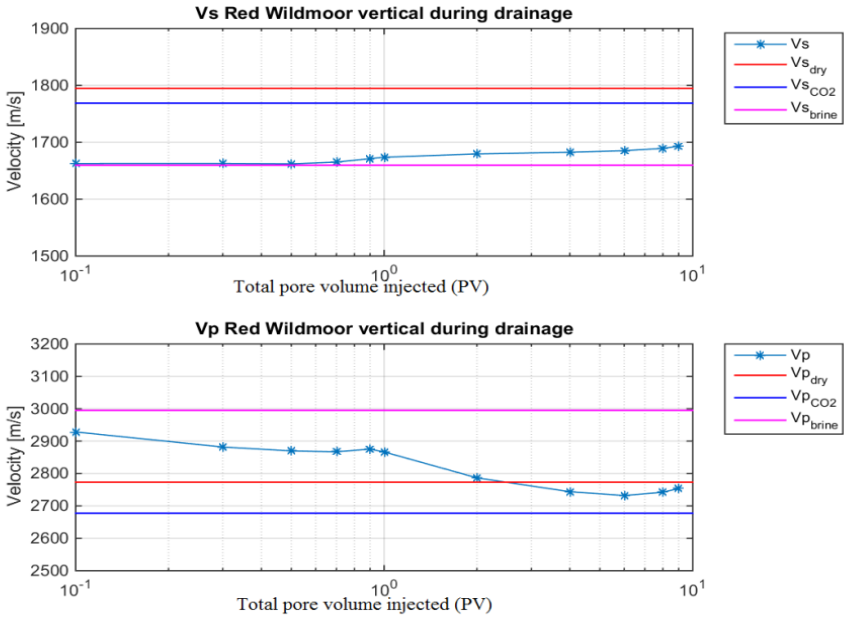

Figure 4.7 Measured axial P- and S-wave velocities during drainage compared with saturated conditions.

4.1.2.3 Imbibition (brine injection)

Measured P- and S-wave velocities are shown in Figure 4.9. Axial Vs decreases with increasing pore volume up to 1 PV then remains constant throughout imbibition (Fig 4.9). In comparison to saturated conditions, axial Vs is lower than both dry and CO_2 saturated conditions but is almost equal to Vs for brine saturated condition after injection of 2 PV. In overall, Vs decreases by -2% during imbibition. P-wave velocity increases with increase in brine injection and it increases by 11% during imbibition. After injecting 4 PV of brine, the measured Vp becomes slightly higher than Vp for fully brine saturated condition.

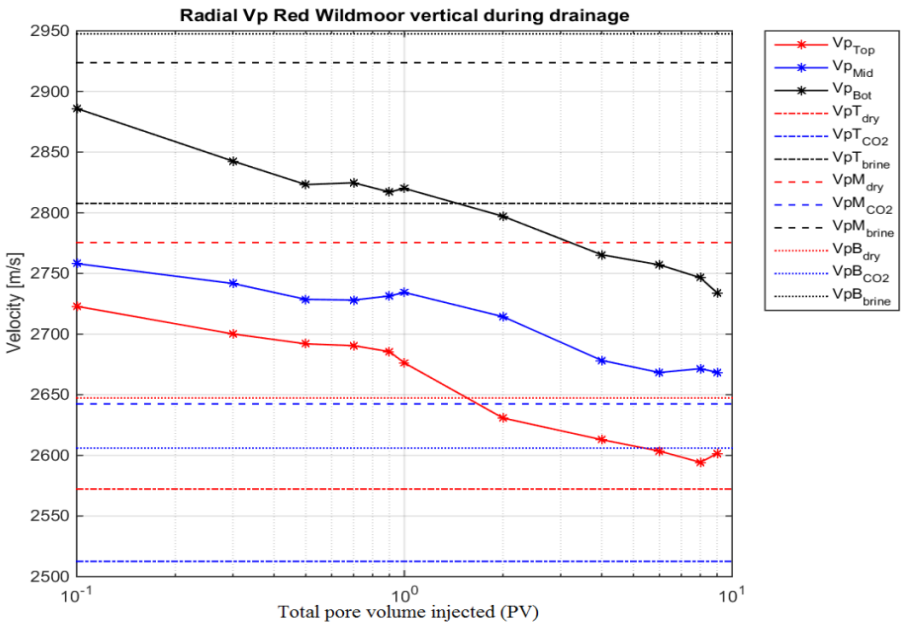

Figure 4.8 Radial P-wave velocities during drainage compared with saturated conditions for top, middle and bottom

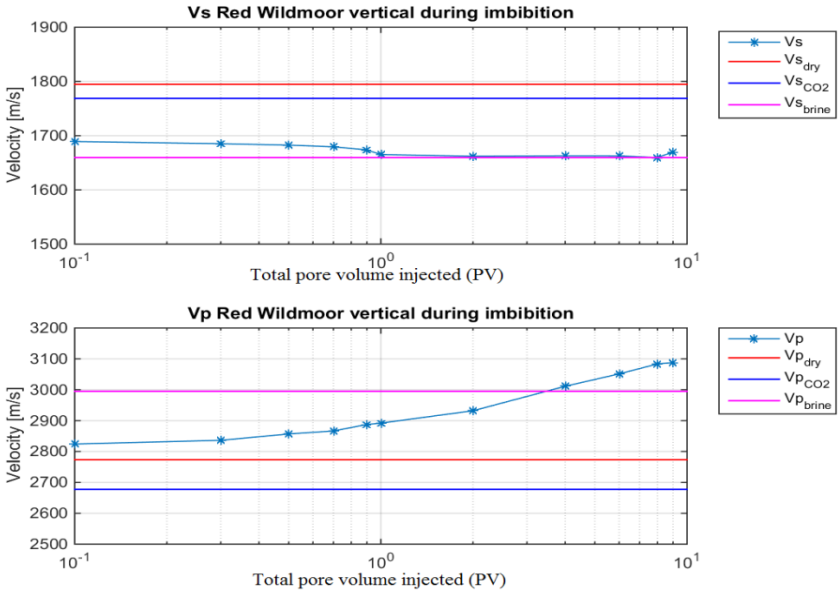

Figure 4.9 Measured axial P- and S-wave velocities during imbibition compared with saturated conditions.

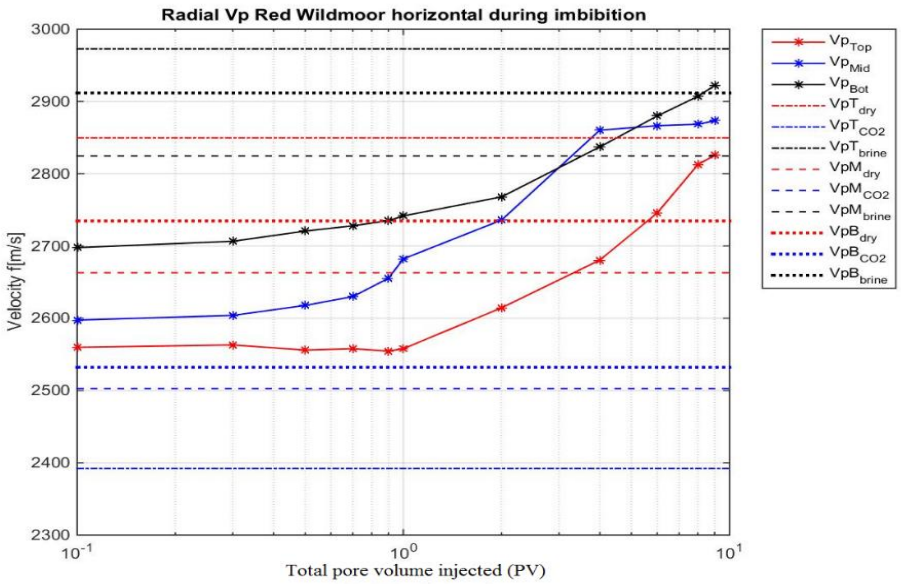

Figure 4.10 Radial P-wave velocities during imbibition compared with saturated conditions for top, middle and bottom.

All the three radial P-wave velocities, increases with increasing pore volume during imbibition. Bottom Vp increases first followed by middle then top (Fig 4.10). There is significant increase in Vp between 1-8 PV as a result of flow rate change. All the measured radial velocities during imbibition are slightly higher than measured at fully brine saturated conditions similar to axial measurements.

4.1.3 Berea vertical core plug

4.1.3.1 Saturated conditions

P- and S-wave velocities for dry, CO_2 and brine-saturated condition were made prior to flooding under the same temperature and pressure condition as vertical and horizontal Red Wildmoor samples. In general, Vs for dry is the highest while brine has the lowest for saturated conditions, as shown in Figure 4.11.

4.1.3.2 Drainage (CO_2 injection)

P- and S-wave velocities were made at a constant pore and differential pressures of 10 MPa and15 MPa respectively using liquid CO_2. Maintaining a constant differential pressure during injection is essential since wave behaviour of the sample displays strong pressure dependence. For Vs, there is no significant change in measurements ca 1% increase. At the end of drainage (11 PV), the sample attains 45% CO_2 saturation and the Vp decreases by -4% and it is 1% higher that values at fully CO_2 saturated (Fig. 4.12). All the radial velocities decrease with drainage. In comparison to values at fully brine-saturated values, the top, middle and bottom Vp decreases by -6%, -7% and -6% upon injecting 11 PV CO_2 (Fig. 4.13).

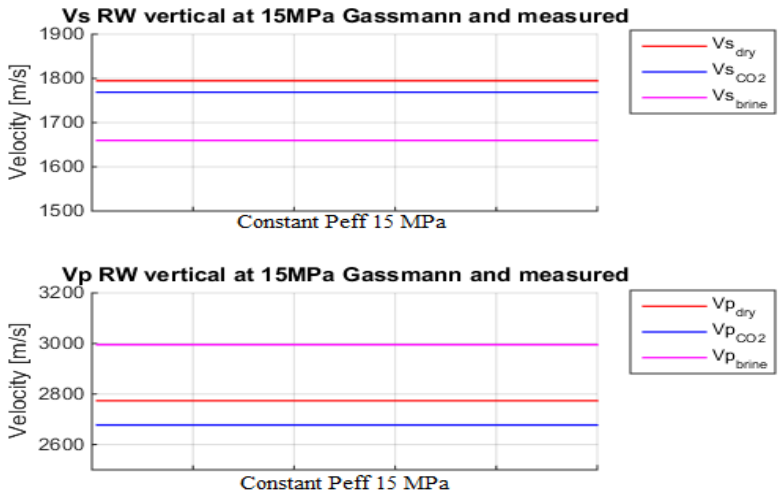

Figure 4.11 Axial P- and S-wave velocities for dry, CO_2 and brine-saturated conditions at 15 MPa.

Table 4.3 CO_2 [mL] injected into Berea sandstone vertical plug (1 PV = 16.87 mL).

Flow rate	0.5mL/min							2.5mL/min						
PV	0	0.1	0.3	0.5	0.7	0.9	1	2	4	6	8	9	10	11
Injected CO_2 [ml]	0	3.69	7.06	10.44	13.81	17.18	18.87	35.74	69.43	103.22	1436.96	153.83	170.70	187.57

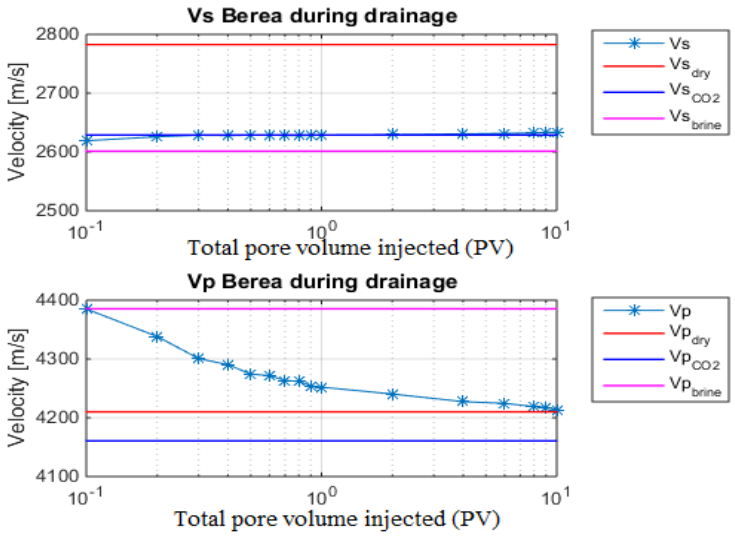

Figure 4.12 Axial P- and S-wave velocities for drainage compared with saturated conditions.

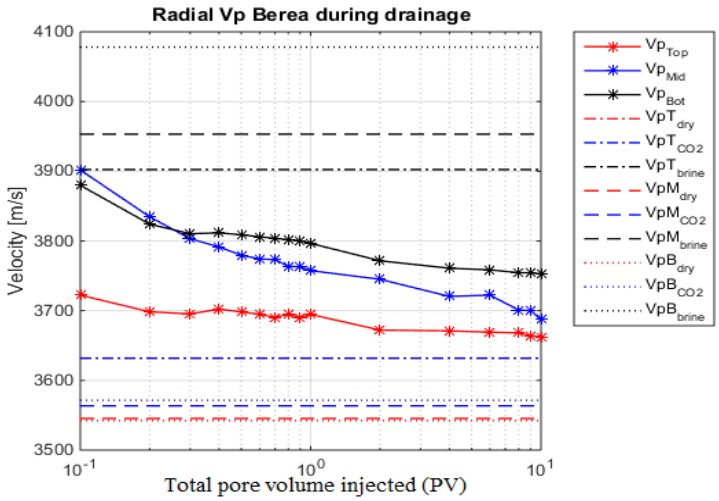

Figure 4.13 Radial P-wave velocities during drainage compared with saturated conditions for top, middle and bottom

4.1.3.3 Imbibition (brine injection)

Figure 4.14 shows Vp and Vs velocities measured during imbibition for vertical Berea sandstone core plug. From the results, measured Vs are higher than measured values at saturated conditions. When brine is substituted in the pore spaces, the Vs decreased by -1%, and is higher than all measured Vs velocities at fully saturated conditions. After injecting 11PV brine, the Vp increases by 4%.

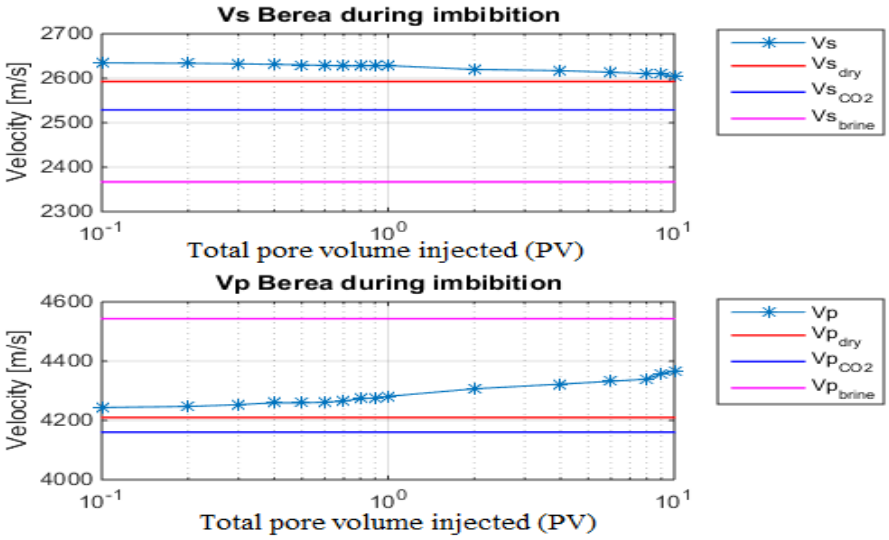

Figure 4.14 Measured axial P- and S-wave velocities during imbibition compared with saturated conditions.

For the radial velocities (Fig 4.15), there is a general increase in all the Vp velocities with increase in injection. The velocity increases significantly with increase in flow rate between

2-11 PV. At the end of imbibition, top, middle and bottom Vp increases by 6%, 6% and 5% respectively.

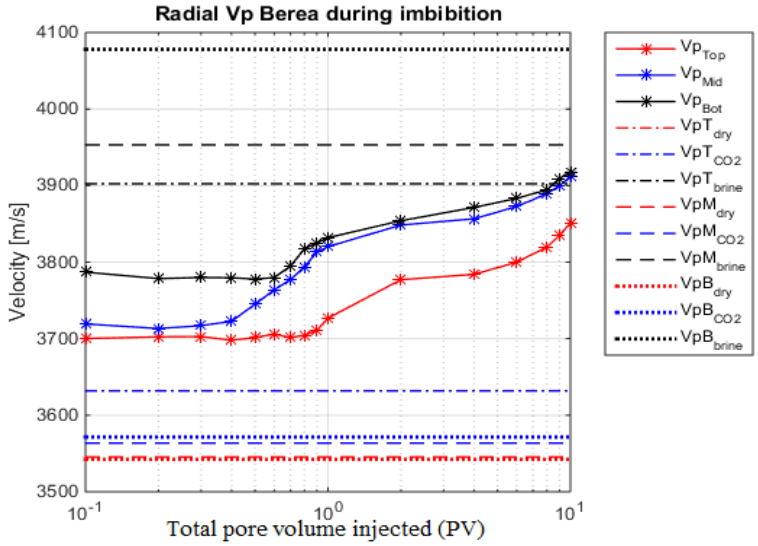

Figure 4.15 Radial P- and S-wave velocities during imbibition compared with saturated conditions for top, middle and bottom.

4.2 Discussion

4.2.1 Influence of anisotropy on velocity (vertical and horizontal RW core plugs)

There is significant influence of anisotropy on the measured velocities on the vertical and horizontal Red Wildmoor core plugs. Figure 4.16 shows the variation in velocities with injected pore volume. For both Vs and Vp, the Red Wildmoor horizontal core plug has a higher velocity that the vertical. In the vertical Red Wildmoor core plug, the layering are perpendicular to the wave propagation direction and the wave must pass through all layering hence, the measured velocity is representative of the change in saturation in each layer (Alemu et al., 2011a). For the horizontal plug, the orientation of the layers with high and low CO_2 saturation is parallel to the wave propagation direction hence the wave is not reflected at each layer interface as in the vertical sample, but rather guided through the high and low porosity channels. As a result, the measured velocity is not representative of the change in saturation.

According to Han et al. (1986), waves travel fastest when the direction of particle motion, is parallel to the direction of greatest stiffness. The Vp waves have particles motion in the direction parallel to layering and fractures, and travel more slowly when perpendicular to layering and fractures. Similar to Vp, Vs with vertically polarised particle motion, parallel to layering is faster than Vs with particle motion polarized orthogonal to fractures.

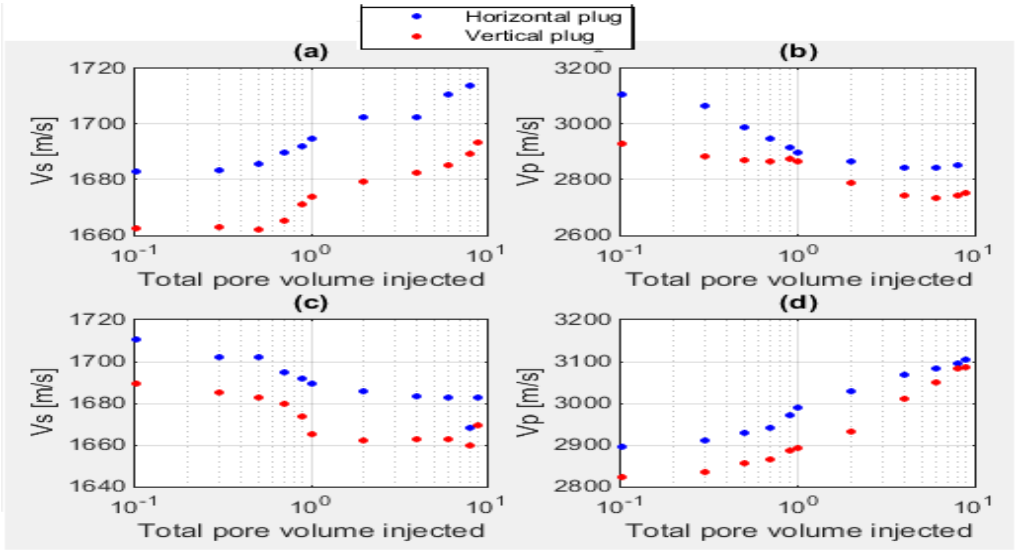

Figure 4.16 Vp and Vs variation with pore volume during CO_2 flooding. (a) and (b) shows velocities during drainage, (c) and (d) are for imbibition for the vertical and horizontal RW core plugs.

4.2.2 Influence of mineralogy on velocity (vertical RW and Berea core plugs)

It is apparent from Figure 4.17 that the mineral composition of the rock influences the Vp and Vs for both vertical Red Wildmoor and Berea core plugs. Mineralogy (especially clay content) affects rock velocities in two ways. The most obvious is through the bulk and shear moduli of the solid matrix of the rock which is primary input to all velocity model. From petrophysical results, *Kdry* for vertical Berea core plug is 19.60 GPa, while for Red Wildmoor *Kdry* is 6.45 GPa. Indirectly, mineralogy controls the degree of cementation and pore structure of the rock. Other factors than influences the velocity in clastic rocks include depositional environment, grain size, and shape, pore size and shape, sorting, and packing (Winkler and Murphy, 1995). Water saturation effect on elasticity of a rock is not only correlated to porosity but also clay content and consolidation.

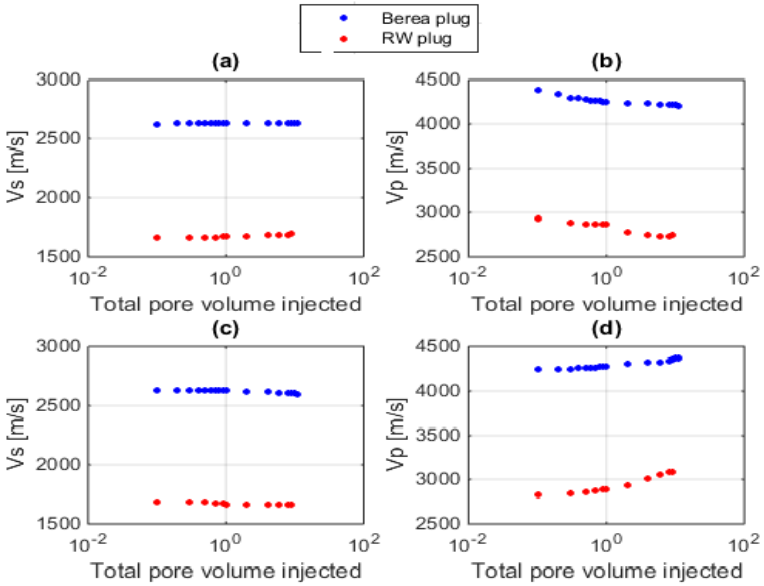

Figure 4.17 Effect of mineralology during drainage and imbition for Red Wildmoor and Berea vertical plugs. (a) and (b) shows drainage while (c) and d shows imbibition.

4.2.3 Comparison of experimental results with theoretical prediction

Variation in measured velocities due to change in CO_2 saturation in the sample were compared with the Gassmann-model. The Voigts-Reuss-Hills model from Wood (1941) was used to calculate the effective pore fluid modulus and average mineral bulk modulus. List of parameters used in Gassmann's equation is provided in Chapter 2. Both observed and modelled results shows that once brine replaces CO_2 in the pore spaces there is a decrease in Vs and an increase in Vp with increase in brine injection. The measured Vp are higher than Gassmann apart from Berea vertical plug core (Fig 4.18 and Fig 4.19). This inconsistency can be attributed to cementation resulting from clay minerals (13%) leading to violation of Gassmann's assumption. These results are in agreement with observations made by Winkler (1986); Winkler and Nur (1982) and Knight and Nolen-Hoeksema (1990) who observed that measured seismic velocities at ultrasonic frequencies are often higher than those predicted by Gassmann's given than high-frequency waves are used in laboratory whereas Gassmann's equation assumes zero wave frequency. For seismic waves, only unconsolidated sands can approximately meet this assumption because of the sand's high porosity and permeability (Wang, 2000).

According to Gassmann's equation μsat = μdry thus the main factor controlling Vs is effective density which is a function of in situ pore fluid. For fully saturated conditions, brine core plugs have the highest Vp while CO_2 saturated has the lowest. The effect of bulk modulus and density have inverse effect on Vp velocities.

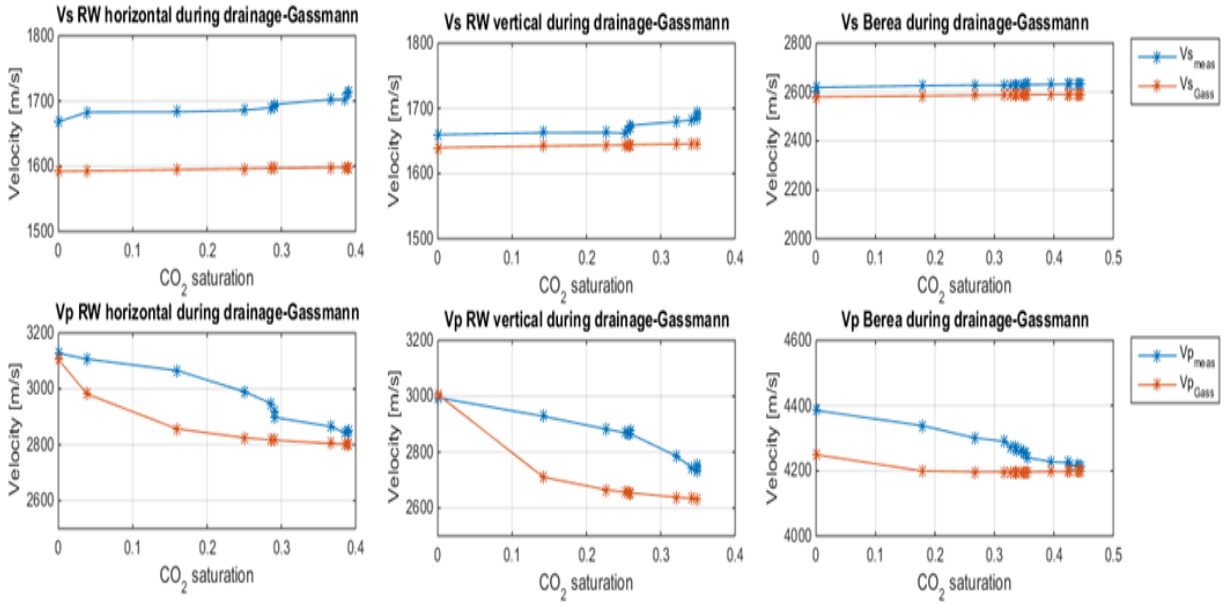

Figure 4.18 Vp and Vs variation against calculated CO_2 saturation for Red Wildmoor core plugs and vertical Berea sandstone plug during drainage.

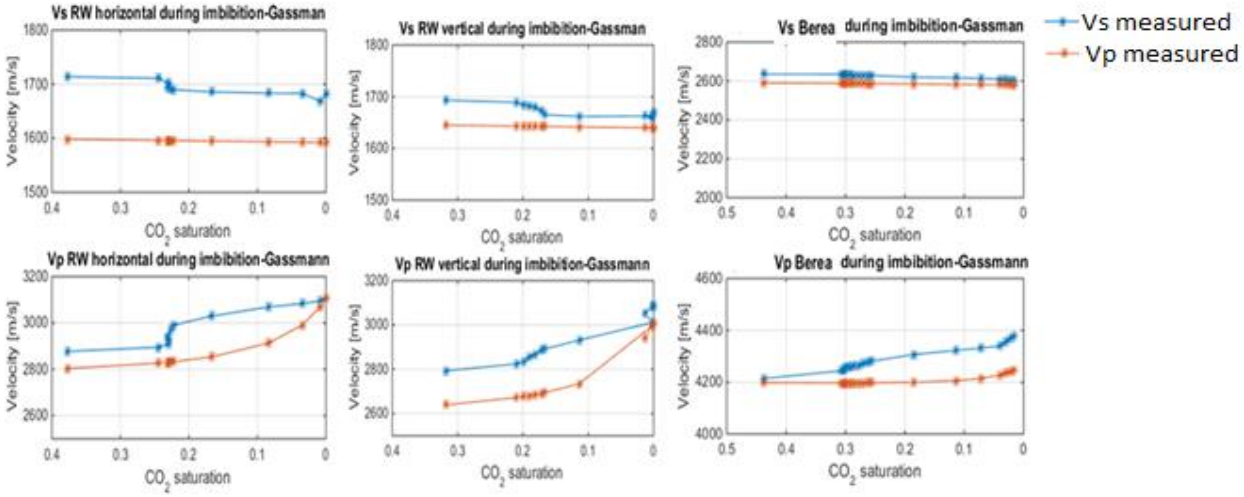

Figure 4.19 Vp and Vs variation against calculated CO_2 saturation for Red Wildmoor core plugs and vertical Berea sandstone plug during imbibition.

4.2.4 Vp-Vs relation between drainage and imbibition phases

From the experimental results, opposite tendencies of the Vp and Vs with changes in brine and CO_2 injection into the core plugs were observe (Fig 4.20). According to Mavko and Mukerji (1998) Vp-Vs relation are the key to determination of lithology and the confirmation of existence of fluid from seismic data. Hamada (2004) indicated that reservoir

fluid can be identified using relationship between Vp and Vs wave arrival time. Figure 4.20 illustrates the Vp-Vs relations for drainage and imbibition. During drainage, Vp decreases significantly, and the Vs increases slightly. At the end of imbibition, Vp does not recover fully to the pre-drainage level which is the effect of residually trapped CO_2. These are consistent with precious study (Kitamura et al., 2014). From Figure 4.20, change in CO_2 saturation and residual CO_2 trapping mechanism during drainage and imbibition can be monitored. One of the challenges with this method is the small velocity changes in deep reservoirs (Kitamura et al., 2014). Ghaderi and Landrø (2009) reported that Vp changes by around 0.2 km/s in CO_2 injection site. Therefore, it must be possible to monitor a change of at least 0.2 km/s.

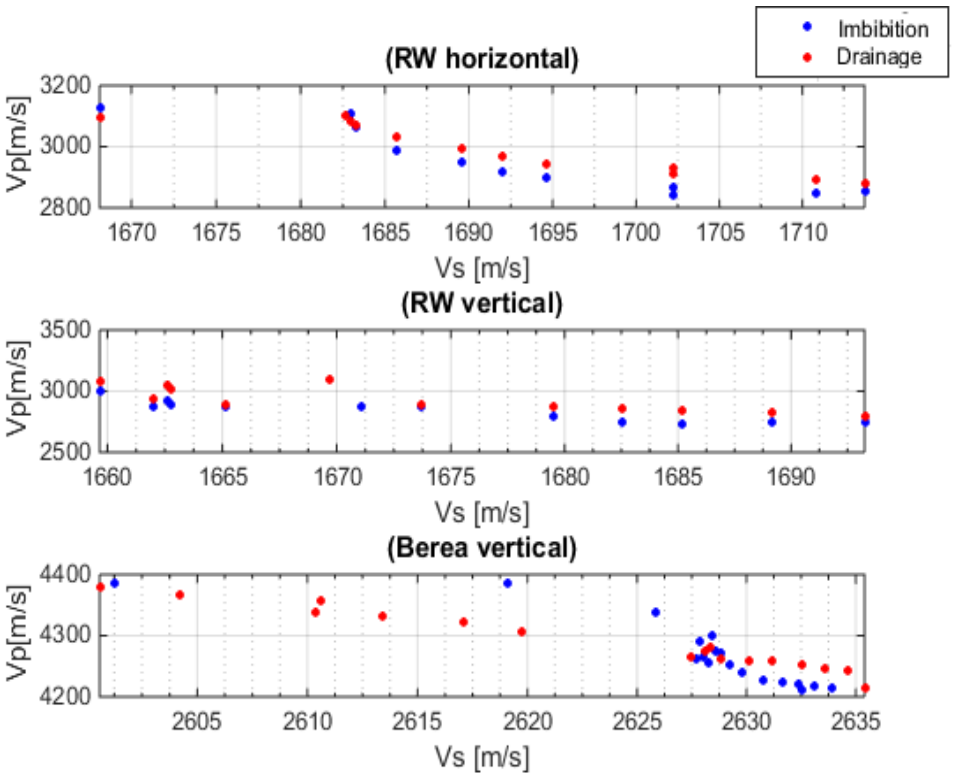

Figure 4.20 Vp-Vs relation during drainage and imbibition for the three core plugs.

Chapter 5: Electrical resistivity measurements

In this chapter, laboratory results, modelling results, and discussion on resistivity and saturation of the three studied sandstone core plugs are given. Calculated saturation and modelled velocities are based on Archie (1942) and Gassmann (1951a). Results used in this chapter were acquired from velocities and measured resistivities explained in Chapter 3. Due to laboratory setup, only middle radial resistivities were measured for both vertically and horizontally Red Wildmoor plugs while for Berea core plug, top, middle and bottom resistivities were acquired.

5.1 Results

5.1.1 Red Wildmoor horizontal core plug

Figure 5.1 shows variation of measured resistivity with pore volume for both axial and radial during drainage and imbibition. The results show that both axial and radial resistivities increase with injection of CO_2 into the sample. The average measured axial and radial resistivities at full brine saturation in the sample were 2.46 and 2.25Ω·m respectively. After injection of 8 PV CO_2, the measured resistivities increased to 6.63Ω·m (Sco_2 = 39%) and 6.62Ω·m (Sco_2 = 42%) for axial and radial respectively. Radial resistivities increases faster than axial during drainage especially between 0-1 PV then both resistivities remain constant after injecting 4 PV. During imbibition, brine is injected from the bottom into the sample to replace CO_2. The measured axial and radial resistivities at the end of imbibition (9 PV brine) were 2.50 and 2.31Ω·m respectively. Both axial and radial resistivities decreases significantly during imbibition with injection of 0.1 PV and tends to stabilize between 0.2-1 PV but drastically changes with increase in fluid flow. Calculated saturations for both axial and radial are almost the same at the end of drainage. During imbibition, both axial and radial resistivities remains constant with injection of 0.1 PV brine but increases significantly between 0.1-0.7 PV then stabilizes up to 1 PV the increases drastically with increase in flow rate.

5.1.2 Red Wildmoor vertical plug

Due to technical difficulties with the setup, measured resistivity values for horizontal Red Wildmoor were abnormally higher than expected hence the values were normalized. During drainage and imbibition, both axial and radial resistivities increases and decreases respectively with injection of 0.1 PV then remain stable up to 1 PV where they underwent significant changes with flow rate change. Measured axial and radial resistivities at full brine saturation in the sample were 1Ω·m for both cases. After injection of 9 PV CO_2, the measured resistivities increased to 2.34Ω·m (Sco_2 = 34.8%) and 2.56Ω·m (Sco_2 = 37.5%) for axial and radial respectively. The axial and radial resistivities do remains more or less constant between 0-1 PV then increases significantly with increase in pore volume from 2-4 PV. Maximum CO_2 saturation is attained after 6 PV while brine saturation is achieved after injection of 4PV as shown in Figure 5.2.

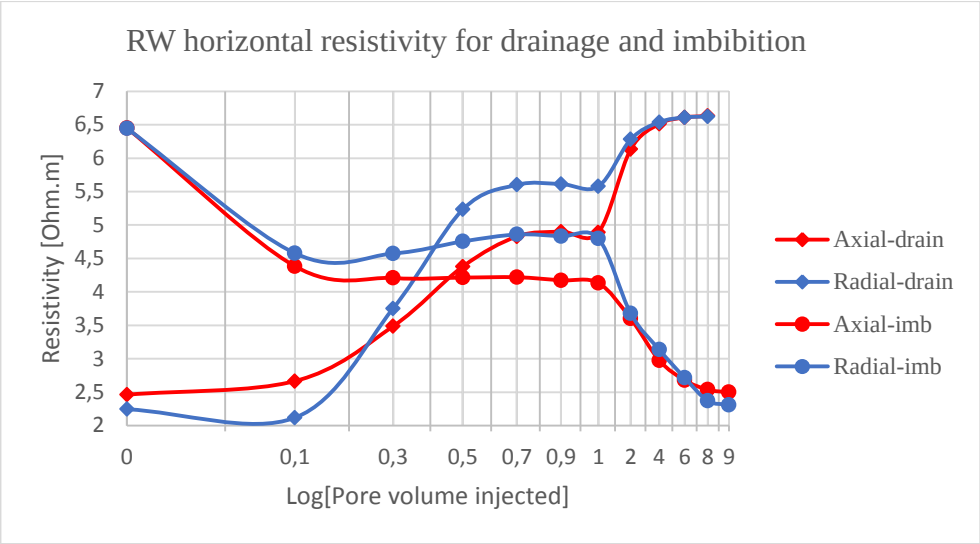

Figure 5.1 Axial and radial resistivity measurements for horizontal Red Wildmoor plug during drainage and imbibition. drain = drainage, imb = imbibition.

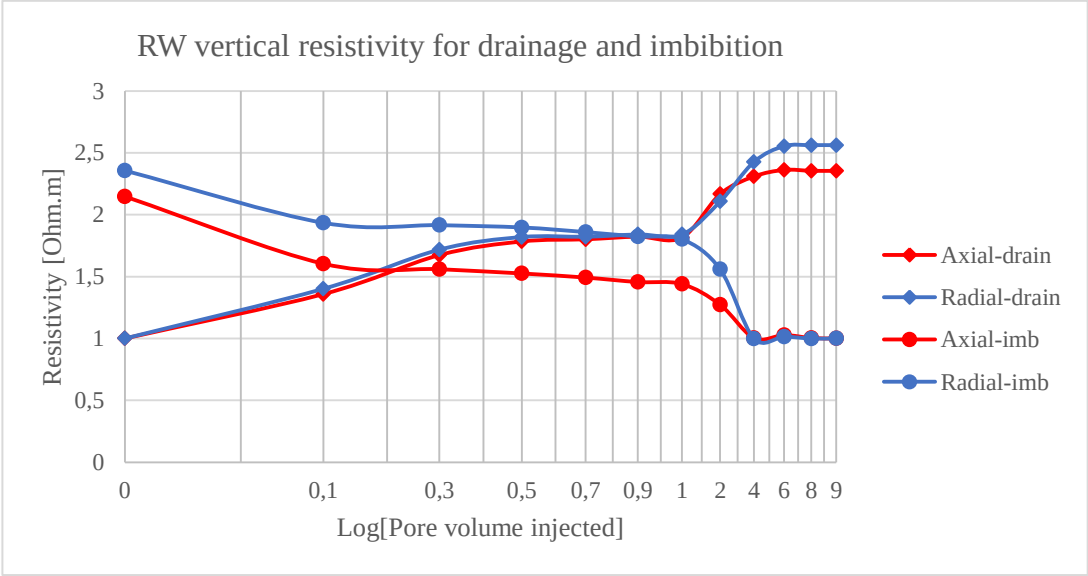

Figure 5.2 Axial and radial resistivity measurements for vertical Red Wildmoor during drainage and imbibition. drain = drainage, imb = imbibition.

5.1.3 Berea vertical core plug

For the Berea sandstone core plug, one axial and three radial resistivities were measured. There is significant increase in resistivity for all channels between 0-1 PV. Change in injection rate does not have any significant effect on resistivity. The average measured axial and radial resistivity at full brine saturation in the sample were 8.29 for the axial and 9.22, 9.57, and 8.13 Ω·m for radial top, middle and bottom. After injection of 11 PV CO_2, the measured resistivity increased to 26.97Ω·m (Sco_2 = 45%) for axial and 37.17Ω·m (Sco_2 = 50%), 35.96Ω·m (Sco_2 = 48%), and 35.62Ω·m (Sco_2 = 52%) for top, middle and bottom radial respectively. Axial resistivity has the lowest resistivity. At the end of imbibition, the measured axial and radial resistivities are 8.57Ω·m for axial and 9.53Ω·m, 9.71Ω·m, and 8.44Ω·m for top, middle and bottom radial respectively and attains 98% brine saturation.

The resistivities decreases significantly upon injection of 0.1 PV of brine with axial dropping first followed by bottom, middle then top. Brine is injected from the bottom of the sample to avoid gravity segregation. There is no remarkable change in resistivity measurements with change in flow rate. From Figure 5.3 the saturation increases significantly at the top after injecting 0.2 PV.

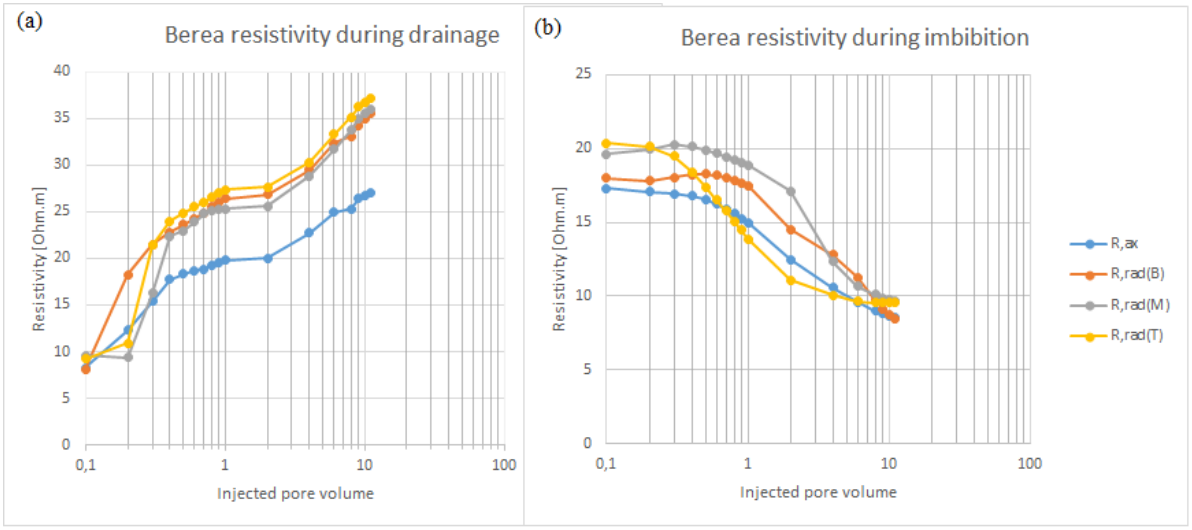

Figure 5.3 Axial and radial resistivity measurements for vertical Berea core plug during (a) drainage and (b) imbibition. R,ax = axial resistivity, rad(B), rad(M), and rad(T) are the radial bottom, middle and top resistivity measurement respectively. X-axis is plotted in log hence the omission of 0 PV. Refer to Table B.4 in the appendix.

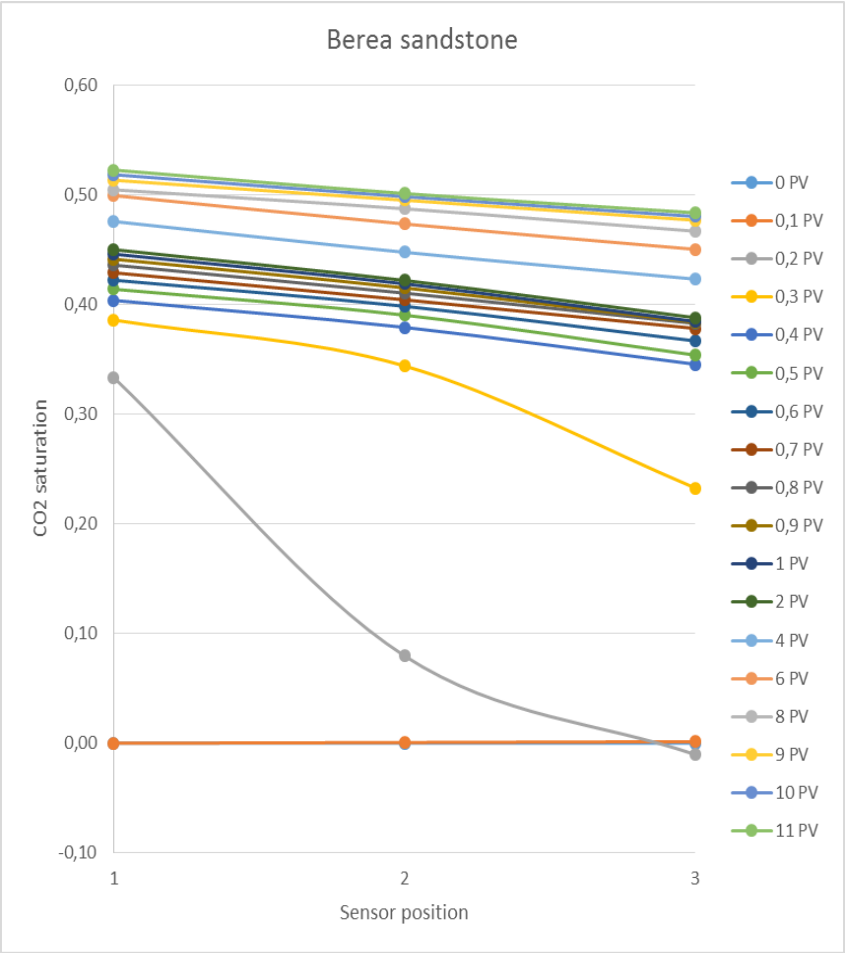

Figure 5.4 Slice-average CO_2 saturation along the length of Berea sample. The caption in the legend represents the cumulative injected fluid during drainage. 1, 2 and 3 on the x-axis represents top, middle and bottom sensors respectively.

5.2 Discussion

5.2.1 Relationship between CO_2 saturation (sCO_2) and Vp

Figure 5.5 illustrates relationship between Vp and sCO_2 during drainage and imbibition in the three core plugs. During drainage, measured velocities rapidly decreases with increasing CO_2 injection up to particular CO_2 saturation point above which the Vp decreases more slowly with injection. These points are 1 PV for horizontal Red Wildmoor plug (29% sCO2), 4 PV (34% sCO2) for vertical Red Wildmoor plug and 1 PV for Berea vertical plug (35% sCO2). The sCO_2 value reaches 40%, 34% and 45% respectively for horizontal Red Wildmoor, vertical Red Wildmoor and Berea core plugs respectively at the end of drainage process. These sCO_2 values are the starting point of the imbibition. During imbibition, the Vp recovers steadily and gently for both vertical Red Wildmoor and Berea core plugs with increasing brine injection. P-wave velocities at the end of imbibition are lower that at 100% brine saturated and these experimental results shows that sCO_2 does not recover fully an indication of residual CO_2 trapping (Fig 5.5).

Hysteresis is observed in the Vp- sCO_2 during drainage and imbibition. This hysteresis implies difference in the CO_2-water distribution pattern in the pore space (Mavko and

Mukerji, 1998). Knight and Nolen-Hoeksema (1990) studied the relationship between Vp and *Sw* under atmospheric pressure conditions and reported similar hysteresis effect. This phenomenon was also reported in water-wet rocks by (Cadoret et al., 1995; Kitamura et al., 2014; Toms et al., 2006). Alemu et al. (2011b) observed that there were no hysteresis in the relationship between Vp and sCO_2 under liquid CO_2 conditions while studying Rothbach sandstone. Later (Alemu et al., 2013) observed this phenomenon on a vertically drilled Rothbach sandstone and not horizontal plug. Such hysteresis is a considerable issue for confirmation of CO_2 storage in reservoir. Xue et al. (2009) conducted both laboratory and field studies and the results indicated that P-wave velocity becomes less sensitive when CO_2 saturation is above 20%, while resistivity kept increasing with increase in sCO_2. These results suggest that the use of resistivity is useful way to overcome the limitation of the seismic method in CO_2 monitoring. They also show that resistivity is sensitive to detect dissolution of CO_2 in formation water hence the usefulness of electrical and electromagnetic techniques in geological CO_2 monitoring. Suman and Knight (1997) and Zhou and Stenby (1997) recommended that Archie's law is not always valid since the resistivity index is affected by other parameters like fluid distribution pattern, saturation history, wettability, clay content pore structure and salinity of brine which should be taken into consideration when calculating saturation.

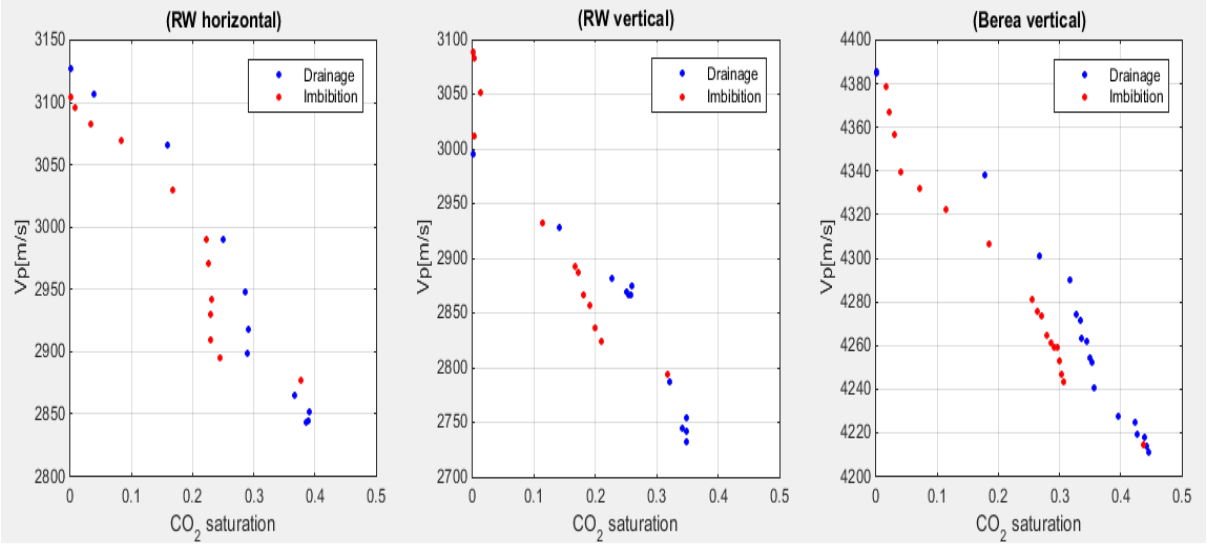

Figure 5.5 Vp variation with CO_2 saturation during drainage and imbibition for the three core plugs studied.

5.2.2 Influence of anisotropy on CO_2 saturation (vertical and horizontal RW plugs)

After injecting 4PV brine in both the horizontal and vertical Red Wildmoor core plugs, the resistivity remains constant throughout the test. This is indication of brine breakthrough. For the Red Wildmoor horizontal plug, 39% CO_2 saturation was achieved compared to 35% for vertical plug. Figure 5.6 shows CO_2 and resistivity variation with pore volume. The resistivity increases significantly for the horizontal plug compared to the vertical. The bedding planes appear to have affected the patterns of fluid distribution in both samples. Alemu et al. (2013) observed that there is correlation between porosity and CO_2 saturation where high porosity regions had higher saturation of CO_2 at all injection steps. Higher

velocities measured for the vertical plug especially at the bottom at the end of imbibition can be because of presence of micro fractures or small contrast in porosity in the sample, which facilitates flow and accumulation of injected brine at the bottom of the sample.

For the vertical Red Wildmoor plug, the layering are perpendicular to the wave propagation direction and the wave must pass through all layering hence, the measured velocity is representative of the change in saturation in each layer. For the horizontal plug, the orientation of the layers with high and low CO_2 saturation was parallel to the wave propagation direction hence the wave is not reflected at each layer interface as in the vertical sample, but rather guided through the high and low porosity channels. As a result, the measured velocity is not representative of the change in saturation. Since the layering are parallel to the wave propagation direction, and the brine-saturated layers acts as fast wave propagation paths, as a result, the measured velocity is not representative of the change in saturation. According to Alemu et al. (2013), amplified impedance contrast between the layers might affect the measured velocity and attenuation in a different manner than changes caused by fluid substitution in the rock with uniform porosity distribution.

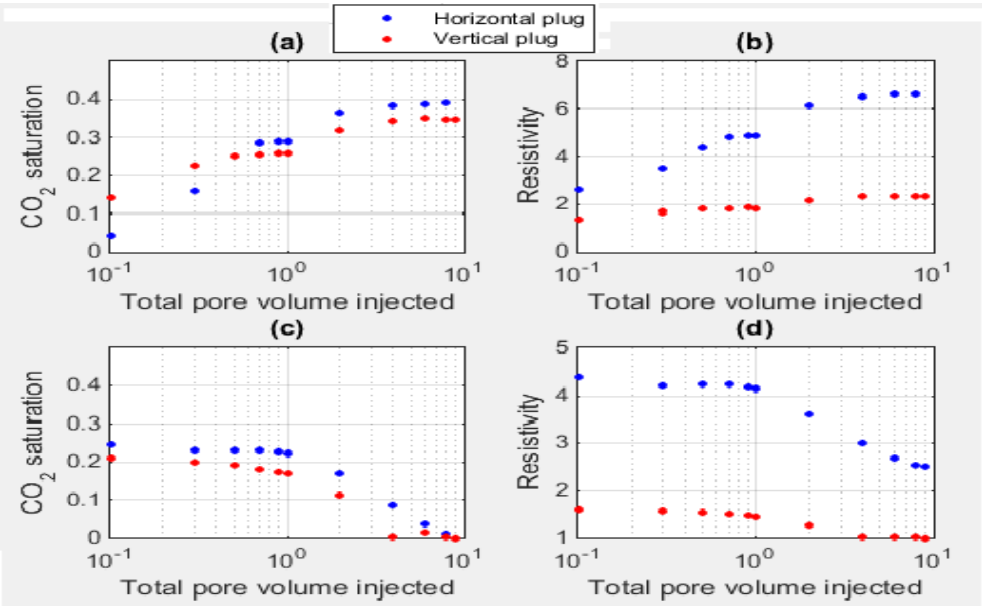

Figure 5.6 CO_2 saturation and resistivity to determine the influence of anisotropy during drainage (a and b) and imbibition (c and d). The resistivity represented here is the average core resistivity measured along the length of the core plugs by two electrodes at the top and bottom of the core.

5.2.3 Influence of mineralogy on saturation (Berea and RW vertical plugs)

Figure 5.7 shows the variation in CO_2 saturation and resistivity for both vertical core plugs: Red Wildmoor and Berea with varying mineral composition. For the vertical Red Wildmoor plug, 35% CO_2 saturation and a resistivity of 2.3 Ω·m is attained after injecting 9 PV while for the vertical Berea plug, after injecting the same amount of pore volume 44% CO_2 saturation and a resistivity of 26.38 Ω·m was achieved. From the SEM and XRD analysis, vertical Berea sandstone plug contains more clay that vertical Red Wildmoor plug. Presence of shale in sandstone influences the electrical conductivity of the formation water due to the

presence of clay minerals like kaolinite and illite, which also contribute to the electrical conduction. Because of this, more complicated electrical models and equations should be used to estimate water saturation for shaly sandstone reservoir (Winkler and Murphy, 1995).

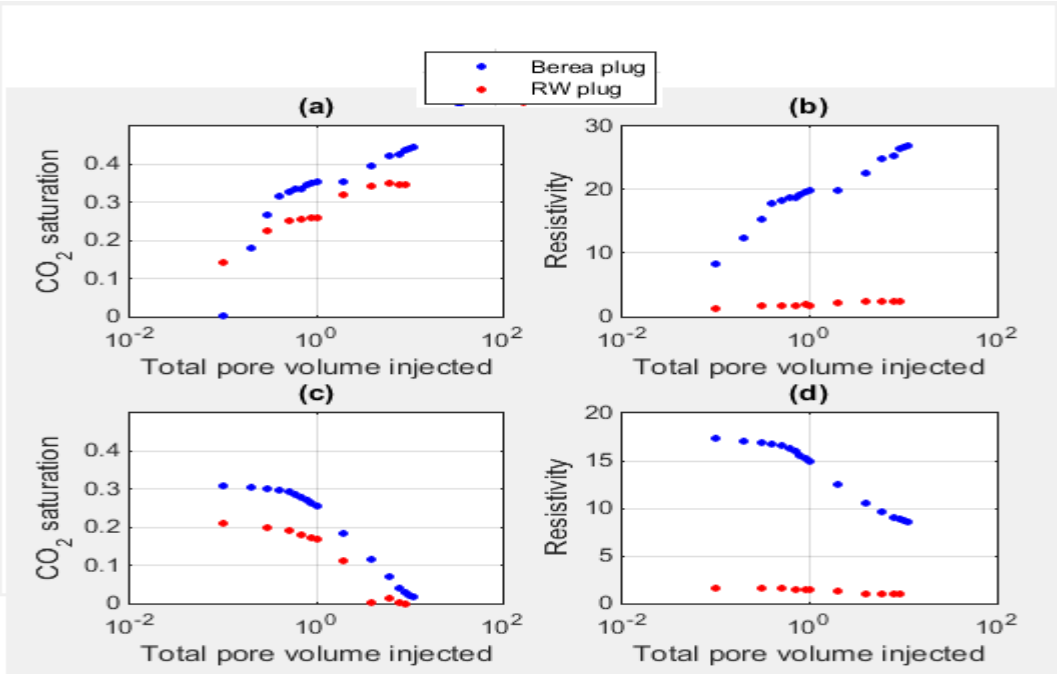

Figure 5.7 CO_2 saturation and resistivity to determine the influence of mineralogy during drainage (a and b) and imbibition (c and d). The resistivity represented here is the avaerage core resistivity measured along the length of the core plugs by two electrodes at the top and bottom of the core.

5.2.4 Influence of flow rate on saturation

Clear dependency is observed between flowrate and average CO_2 saturation (Fig. 5.8), the latter being related to the brine displacement efficiency. Several observations can be made with respect to low and high flow regime/viscous dominated regime. As the injection flow rate increases, the variation of saturation within the core decreases; in other words, a greater flow rate is needed to reach a relative constant saturation for the heterogeneous core as compared to homogeneous core. In high flow rate regimes (Fig 5.8b), viscous forces dominate the system, while the effect of gravity becomes more important as the injection rate is lowered (Fig 5.8a). The effect of gravity is only important when the flow rate is lower that the viscous dominated regime. In terms of sub-core heterogeneity, radial velocities during imbibition show that the brine has higher sweep efficiency for the vertical Red Wildmoor plug than the horizontal Red Wildmoor plug.

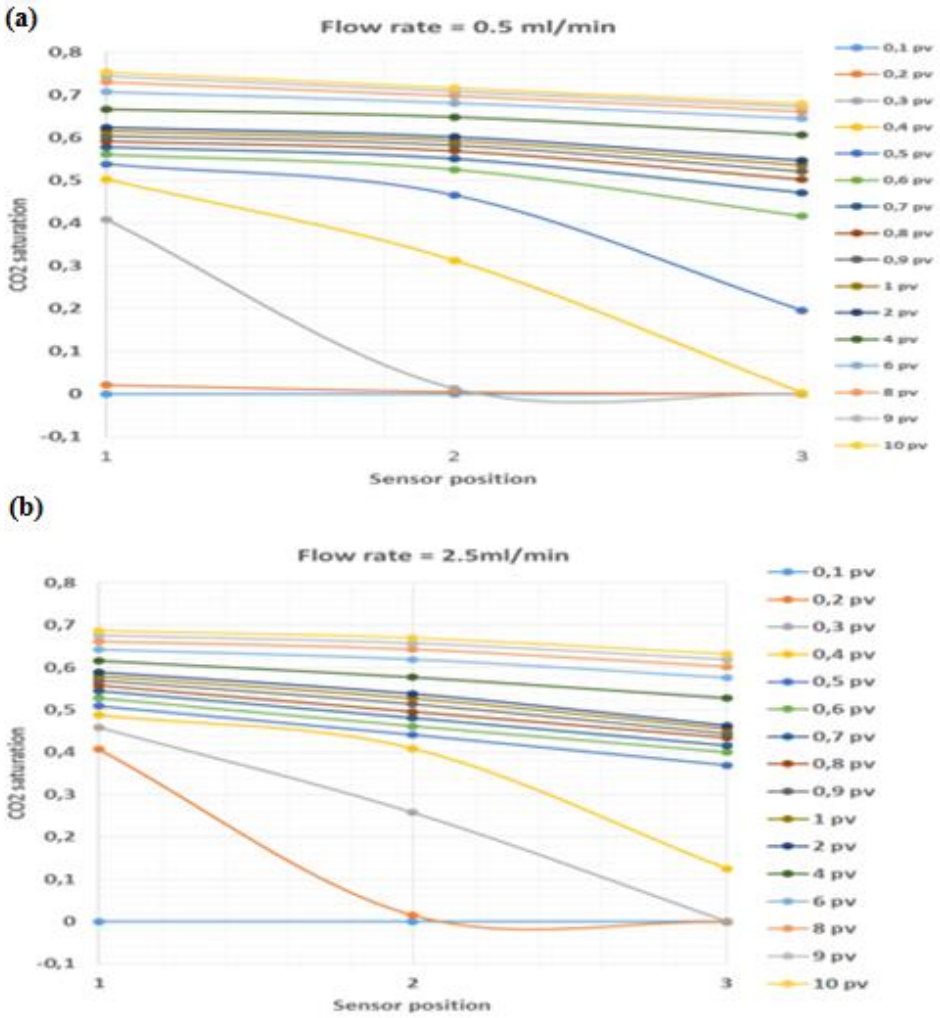

Figure 5.8 Saturation profile along the core of Rothbach sandstone. (a) is for 0.5ml/min flow rate while (b) is for 2.5ml/min. The caption in the legend represents the cumulative injected fluid during drainage. It is evident that with low flow rate higher saturation is achieved as compared to higher flow rate. On the other hand, CO_2 breakthrough is reached faster for the higher flow rate but CO_2 saturation reaches a steady state after certain pore volume of CO_2 was injected into the samples. In general, heterogeneity, gravity and capillary forces influence the flow rate. Data courtesy of NGI.

Chapter 6: Summary and Conclusions

This study aims to study the effect of sub-core heterogeneities on the fluid distribution pattern and acoustic velocity and electrical resistivity response during CO2 flooding in order to understanding estimation of saturation of stored carbon dioxide in a sandstone reservoir. Three-sandstone core plugs (vertical and horizontal Red Wildmoor and vertical Berea) were utilized. 30g/l NaCl and liquid CO_2 were used as pore fluids. The core plugs were analysed using SEM and XRD analysis to determine their mineralogy and petrophysical properties. These results reveals high clay content in vertical Berea sandstone core plug that the vertical and horizontal Red Wildmoor. The core plugs then underwent dry, fully CO_2 and brine saturated loading and unloading tests prior to CO_2 flooding. The effective pressure varied from 1 to 15 MPa with a constant pore pressure of 10 MPa. For the CO_2 flooding, an effective pressure of 15 MPa and pore pressure of 10 MPa was maintained. During drainage and imbibition, CO_2 and brine were injected stepwise until measured resistivities were similar to saturated condition resistivities.

By introducing CO_2 into the sample, the Vp velocity decreases drastically while the Vs changes slightly. As expected, the Vs increased during drainage and decreased with imbibition while Vp decreased with drainage and increase during imbibition. During drainage, the Vs increased by 2%, 3% and 1% for vertical Red Wildmoor, horizontal Red Wildmoor and vertical Berea core plugs respectively while the Vp decreased by 8%, 9% and 4%. For the imbibition, Vs did not change for the vertical Red Wildmoor but decreased by 2% and 1% for the horizontal Red Wildmoor and vertical Berea core plugs respectively. The Vp increased by 11%, 8% and 4% for vertical Red Wildmoor, horizontal Red Wildmoor and vertical Berea respectively.

The acoustic velocity results shows than anisotropy and mineralogy can influence reservoir response during CO_2 flooding. Comparison between vertical and horizontal Red Wildmoor core plugs shows that waves travel fastest when the direction of particle motion, is parallel to the direction of greatest stiffness (Han et al., 1986). The Vp waves have particle motion in the direction parallel to layering and fractures, and travel more slowly when perpendicular to layering and fractures. In term of CO_2 saturation measurements, horizontal plug attained higher saturation compared to vertical for the Red Wildmoor plugs. The layering are perpendicular to the wave propagation direction Red Wildmoor vertical plug hence, the wave must pass through all layering hence, the measured velocity is representative of the change in saturation in each layer. For the for the horizontal plug, the orientation of the layers with high and low CO_2 saturation was parallel to the wave propagation direction hence the wave is not reflected at each layer interface as in the vertical sample, but rather guided through the high and low porosity channels.

A clear relationship between flow rate and average CO_2 saturation is observed, the latter being related to the brine displacement efficiency. Several observations were made with respect to low and high flow regime/viscous dominated regime. As the injection flow rate increases, the variation of saturation within the core decreases, this means that a greater flow rate is needed to reach a relative constant saturation for the heterogeneous core as compared to homogeneous core. It is evident that with slow flow rate, higher saturation is achieved compared to faster flow rate, and CO_2 breakthrough is achieved faster for the higher flow rate. This assumption should be treated with caution given that a higher flow rate was

applied before a lower one hence the possibility of widening of pore throats before injection at a lower flowrate. In general, heterogeneity, gravity and capillary forces influence the flow rate.

Hysteresis is observed in Vp during drainage and imbibition for all the core plugs. This hysteresis implies difference in the CO_2-water distribution pattern in the pore space (Cadoret et al., 1995; Knight and Nolen-Hoeksema, 1990; Mavko and Mukerji, 1998). Such hysteresis is a considerable issue for confirmation of CO_2 storage. Therefore, integration of resistivity/EM data to seismic is a useful way to overcome the limitation of the seismic method in CO_2 monitoring. Electrical resistivity is sensitive to detect dissolution of CO_2 in formation water and so with seismic resistivity/EM is a very useful tool to monitor geological storage of CO_2.

Mineralogy (especially clay content) affects rock velocities in two ways. The most obvious is through the bulk and shear moduli of the solid matrix of the rock which is primary input to all velocity model. Vertical Berea plug has a higher velocity and saturation than vertical Red Wildmoor and this can be explained by its higher Kdry value compared to Red Wildmoor sample. In term of saturation, presence of shale in sandstone influences the electrical conductivity of the formation water due to the presence of clay minerals like kaolinite and illite, which also contribute to the electrical conduction.

Based on our laboratory results, the following conclusions can be drawn from this study:

- In CO_2 injection process, resistivity increases monotonously throughout the CO_2 injection period, the P-wave velocity decreased after starting drainage and increased with imbibition.
- Sample anisotropy has an effect on its acoustic velocity and saturation level.
- Mineral composition of the core plugs had effect on their saturation.
- Vp-Vs relation can be used to monitor residual CO_2 trapping.
- Monitoring of CO_2 migration depends strongly on resistivity increase and velocity reduction caused by injecting CO_2. This result suggests that resistivity and seismic velocity are useful to monitor the CO_2 migration behaviour in the CO_2 injection site.
- P-wave velocity and resistivity can be used to estimate CO_2 saturation in the field by applying Gassmann fluid substitution and resistivity. P-wave velocity becomes less sensitive at some particular value with increase in CO_2 saturation in a sample thus resistivity can complement effectively the difficulty of P-wave velocity on quantifying CO_2 saturation from Archie's law.
- A combination of axial and radial acoustic velocity and resistivity can be used to track CO_2 front movement.
- The experimental results showed the effect of changes in pore fluid saturation on seismic velocity of porous rocks.
- Gassmann's theory can be used to model changes in the P-wave velocity of sandstone containing different mixtures of liquids CO_2 and brine provided the distribution of the two fluids in pore spaces are counted for in the calculation of pore fluid bulk modulus.

Chapter 7: References

Alemu, B. L., Aagaard, P., Munz, I. A., and Skurtveit, E., 2011a, Caprock interaction with CO2: A laboratory study of reactivity of shale with supercritical CO2 and brine: Applied Geochemistry, v. 26, no. 12, p. 1975-1989.

Alemu, B. L., Aker, E., Soldal, M., Johnsen, O., and Aagaard, P., 2011b, Influence of CO2 on rock physics properties in typical reservoir rock: A CO2 flooding experiment of brine saturated sandstone in a CT-scanner: 10th International Conference on Greenhouse Gas Control Technologies, v. 4, p. 4379-4386.

-, 2013, Effect of sub-core scale heterogeneities on acoustic and electrical properties of a reservoir rock: a CO2 flooding experiment of brine saturated sandstone in a computed tomography scanner: Geophysical Prospecting, v. 61, no. 1, p. 235-250.

Alkan, H., Cinar, Y., and Ülker, E., 2010, Impact of capillary pressure, salinity and in situ conditions on CO2 injection into saline aquifers: Transport in porous media, v. 84, no. 3, p. 799-819.

Angus, S., Armstrong, B., and De Reuck, K., 2013, International Thermodynamic Tables of the Fluid State: Propylene (propene), Elsevier.

Archie, G. E., 1942, The Electrical Resistivity Log as an Aid in Determining Some Reservoir Characteristics: Society of Petroleum Engineers.

Armstrong, P., Ireson, D., Chmela, B., Dodds, K., Esmersoy, C., Miller, D., Hornby, B., Sayers, C., Schoenberg, M., and Leaney, S., 1994, The promise of elastic anisotropy: Oilfield Review, v. 6, no. 4, p. 36-47.

Arnold, O., Kerry, K., and Steven, C., 2009, The feasibility of reservoir monitoring using time-lapse marine CSEM: GEOPHYSICS, v. 74, no. 2, p. F21-F29.

Arts, R., Eiken, O., Chadwick, A., Zweigel, P., van der Meer, L., and Zinszner, B., 2004, Monitoring of CO2 injected at Sleipner using time-lapse seismic data: Energy, v. 29, no. 9-10, p. 1383-1392.

Azari, M., and Leimkuhler, J., 1990a, Completion Fluid Invasion Simulation and Permeability Restoration by Sodium- and Potassium-Based Brines, Society of Petroleum Engineers.

Azari, M., and Leimkuhler, J., Completion Fluid Invasion Simulation and Permeability Restoration by Sodium-and Potassium-Based Brines, *in* Proceedings SPE Formation Damage Control Symposium1990b, Society of Petroleum Engineers.

Bachu, S., and Adams, J. J., 2003, Sequestration of CO2 in geological media in response to climate change: capacity of deep saline aquifers to sequester CO2 in solution: Energy Conversion and Management, v. 44, no. 20, p. 3151-3175.

Bachu, S., Bradshaw, J., Bonijoly, D., Burruss, R., Holloway, S., Christensen, N. P., and Mathiassen, O. M., 2007, CO2 storage capacity estimation: Issues and development of standards: International Journal of Greenhouse Gas Control, v. 1, no. 1, p. 62-68.

Bachu, S., Gunter, W. D., and Perkins, E. H., 1994, AQUIFER DISPOSAL OF CO2 - HYDRODYNAMIC AND MINERAL TRAPPING: Energy Conversion and Management, v. 35, no. 4, p. 269-279.

Bassiouni, Z., 1994, Theory, measurement, and interpretation of well logs, Richardson, TX, Henry L. Doherty Memorial Fund of AIME, SPE textbook series.

Baudracco, J., and Aoubouazza, M., 1995, Permeability variations in Berea and Vosges sandstone submitted to cyclic temperature percolation of saline fluids: Geothermics, v. 24, no. 5–6, p. 661-677.

Benton, M. J., Cook, E., and Turner, P., 2002, *Permian and Triassic Red Beds and the Penarth Group of Great Britain*, Geological Conservation Review Series, No. 24, Joint Nature Conservation Committee, Peterborough, 337 pp., Geol. Mag., Volume 139, p. 595-598.

Berryman, J. G., and Blair, S. C., 1987, Kozeny-Carman relations and image processing methods for estimating Darcy's constant: Journal of Applied Physics, v. 62, no. 6, p. 2221-2228.

Biot, M. A., 1956, Theory of Propagation of Elastic Waves in a Fluid-Saturated Porous Solid. I. Low-Frequency Range: The Journal of the Acoustical Society of America, v. 28, no. 2, p. 168-178.

Bjørnevoll, N. H., Gabrielsen, R. H., Lothe, A. E., and Larsen, B. T., 2002, An experimental study of the texture of deformation bands: effects on the porosity and permeability of sandstones: Petroleum Geoscience, v. 8, no. 3, p. 195-207.

Burnside, N., and Naylor, M., 2014, Review and implications of relative permeability of CO 2/brine systems and residual trapping of CO 2: International Journal of Greenhouse Gas Control, v. 23, p. 1-11.

Cadoret, T., Marion, D., and Zinszner, B., 1995, Influence of frequency and fluid distribution on elastic wave velocities in partially saturated limestones: Journal of Geophysical Research: Solid Earth, v. 100, no. B6, p. 9789-9803.

Castagna, J. P., and Backus, M. M., 1993, Offset-dependent reflectivity: theory and practice of AVO analysis, Tulsa, Okla., Society of Exploration Geophysicists., VIII, 348 s. : ill. p.:

Castagna, J. P., Batzle, M. L., and Eastwood, R. L., 1985, Relationships between compressional-wave and shear-wave velocities in clastic silicate rocks: Geophysics, v. 50, no. 4, p. 571-581.

Chadwick, R. A., Zweigel, P., Gregersen, U., Kirby, G. A., Holloway, S., and Johannessen, P. N., 2004, Geological reservoir characterization of a CO2 storage site: The Utsira Sand, Sleipner, Northern North Sea: Energy, v. 29, no. 9-10, p. 1371-1381.

Constable, S., and Weiss, C. J., 2006, Mapping thin resistors and hydrocarbons with marine EM methods: Insights from 1D modeling: Geophysics, v. 71, no. 2, p. G43-G51.

Czernichowski-Lauriol, I., Rochelle, C., Gaus, I., Azaroual, M., Pearce, J., and Durst, P., 2006, Geochemical interactions between CO2, pore-waters and reservoir rocks - Lessons learned from laboratory experiments, field studies and computer simulations, *in* Lombardi, S., Altunina, L. K., and Beaubien, S. E., eds., Advances in the Geological Storage of Carbon Dioxide: International Approaches to Reduce Anthropogenic Greenhouse Gas Emissions, Volume 65, p. 157-174.

Daley, T. M., Myer, L. R., Peterson, J., Majer, E., and Hoversten, G., 2008, Time-lapse crosswell seismic and VSP monitoring of injected CO2 in a brine aquifer: Environmental Geology, v. 54, no. 8, p. 1657-1665.

Davis, T. L., M. J. Terrell, R. D. Benson, R. Cardona, R. R. Kendall, and R. Winarsky, 2003, Multicomponent seismic characterization and monitoring of CO2 flood at Weyburn Field, Saskatchewan: The Leading Edge, v. 22, no. 7, p. 696-697.

Dawson, G. K. W., Pearce, J. K., Biddle, D., and Golding, S. D., Experimental mineral dissolution in Berea Sandstone reacted with CO2 or SO2 –CO2 in NaCl brine under CO2 sequestration conditions: Chemical Geology, no. 0.

-, 2014, Experimental mineral dissolution in Berea Sandstone reacted with CO2 or SO2–CO2 in NaCl brine under CO2 sequestration conditions: Chemical Geology, no. 0.

Duan, Z., and Sun, R., 2003, An improved model calculating CO 2 solubility in pure water and aqueous NaCl solutions from 273 to 533 K and from 0 to 2000 bar: Chemical Geology, v. 193, no. 3, p. 257-271.

Dvorkin, J., and Nur, A., 1996a, Elasticity of high-porosity sandstones: Theory for two North Sea data sets: Geophysics, v. 61, no. 5, p. 1363-1370.

Dvorkin, J., and Nur, A., 1996b, Elasticity of high-porosity sandstones: Theory for two North Sea data sets: GEOPHYSICS, v. 61, no. 5, p. 1363-1370.

Ellingsrud, S., Eidesmo, T., Johansen, S., Sinha, M., MacGregor, L., and Constable, S., 2002, Remote sensing of hydrocarbon layers by seabed logging (SBL): Results from a cruise offshore Angola: The Leading Edge, v. 21, no. 10, p. 972-982.

Fawad, M., Mondol, N. H., Jahren, J., and Bjorlykke, K., 2011, Mechanical compaction and ultrasonic velocity of sands with different texture and mineralogical composition: Geophysical Prospecting, v. 59, no. 4, p. 697-720.

Feron, P., H.M., and Hendriks, C., A., 2005, Les différents procédés de capture du CO2 et leurs coûts: Oil & Gas Science and Technology - Rev. IFP, v. 60, no. 3, p. 451-459.

Garcia, J. E., and Pruess, K., 2003, Flow Instabilities During Injection of CO2 into Saline Aquifers, Medium: ED p.:

Gassmann, F., 1951a, Elastic waves through a packing of spheres: Geophysics, v. 16, no. 4, p. 673-685.

Gassmann, F. I. f. r. G., 1951b, Uber die Elastizit‰t porˆser Medien, Z¸rich, Inst. f¸r Geophysik an der ETH.

Gelius, L.-J., and Johansen, T. A., 2010, Petroleum geophysics, Bergen, Unigeo.

Ghaderi, A., and Landrø, M., 2009, Estimation of thickness and velocity changes of injected carbon dioxide layers from prestack time-lapse seismic data: Geophysics, v. 74, no. 2, p. O17-O28.

Gunter, W. D., Bachu, S., Law, D. H. S., Marwaha, V., Drysdale, D. L., Macdonald, D. E., and McCann, T. J., 1996, Technical and economic feasibility of CO2 disposal in aquifers within the Alberta sedimentary basin, Canada: Energy Conversion and Management, v. 37, no. 6–8, p. 1135-1142.

Hamada, G., 2004, Reservoir fluids identification using Vp/Vs ratio?: Oil & gas science and technology, v. 59, no. 6, p. 649-654.

Han, D.-h., and Batzle, M. L., 2004, Gassmann's equation and fluid-saturation effects on seismic velocities: Geophysics, v. 69, no. 2, p. 398-405.

Han, D.-h., Nur, A., and Morgan, D., 1986, Effects of porosity and clay content on wave velocities in sandstones: Geophysics, v. 51, no. 11, p. 2093-2107.

Han, D., 1986, Effects of porosity and clay content on acoustic properties of sandstones and unconsolidated sediments. [Ph.D. dissertation: Stanford University.

Han, T., Best, A. I., Sothcott, J., North, L. J., and MacGregor, L. M., 2015, Relationships among low frequency (2 Hz) electrical resistivity, porosity, clay content and permeability in reservoir sandstones: Journal of Applied Geophysics, v. 112, no. 0, p. 279-289.

Hao, Y., Wu, Z., Ju Binshan, C. Y., Luo, X., and Xinjiang, P., 2004, Laboratory investigation of CO2 flooding.: Spe Journal, no. 88883.

Hart, D. J., and Wang, H. F., 1995, Laboratory measurements of a complete set of poroelastic moduli for Berea sandstone and Indiana limestone: Journal of Geophysical Research: Solid Earth, v. 100, no. B9, p. 17741-17751.

Holloway, S., 2005, Underground sequestration of carbon dioxide - a viable greenhouse gas mitigation option: Energy, v. 30, no. 11-12, p. 2318-2333.

Holt, T., Jensen, J. I., and Lindeberg, E., 1995a, Underground storage CO_2 in aquifers and Oil reservoirs: Energy Conversion and Management, v. 36, no. 6, p. 535-538.

-, 1995b, Underground storage of CO2 in aquifers and oil reservoirs, Volume 36, p. 535-538.

Huppert, H. E., and Neufeld, J. A., 2014, The Fluid Mechanics of Carbon Dioxide Sequestration, *in* Davis, S. H., and Moin, P., eds., Annual Review of Fluid Mechanics, Vol 46, Volume 46, p. 255-272.

Ide, S. T., Jessen, K., and Orr, F. M., 2007, Storage of CO2 in saline aquifers: Effects of gravity, viscous, and capillary forces on amount and timing of trapping: International Journal of Greenhouse Gas Control, v. 1, no. 4, p. 481-491.

IPCC, 2005, IPCC: Intergovernmental Panel on Climate Change, IPCC Special report on carbon dioxide capture and storage.

Izgec, O., Demiral, B., Bertin, H., and Akin, S., 2008, CO2 Injection into Saline Carbonate Aquifer Formations II: Comparison of Numerical Simulations to Experiments, Volume 73, p. 57-74.

Jarrell, P. M., and Engineers, S. o. P., 2002, Practical Aspects of CO2 Flooding, Society of Petroleum Engineers, v. v. 1.

Kitamura, K., Xue, Z., Kogure, T., and Nishizawa, O., 2014, The potential of Vs and Vp–Vs relation for the monitoring of the change of CO2-saturation in porous sandstone: International Journal of Greenhouse Gas Control, v. 25, no. 0, p. 54-61.

Klaus, K., David, M., and David, F. B., 2008, Carbon dioxide sequestration: How much when?: Climate Change, v. 88, p. 267-291.

Knight, R., and Nolen-Hoeksema, R., 1990, A laboratory study of the dependence of elastic wave velocities on pore scale fluid distribution: Geophysical Research Letters, v. 17, no. 10, p. 1529-1532.

Krief, M., Stellingwerf, J., and Ventre, J., 1990, A Petrophysical Interpretation Using The Velocities Of P And S Waves (full-waveform Sonic): The Log Analyst, v. 31, no. 06.

Li, Z., Dong, M., Li, S., and Huang, S., 2006, CO2 sequestration in depleted oil and gas reservoirs-caprock characterization and storage capacity: Energy Conversion and Management, v. 47, p. 1372-1382.

Lien, M., and Mannseth, T., 2008, Sensitivity study of marine CSEM data for reservoir production monitoring: Geophysics, v. 73, no. 4, p. F151-F163.

Mathieu, J., 2007, Predicitng absolute and relative permeabilities of carbonate rocks using image analysis and effective medium theory. [PhD: University of London, 182 p.

Mavko, G., and Mukerji, T., 1998, Bounds on low-frequency seismic velocities in partially saturated rocks: Geophysics, v. 63, no. 3, p. 918-924.

Mavko, G., Mukerji, T., and Dvorkin, J., 2009, The Rock Physics Handbook: Tools for Seismic Analysis of Porous Media, Cambridge, Cambridge University Press, 1 online resource (524 s.) : digital, PDF file(s) p.:

Mikhaltsevitch, V., Lebedev, M., and Gurevich, B., 2014, Measurements of the elastic and anelastic properties of sandstone flooded with supercritical CO2: Geophysical Prospecting, v. 62, no. 6, p. 1266-1277.

Moghadam, J. N., Mondol, N. H., Hellevang, H., Johnsen, Ø., and Aagaard, P., Seismic Response of CO2 Saturated Red Wildmoor Sandstone under Varying Temperatures and Pressures, *in* Proceedings 76th EAGE Conference and Exhibition 20142014.

Moore, D. M., and Reynolds, R. C., 1989, X-ray Diffraction and the Identification and Analysis of Clay Minerals, Oxford university press Oxford.

Nakatsuka, Y., Xue, Z., Garcia, H., and Matsuoka, T., 2010, Experimental study on CO2 monitoring and quantification of stored CO2 in saline formations using resistivity measurements: International Journal of Greenhouse Gas Control, v. 4, no. 2, p. 209-216.

Nakatsuka, Y., Xue, Z., Yamada, Y., and Matsuoka, T., 2009, Experimental study on monitoring and quantifying of injected CO2 from resistivity measurement in saline aquifer storage: Energy Procedia, v. 1, no. 1, p. 2211-2218.

Nalinee, C., and Martin, J. B., 2011, Carbon Dioxide storage potential in the North Sea: IPTC, no. 14464.

Oldenburg, C. M., Pruess, K., and Benson, S. M., 2001, Process Modeling of CO2 Injection into Natural Gas Reservoirs for Carbon Sequestration and Enhanced Gas Recovery: Energy Fuels, v. 15, p. 293-298.

Oldenburg, C. M., Unger, A. J. A., Hepple, R. P., and Jordan, P. D., 2002, On leakage and seepage from geological carbon sequestration sites, LBNL--51130; R&D Project: 80TE02; TRN: US200303%%549 United States10.2172/806116R&D Project: 80TE02; TRN: US200303%%549Tue Feb 05 04:48:13 EST 2008OSTI as DE00806116LBNLEnglish.

Ott, H., Berg, S., and Oedai, S., 2012, Displacement and Mass Transfer of CO2/Brine in Sandstone: Energy Procedia, v. 23, p. 512-520.

Peter, D. J., Richard, D. J., Christopher, J. P., and Jonathan, M. P., 1993, Resistivity/porosity/velocity relationship from downhole logs: An aid for evaluating pore morphology.

Prutton, C. F., and Savage, R. L., 1945, The Solubility of Carbon Dioxide in Calcium Chloride-Water Solutions at 75, 100, 120° and High Pressures1: Journal of the American Chemical Society, v. 67, no. 9, p. 1550-1554.

Saito, H., Nobuoka, D., Azuma, H., Xue, Z., and Tanase, D., 2006, Time-lapse crosswell seismic tomography for monitoring injected CO2 in an onshore aquifer, Nagaoka, Japan: Exploration Geophysics, v. 37, no. 1, p. 30-36.

Shi, J.-Q., Xue, Z., and Durucan, S., 2007a, Seismic monitoring and modelling of supercritical CO2 injection into a water-saturated sandstone: Interpretation of P-wave velocity data: International Journal of Greenhouse Gas Control, v. 1, no. 4, p. 473-480.

-, 2007b, Seismic monitoring and modelling of supercritical CO 2 injection into a water-saturated sandstone: Interpretation of P-wave velocity data: International Journal of Greenhouse Gas Control, v. 1, no. 4, p. 473-480.

-, 2011, Supercritical CO2 core flooding and imbibition in Berea sandstone — CT imaging and numerical simulation: Energy Procedia, v. 4, no. 0, p. 5001-5008.

Spears, D. A., 1983, Geochemistry and Mineralogy of Triassic Sandstones and Implications for Groundwater Composition: Mineralogical Magazine 47, (2), 1983 183-190 : Ill.

Spycher, N., and Pruess, K., 2005, CO2-H2O mixtures in the geological sequestration of CO2. II. Partitioning in chloride brines at 12–100°C and up to 600 bar: Geochimica et Cosmochimica Acta, v. 69, no. 13, p. 3309-3320.

Stock, S., and Cullity, B., 2001, Elements of X-ray diffraction: Prentice Hall, Upper Saddle River, New Jersey.

Suekane, T., Soukawa, S., Iwatani, S., Tsushima, S., and Hirai, S., 2005, Behavior of supercritical CO2 injected into porous media containing water: Energy, v. 30, no. 11–12, p. 2370-2382.

Suman, R. J., and Knight, R. J., 1997, Effects of pore structure and wettability on the electrical resistivity of partially saturated rocks-A network study: Geophysics, v. 62, no. 4, p. 1151-1162.

Toms, J., Müller, T. M., Ciz, R., and Gurevich, B., 2006, Comparative review of theoretical models for elastic wave attenuation and dispersion in partially saturated rocks: Soil Dynamics and Earthquake Engineering, v. 26, no. 6–7, p. 548-565.

Van Den Abeele, K. E. A., Carmeliet, J., Johnson, P. A., and Zinszner, B., 2002, Influence of water saturation on the nonlinear elastic mesoscopic response in Earth materials and the implications to the mechanism of nonlinearity: Journal of Geophysical Research: Solid Earth, v. 107, no. B6, p. ECV 4-1-ECV 4-11.

Vargaftik, N. B., Vinogradov, J. K., and Jargin, V. S., 1996, Handbook of physical properties of liquids and gases: pure substances and mixtures, New York, Begell House, VI, 1358 s. : ill. p.:

Wang, Z., 2000, The Gassmann equation revisited: Comparing laboratory data with Gassmann's predictions: Seismic and acoustic velocities in reservoir rocks, v. 3, p. 8-23.

Wang, Z., Cates, M. E., and Langan, R. T., 1998, Seismic monitoring of a CO2 flood in a carbonate reservoir: A rock physics study: Geophysics, v. 63, no. 5, p. 1604-1617.

Wang, Z., Gelius, L.-J., and Kong, F.-N., 2009, Simultaneous core sample measurements of elastic properties and resistivity at reservoir conditions employing a modified triaxial cell – a feasibility study: Geophysical Prospecting, v. 57, no. 6, p. 1009-1026.

Wang, Z., and Nur, A., 1989, Effects of CO2 flooding on wave velocities in rocks with hydrocarbons.

White, S. P., Allis, R. G., Moore, J., Chidsey, T., Morgan, C., Gwynn, W., and Adams, M., 2003, Injection of CO2 into an Unconfined Aquifer Located Beneath the Colorado Plateau, Central Utah.

Wiebe, R., and Gaddy, V. L., 1939, The Solubility in Water of Carbon Dioxide at 50, 75 and 100°, at Pressures to 700 Atmospheres: Journal of the American Chemical Society, v. 61, no. 2, p. 315-318.

Winkler, K. W., 1986, Estimates of velocity dispersion between seismic and ultrasonic frequencies: Geophysics, v. 51, no. 1, p. 183-189.

Winkler, K. W., and Murphy, W. F., 1995, Acoustic velocity and attenuation in porous rocks: Rock Physics & Phase Relations: A Handbook of Physical Constants, p. 20-34.

Winkler, K. W., and Nur, A., 1982, Seismic attenuation: Effects of pore fluids and frictional-sliding: Geophysics, v. 47, no. 1, p. 1-15.

Winterstein, D. F., 1990, Velocity anisotropy terminology for geophysicists: GEOPHYSICS, v. 55, no. 8, p. 1070-1088.

Wissler, T. M., and Simmons, G., 1985, The physical properties of a set of sandstones—Part II. Permanent and elastic strains during hydrostatic compression to 200 MPa: International

Journal of Rock Mechanics and Mining Sciences & Geomechanics Abstracts, v. 22, no. 6, p. 393-406.

Wood, A., 1941, A textbook of Sound,: Bell, London.

Worthington, P. F., 1993, THE USES AND ABUSES OF THE ARCHIE EQUATIONS .1. THE FORMATION FACTOR POROSITY RELATIONSHIP: Journal of Applied Geophysics, v. 30, no. 3, p. 215-228.

Wyllie, M., Gregory, A., and Gardner, L., 1956, ELASTIC WAVE VELOCITIES IN HETEROGENEOUS AND POROUS MEDIA: GEOPHYSICS, v. 21, no. 1, p. 41-70.

Wyllie, M. R. J., and Gregory, A. R., 1953, FORMATION FACTORS OF UNCONSOLIDATED POROUS MEDIA - INFLUENCE OF PARTICLE SHAPE AND EFFECT OF CEMENTATION: Transactions of the American Institute of Mining and Metallurgical Engineers, v. 198, p. 103-110.

Wynn, D., Ajo-Franklin, J., Wu, C., Urban, J., and Akintunde, O. M., 2003, Subsurface Monitoring of Geological CO2 Storage.

Xue, Z., Kim, J. W., Mito, S., Kitamura, K., and Matsuoka, T., 2009, Detecting and Monitoring CO2 With P-Wave Velocity and Resistivity From Both Laboratory and Field Scales, Society of Petroleum Engineers.

Xue, Z., and Lei, X., 2006, Laboratory study of CO2 migration in water-saturated anisotropic sandstone, based on P-wave velocity imaging: Exploration Geophysics, v. 37, no. 1, p. 10-18.

Xue, Z., and Ohsumi, T., 2004, Seismic wave monitoring of CO2 migration in water-saturated porous sandstone: Exploration Geophysics, v. 35, no. 1, p. 25-32.

Xue, Z., Ohsumi, T., and Koide, H., Laboratory measurement of seismic wave velocity by CO2 injection in two porous sandstones, *in* Proceedings Proceedings of the 6th International Conference on Greenhouse Gas Control Technologies (GHGT-6)2002, p. 359-364.

Xue, Z., Tanase, D., and Watanabe, J., 2006, Time-lapse CO2 monitor logging in the first pilot-scale CO2 injection site in Japan., Proceedings of the 8th SEGJ International Symposium, Kyoto, Japan, 26-28 November 2006, Society of Exploration Geophysicists of Japan, p. 1-5.

Zhou, D., and Stenby, E. H., 1997, A percolation study of wettability effect on the electrical properties of reservior rocks: Transport in porous media, v. 29, no. 1, p. 85-98.

Zhu, X., and McMechan, G. A., Direct estimation of the bulk modulus of the frame in a fluid-saturated elastic medium by Biot Theory, *in* Proceedings 60th Ann. Internat. Mtg., SEG Expanded Abstracts1990, Volume 9, p. 787.

Appendix A: Velocities

Vertical Red Wildmoor

Table A.1 Axial and radial velocities for loading and unloading cycles

Test	Vs,axial [m/s]	Vp,axial [m/s]	Vp,rad(B) [m/s]	Vp,rad(M) [m/s]	Vp,rad(T) [m/s]
Dry	1733,465	2969,796	2734,619	2662,966	2849,632
CO2	1722,467	2825,456	2532,096	2502,644	2392,135
Brine	1638,129	3127,447	2911,674	2824,651	2972,729

Table A.0.1 Measured axial and radial velocities for drainage

PV	Flow rate	Vs,axial	Vp,axial	Vp,rad(B)	Vp,rad(M)	Vp,rad(T)
0	0,5	1660,498	3140,405	2970,323	2903,107	2831,809
0,1	0,5	1682,987	3106,422	2967,742	2890,827	2820,758
0,3	0,5	1683,317	3065,631	2907,822	2807,905	2758,249
0,5	0,5	1685,697	2990,061	2873,368	2741,15	2701,358
0,7	0,5	1689,629	2948,318	2857,202	2710,51	2659,498
0,9	0,5	1691,989	2918,123	2842,723	2703,296	2646,763
1	0,5	1694,614	2898,264	2824,776	2698,636	2633,041
2	2,5	1699,482	2865,37	2750,167	2671,021	2586,122
4	2,5	1702,281	2843,087	2724,055	2658,549	2558,309
6	2,5	1710,808	2844,544	2706,596	2623,296	2548,939
8	2,5	1713,758	2852,187	2696,688	2614,35	2544,448

Table A.0.2 Calculated Gassmann's velocities

		Axial		Radial	
PV	Flow rate	Vs,axial	Vp,axial	Vs,axial	Vp,axial
0	0,5	1651,333	2972,938	1651,333	2972,938
0,1	0,5	1654,502	2954,207	1648,924	2987,899
0,3	0,5	1664,468	2901,195	1670,074	2874,561
0,5	0,5	1672,067	2865,546	1680,136	2831,145

0,7	0,5	1675,096	2852,26	1682,019	2823,547
0,9	0,5	1675,544	2850,335	1682,078	2823,309
1	0,5	1675,473	2850,638	1681,904	2824,005
2	2,5	1681,975	2823,723	1685,06	2811,579
4	2,5	1683,59	2817,318	1686,089	2807,608
6	2,5	1683,976	2815,803	1686,365	2806,551
8	2,5	1684,065	2815,454	1686,418	2806,349

Table A.0.3 Measured velocities for imbibition

Imbibition.						
PV	Flow rate	Vs,axial	Vp,axial	Vp,rad(B)im	Vp,rad(M)im	Vp,rad(T)im
0	0,5	1654,792	2876,74	2700,663	2617,167	2442,003
0,1	0,5	1656,902	2895,215	2697,766	2597,462	2559,782
0,3	0,5	1655,982	2909,125	2706,507	2603,939	2563,097
0,5	0,5	1643,132	2930,132	2720,614	2617,724	2555,952
0,7	0,5	1638,062	2941,922	2727,92	2629,997	2557,866
0,9	0,5	1633,884	2971,245	2735,066	2655,265	2554,563
1	0,5	1632,818	2990,622	2741,649	2682,171	2557,865
2	2,5	1631,272	3029,196	2767,898	2735,864	2614,447
4	2,5	1628,874	3069,143	2837,055	2860,155	2680,452
6	2,5	1625,15	3083,058	2879,878	2866,48	2745,656
8	2,5	1617,957	3096,113	2907,053	2868,449	2812,638
9	2,5	1618,632	3104,546	2921,967	2873,271	2825,535

Table A.0.4 Gassmann-modelled velocities for imbibition

		Axial		Radial	
PV	Flow rate	Vs,axial	Vp,axial	Vs,axial	Vp,axial
0	0,5	1682,952	2819,835	1684,985	2811,868
0,1	0,5	1671,646	2867,434	1675,41	2850,907
0,3	0,5	1670,323	2873,424	1675,384	2851,022
0,5	0,5	1670,373	2873,192	1676,54	2846,089
0,7	0,5	1670,409	2873,03	1677,178	2843,393

0,9	0,5	1670,054	2874,652	1677,017	2844,073
1	0,5	1669,744	2876,076	1676,812	2844,935
2	2,5	1665,084	2898,17	1668,468	2881,992
4	2,5	1658,19	2933,627	1662,99	2908,564
6	2,5	1654,121	2956,403	1657,652	2936,556
8	2,5	1651,957	2969,17	1652,369	2966,7
9	2,5	1651,333	2972,938	1651,333	2972,938

Horizontal Red Wildmoor.

Table A.0.5 Axial and radial velocities for loading and unloading cycles

Test	Vs,axial [m/s]	Vp,axial [m/s]	Vp,rad(B) [m/s]	Vp,rad(M) [m/s]	Vp,rad(T) [m/s]
Dry	1844,786	2773,337	2647,333	2775,433	2572,209
CO2	1768,719	2677,395	2605,974	2642,414	2512,594
Brine	1603,134	3009,235	2943,899	2980,364	2869,653

Table A.0.6 Measured velocities for drainage

PV	Flow rate	Vs,axial	Vp,axial	Vp,rad(B)	Vp,rad(M)	Vp,rad(T)
0	0,5	1619,659	2994,965	2947,493	2923,767	2807,72
0,1	0,5	1625,644	2928,298	2886,016	2758,109	2722,92
0,3	0,5	1638,744	2881,827	2842,582	2741,694	2700,096
0,5	0,5	1641,004	2869,793	2823,249	2728,624	2691,936
0,7	0,5	1640,16	2867,109	2824,726	2728,033	2690,449
0,9	0,5	1639,115	2875,279	2817,143	2731,386	2685,559
1	0,5	1638,71	2866,594	2820,087	2734,352	2676,236
2	2,5	1639,485	2786,73	2797,117	2714,311	2630,759
4	2,5	1642,502	2743,95	2765,378	2678,323	2612,926
6	2,5	1649,195	2732,195	2757,103	2668,296	2603,561
8	2,5	1653,127	2742,251	2746,479	2671,504	2594,263
9	2,5	1655,256	2753,808	2733,956	2668,484	2601,409

Table A.0.7 Gassmann-modelled velocities for drainage

	Axial	Radial

PV	Flow rate	Vs,axial	Vp,axial	Vs,rad	Vp,rad
0	0,5	1651,333	2972,938	1651,333	2972,938
0,1	0,5	1663,008	2908,471	1664,113	2902,949
0,3	0,5	1670,13	2874,306	1670,964	2870,506
0,5	0,5	1672,171	2865,084	1672,796	2862,305
0,7	0,5	1672,483	2863,694	1672,841	2862,106
0,9	0,5	1672,852	2862,058	1673,153	2860,726
1	0,5	1672,729	2862,6	1673,153	2860,726
2	2,5	1678,066	2839,677	1677,250	2843,089
4	2,5	1679,879	2832,193	1681,263	2826,581
6	2,5	1680,518	2829,591	1682,665	2820,973
8	2,5	1680,434	2829,932	1682,748	2820,646
9	2,5	1680,434	2829,932	1682,748	2820,646

Table A.0.8 Measured velocities for imbibition

PV	Flow rate	Vs,axial	Vp,axial	Vp,rad(B)	Vp,rad(M)	Vp,rad(T)
0	0,5	1656,029	2793,592	2760,515	2625,252	2520,158
0,1	0,5	1655,584	2824,177	2783,502	2643,071	2564,647
0,3	0,5	1656,65	2836,232	2782,477	2644,551	2566,564
0,5	0,5	1639,545	2856,762	2800,217	2651,234	2585,893
0,7	0,5	1632,63	2866,524	2812,1	2661,509	2605,514
0,9	0,5	1620,383	2887,391	2849,436	2671,295	2629,638
1	0,5	1623,385	2891,893	2894,416	2691,09	2662,072
2	2,5	1620,027	2931,898	2966,476	2885,793	2768,001
4	2,5	1616,344	3011,183	3032,447	3073,656	2910,924
6	2,5	1616,146	3051,174	3070,655	3113,173	3021,529
8	2,5	1613,3	3083,391	3086,967	3145,057	3048,106
9	2,5	1613,689	3087,686	3089,744	3165,881	3057,234

Table A.0.9 Gassman modelled velocities for imbibition

		Axial		Radial	
PV	Flow rate	Vs,axial	Vp,axial	Vs,rad	Vp,rad
0	0,5	1677,803	2840,774	1680,458	2829,837
0,1	0,5	1668,737	2880,735	1674,696	2853,987
0,3	0,5	1667,797	2885,138	1674,393	2855,303
0,5	0,5	1667,043	2888,712	1674,093	2856,608
0,7	0,5	1666,292	2892,308	1673,476	2859,307
0,9	0,5	1665,452	2896,373	1672,871	2861,973
1	0,5	1665,067	2898,251	1672,492	2863,655
2	2,5	1660,645	2920,583	1667,772	2885,26
4	2,5	1651,482	2972,033	1651,323	2973,001
6	2,5	1652,43	2966,337	1651,887	2969,587
8	2,5	1651,482	2972,033	1651,323	2973,001
9	2,5	1651,333	2972,938	1651,333	2972,938

Berea sandstone

Table A.0.10 Axial and radial velocities for loading and unloading cycles

Test	Vs [m/s]	Vp [m/s]	Vp,rad(B) [m/s]	Vp,rad(M) [m/s]	Vp,rad(T) [m/s]
Dry	2592,624	4210,091	3542,263	3545,334	3632,105
CO2	2528,773	4160,657	3571,529	3563,574	3631,8
Brine	2366,869	4543,215	4078,057	3953,14	3902,449

Table A.0.11 Measured velocities for drainage

Drainage						
PV	Flow rate [mL/min]	Vs [m/s]	Vp [m/s]	Vp,rad(B) [m/s]	Vp,rad(M) [m/s]	Vp,rad(T) [m/s]
0	0,5	2601,228	4385,44	3985,187	3968,235	3902,205
0,1	0,5	2619,116	4384,955	3879,762	3901,692	3722,318
0,2	0,5	2625,833	4338,39	3824,107	3834,63	3698,367
0,3	0,5	2628,459	4300,763	3810,365	3803,078	3695,395

0,4	0,5	2627,847	4290,234	3811,626	3791,475	3702,087
0,5	0,5	2628,548	4274,418	3808,822	3779,516	3698,364
0,6	0,5	2628,813	4271,643	3805,902	3774,199	3694,645
0,7	0,5	2628,022	4263,554	3803,778	3773,156	3690,569
0,8	0,5	2627,673	4261,943	3801,85	3763,696	3694,644
0,9	0,5	2628,285	4254,123	3800,436	3762,888	3690,197
1	0,5	2629,249	4252,059	3796,512	3757,429	3694,641
2	2,5	2629,778	4240,4	3771,564	3745,035	3672,146
4	2,5	2630,741	4227,437	3760,883	3720,418	3671,045
6	2,5	2631,619	4224,491	3758,579	3722,301	3669,216
8	2,5	2632,415	4219,076	3754,497	3700,943	3668,103
9	2,5	2633,118	4217,947	3754,344	3700,198	3664,084
10	2,5	2633,909	4213,439	3752,811	3687,218	3662,624
11	2,5	2632,5	4211,184	3747,001	3680,577	3669,198

Table A.0.12 Velocities from Gassmann's model during drainage

PV	[mL/min]	Vs	Vp	Vp,rad(B)	Vp,rad(M)	Vp,rad(T)
0	0,5	2118,05	4596,859	4596,859	4596,859	4596,859
0,1	0,5	2118,062	4594,914	4592,703	4595,226	4597,398
0,2	0,5	2121,593	4408,275	4635,636	4468,653	4351,575
0,3	0,5	2123,346	4373,603	4385,937	4348,292	4335,665
0,4	0,5	2124,34	4356,966	4347,828	4337,646	4330,405
0,5	0,5	2124,561	4353,456	4345,259	4334,348	4327,461
0,6	0,5	2124,697	4351,318	4341,338	4331,967	4325,082
0,7	0,5	2124,734	4350,734	4337,933	4330,26	4323,138
0,8	0,5	2124,901	4348,141	4336,573	4328,48	4321,162
0,9	0,5	2125	4346,629	4336,284	4327,104	4319,623
1	0,5	2125,071	4345,543	4336,06	4326,038	4318,304
2	2,5	2125,124	4344,728	4335,049	4325,151	4317,167
4	2,5	2125,917	4332,892	4324,813	4317,838	4309,982
6	2,5	2126,469	4324,908	4317,099	4310,609	4303,441
8	2,5	2126,549	4323,761	4312,46	4306,763	4302,002
9	2,5	2126,793	4320,287	4309,661	4304,622	4299,598
10	2,5	2126,865	4319,274	4308,7	4303,708	4298,224
11	2,5	2126,916	4318,55	4307,772	4302,932	4297,061

Table A.0.13 Measured velocities for imbibition

PV	Flow rate [mL/min]	Vs [m/s]	Vp [m/s]	Vp,rad(B) [m/s]	Vp,rad(M) [m/s]	Vp,rad(T) [m/s]
0	0,5	2635,403	4214,111	3749,207	3685,362	3666,631
0,1	0,5	2634,614	4243,6	3786,914	3719,268	3700,191
0,2	0,5	2633,558	4247,029	3778,473	3713,261	3702,424
0,3	0,5	2632,503	4252,986	3779,909	3717,012	3702,796
0,4	0,5	2631,186	4259,42	3779,598	3722,654	3697,958
0,5	0,5	2630,132	4259,186	3777,851	3744,972	3701,306
0,6	0,5	2628,815	4261,257	3779,791	3763,667	3706,153
0,7	0,5	2627,501	4264,945	3794,799	3777,306	3701,304
0,8	0,5	2628,113	4273,266	3817,394	3793,736	3704,652
0,9	0,5	2628,113	4275,35	3825,053	3813,278	3710,629
1	0,5	2628,375	4281,153	3831,899	3820,201	3726,786
2	2,5	2619,743	4306,664	3854,15	3848,465	3777,071
4	2,5	2617,118	4322,359	3871,385	3856,586	3784,018
6	2,5	2613,433	4331,896	3883,282	3872,642	3799,888
8	2,5	2610,358	4339,276	3894,532	3889,42	3819,76
9	2,5	2610,639	4356,809	3909,15	3899,678	3834,744
10	2,5	2604,244	4367,039	3917,88	3911,984	3851,138
11	2,5	2600,586	4378,44	3931,187	3916,235	3879,205

Table A.0.14 Gassmann-modelled velocities for imbibiton

PV	Flow rate [mL/min]	Vs [m/s]	Vp [m/s]	Vp,rad(B) [m/s]	Vp,rad(M) [m/s]	Vp,rad(T) [m/s]
0	0,5	2126,629	4322,616	4307,217	4309,034	4302,637
0,1	0,5	2123,996	4362,566	4359,201	4364,619	4356,871
0,2	0,5	2123,916	4363,881	4360,459	4362,806	4357,923
0,3	0,5	2123,86	4364,814	4364,238	4360,888	4356,574
0,4	0,5	2123,793	4365,932	4370,935	4361,769	4355,387
0,5	0,5	2123,687	4367,728	4378,569	4363,072	4355,221
0,6	0,5	2123,557	4369,945	4385,791	4364,474	4355,657
0,7	0,5	2123,414	4372,405	4392,699	4365,809	4356,534

0,8	0,5	2123,262	4375,082	4399,703	4367,086	4357,598
0,9	0,5	2123,105	4377,884	4407,391	4368,286	4358,803
1	0,5	2122,954	4380,63	4415,45	4369,378	4360,096
2	2,5	2121,536	4409,579	4482,339	4382,077	4383,174
4	2,5	2120,105	4449,891	4551,683	4446,684	4402,847
6	2,5	2119,25	4487,006	4605,707	4510,964	4428,76
8	2,5	2118,628	4529,186	4623,106	4557,292	4476,006
9	2,5	2118,418	4549,139	4626,956	4586,316	4509,538
10	2,5	2118,261	4567,036	4627,505	4606,258	4550,048
11	2,5	2118,149	4581,832	4628,543	4613,689	4586,351

Appendix B: Resistivities and saturation

Table B.0.1 Horizontal Red Wildmoor.

	Saturation			
PV	Drainage		Imbibition	
	Axial	Radial	Axial	Radial
0	0	0	0,37762	0,40117
0,1	0,03883	-0,0297	0,24505	0,28949
0,3	0,15948	0,2264	0,22936	0,28917
0,5	0,25004	0,34485	0,22996	0,30276
0,7	0,28579	0,36678	0,23038	0,31025
0,9	0,29106	0,36747	0,22617	0,30836
1	0,29023	0,36544	0,22248	0,30596
2	0,36627	0,40203	0,16687	0,2073
4	0,38502	0,41393	0,08373	0,14172
6	0,38949	0,41711	0,03417	0,0772
8	0,39052	0,41772	0,00766	0,01272
9	-	-	0	0

Table B.0.1 Vertical Red Wildmoor.

	Saturation			
Pore volume	Drainage		Imbibition	
	Axial	Radial	Axial	Radial
0	0	0	0.317572	0.348599
0.1	0.141945	0.155224	0.210504	0.281078
0.3	0.227064	0.23697	0.199309	0.277501
0.5	0.251261	0.258656	0.190308	0.273967
0.7	0.254955	0.259188	0.181331	0.266688
0.9	0.259316	0.262881	0.171276	0.259544
1	0.257871	0.262881	0.166667	0.255058
2	0.320649	0.311099	0.113454	0.199
4	0.341851	0.357978	0.001831	-0.00013
6	0.349305	0.374285	0.013463	0.006805
8	0.348326	0.375243	0.001831	-0.00013

9	0.348326	0.375243	0	0

Table B.0.2 Berea sandstone drainage.

Pore volume	R,ax	R,rad(T)	R,rad(M)	R,rad(B)
0	0,00	0,00	0,00	0,00
0,1	0,00	0,00	0,00	0,00
0,2	0,18	0,33	0,08	-0,01
0,3	0,27	0,39	0,34	0,23
0,4	0,32	0,40	0,38	0,35
0,5	0,33	0,41	0,39	0,35
0,6	0,33	0,42	0,40	0,37
0,7	0,34	0,43	0,40	0,38
0,8	0,34	0,44	0,41	0,38
0,9	0,35	0,44	0,42	0,38
1	0,35	0,45	0,42	0,38
2	0,36	0,45	0,42	0,39
4	0,40	0,48	0,45	0,42
6	0,42	0,50	0,47	0,45
8	0,43	0,50	0,49	0,47
9	0,44	0,51	0,50	0,48
10	0,44	0,52	0,50	0,48
11	0,45	0,52	0,50	0,48

Table B.0.3 Berea sandstone imbibition.

Pore Volume	R,ax	R,rad(T)	R,rad(B)	R,rad(M)
0	26,22	36,72	33,92	36,18
0,1	17,28	20,35	17,98	19,62
0,2	17,09	20,13	17,81	19,97
0,3	16,95	19,48	18,03	20,26
0,4	16,79	18,43	18,22	20,11
0,5	16,54	17,37	18,25	19,88
0,6	16,24	16,50	18,18	19,64
0,7	15,93	15,76	18,03	19,42
0,8	15,60	15,09	17,86	19,22
0,9	15,27	14,49	17,66	19,06
1	14,96	13,86	17,46	18,86

2	12,49	11,09	14,53	17,11
4	10,56	10,05	12,81	12,33
6	9,61	9,65	11,28	10,66
8	9,00	9,56	9,73	10,10
9	8,81	9,54	9,14	9,87
10	8,67	9,54	8,70	9,75
11	8,57	9,53	8,45	9,71

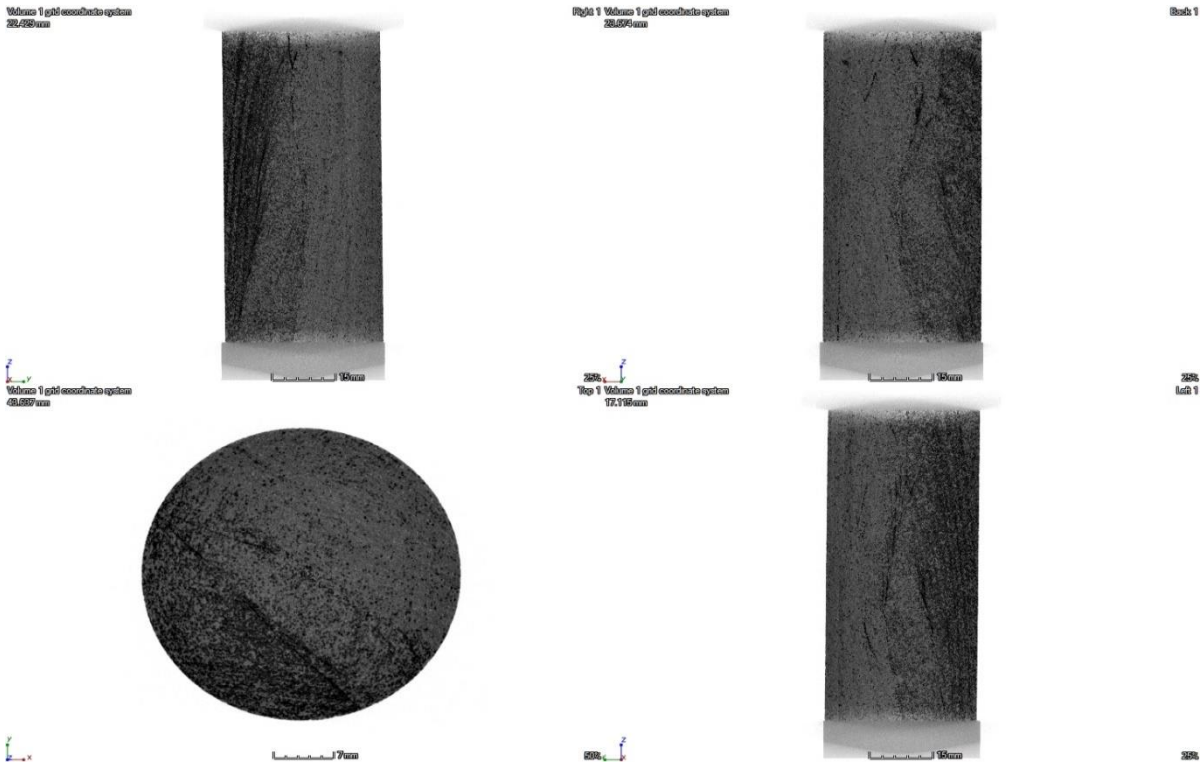

Figure A-1 CT scan image for low permeable Berea Sandstone

Appendix C: Submitted and accepted abstracts

1. Geophysical monitoring of CO2 flow during sandstone flooding experiments

Introduction

Geological storage of carbon dioxide (CO2) is often considered one of the most promising options for reducing anthropogenic CO2 emissions from large-scale point sources. Saline aquifers and producing/abandoned hydrocarbon reservoirs are good candidates for such large-scale CO2 geological storages (e.g. those in North Sea). In the initial phase of injection, the CO2 will be physically and hydro-dynamically trapped in the pores of the reservoir rock and the formation's petrophysical properties will change as CO2 replaces the formation fluid (Alemu *et al*. 2013). Monitoring the injected CO2 in terms of direct measurement of the petrophysical formation properties is, however, not practically viable. Instead, geophysical field monitoring is conducted which can provide temporal and spatial variations of seismic velocity, electrical resistivity, density and anisotropy of the formation. Proper use of relevant rock physics can then relate changes in geophysical signature to changes in petrophysical properties of the formation (Alnes *et al*. 2011, Arts *et al*. 2008, Chadwick *et al*. 2005, and Park *et al*. 2014).

In this study, liquid CO2 is injected into initially brine saturated reservoir core samples in the laboratory, and consequently changes in electrical resistivity, acoustic velocities (ultrasonic frequency) and their anisotropy are monitored. To enhance the spatial resolution, a system enabling velocity and resistivity measurements at different points along the specimen's axial direction has been developed. Saturation levels and fluid distribution pattern within the porous system is also planned to be mapped using a high resolution X-ray Computed Tomography (CT) scanner (similar to Alemu *et al*. 2013) and will form a reference for the geophysical measurements. The study is still ongoing and results should be treated as preliminary. So far, focus has been related to CO2 geological storage, but the outline of the study is believed to also be applicable for CO2 injection for enhanced oil recovery (EOR).

Method

The laboratory investigations are conducted in a hydrostatic pressure vessel in which confining and pore pressures are controlled using different pressure controllers. Deformation of the sandstone core samples are monitored in both axial and radial direction utilizing LVDT strain gages mounted onto the samples. A rubber membrane with an array of compressional (P-wave) piezo-ceramic crystals embedded into it at three different levels across the sample length is utilized as the sealing agent between the sample and the surrounding confining oil (Figure 1). Compressional and shear (S-wave) piezo-ceramic crystals are also fixed inside the top cap and bottom pedestal enabling measurements of axial velocity. Both radial and axial acoustic crystals are employed as electrodes during resistivity monitoring.

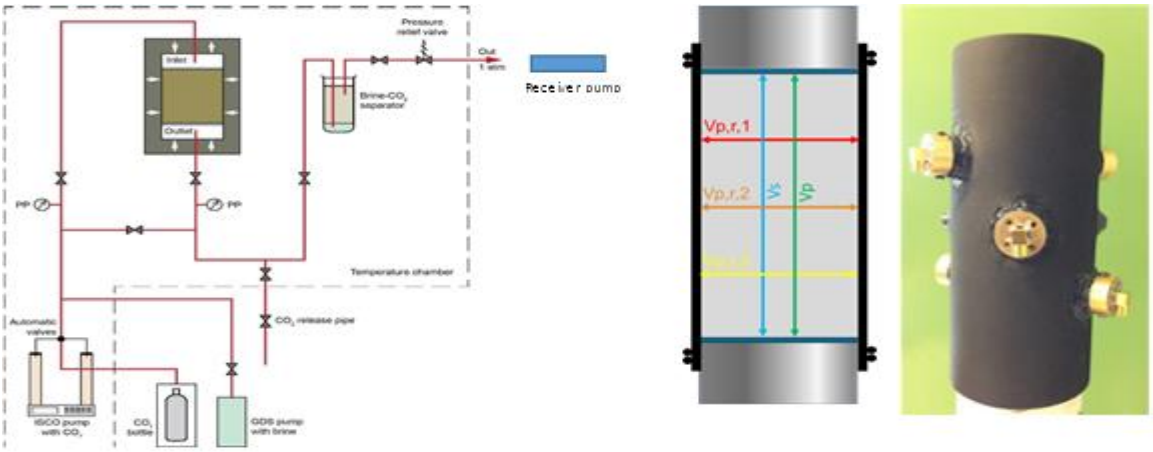

Figure 1 Experimental set-up and the instrumented rubber membrane.

Sample material and test protocol

Cylindrical samples with diameter of 38 mm and height of approximately 80 mm are prepared from well-known sandstone formations (Red Wildmoor, Gres des Vosges and Berea). To study the effect of sample orientation on CO2 flow pattern, core plugs are drilled both parallel and perpendicular to bedding plane (see Figure 2). The different formations represent differences in terms of layering, permeability and mineralogy.

After mounting the samples inside the cell, they are subjected to three hydrostatic load cycles; one in dry conditions, one in liquid CO2-saturated conditions and one in brine-saturated conditions. The effective isotropic stress cycles range from 1 to 15 MPa, and when liquids are present in the sample the pore pressure is kept at 10 MPa. Next, liquid CO2 is injected from top into the brine-saturated samples in volumetric steps corresponding to fractions of the total pore volume (i.e 0.1 PV, 0.2 PV etc) until a total of approximately 10-15 pore volumes are injected (CO2 drainage). Then fresh brine (30 g/l NaCl) is injected into the bottom of the sample (brine imbibition) in the same manner as for CO2. Throughout the experiment, sample deformation, acoustic velocities and electrical resistivity are measured.

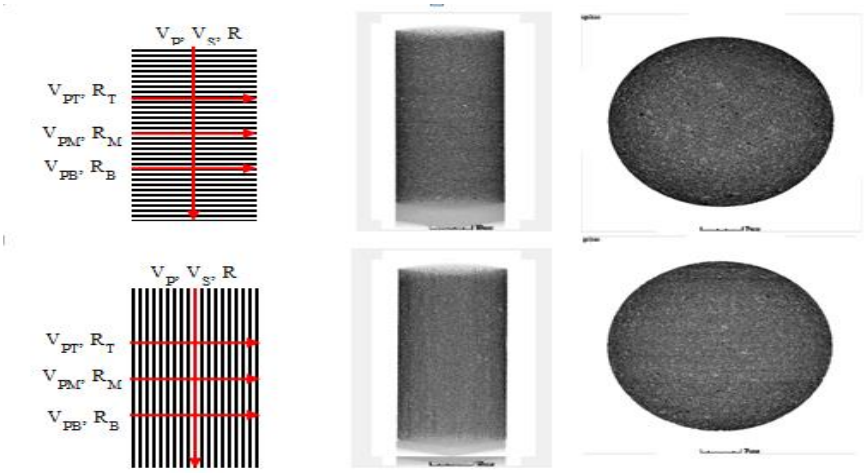

Figure 2 Sensor orientation relative to rock sample bedding.

Results

Figure 3 shows the efficiency of both acoustic velocity (left) and electrical resistivity (right) in detecting the CO2 front movement. Additionally, the combination of axial and radial measurements at different points along the sample axis clearly displays both material anisotropy and heterogeneity (in pore-scale). As the liquid CO2 moves from the inlet (top) towards the outlet (bottom) of the sample, the decrease in both density and bulk modulus of the rock/fluid system causes the acoustic P-wave velocity to drop, well in accordance with common mixing laws (Brie, 1995). Note that the decrease in the latter is more significant than that of the former. As conductive brine is displaced from the porous network, the electrical resistivity is seen to gradually decrease before stabilizing at some level indication that a final CO2 saturation level has been reached.

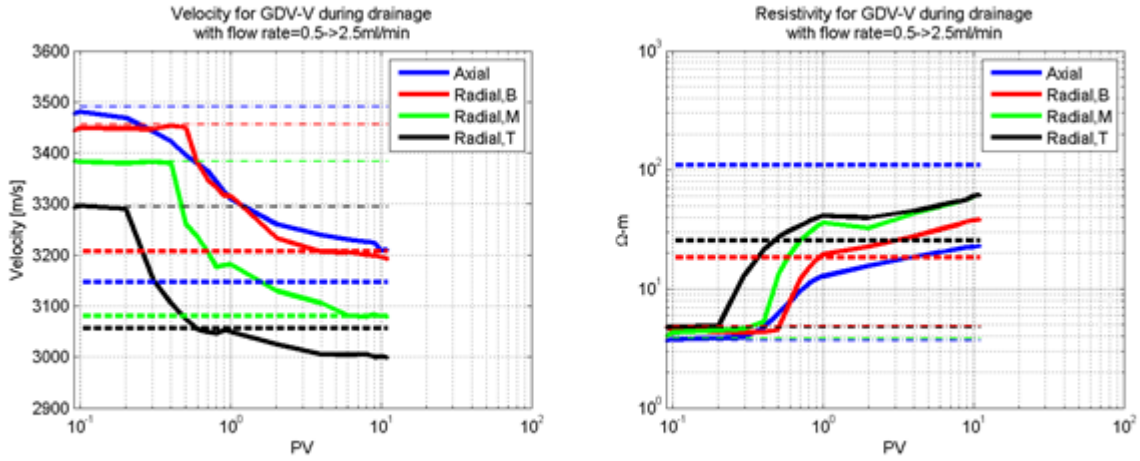

Figure 3 P-wave velocity (left) and electrical resistivity change as a function of injected pore volumes of liquid CO2 for Gres des Vosges sandstone drilled perpendicular to layering.

Archie (1942) formulated an empirical relationship between resistivity and relative saturation of a porous medium based on measured electrical DC conductivity of brine-saturated sandstone cores:

$$I = \frac{R_t}{R_0} = \frac{b}{S_w^{-n}}$$

Where I is the resistivity index, R_0 is the resistivity of the fully brine-saturated media, R_t is the resistivity of the media saturated with both brine and non-wetting fluid, b is a real constant equal to 1, S_w is the water saturation and n is the saturation exponent. Saturation levels determined from CO2 experiments in the X-ray CT scanner will be used to determine appropriate values of the saturation exponent (similar to Alemu et.al (2013)), enabling fairly accurate saturation estimates based on measurements of electrical resistivity. Examination of acoustic P-wave velocity and amplitude can give additional insight into both saturation levels and CO2 flow pattern (linked to attenuation).

Conclusions

We present the results from laboratory measurements of both radial and axial seismic velocities and electrical resistivity during CO2 flooding experiments of sandstone core samples. Liquid CO2 in injected into fully brine-saturated sandstones in volumetric increments and the geophysical response is monitored. Parallel experiments in the CT scanner with only axial geophysical monitoring will be performed, enabling determination of reference saturation levels. Electrical resistivity and acoustic

velocity and amplitude are all clearly influenced by pore-scale heterogeneity and fluid flow pattern and it is important to study this interaction. The study is still on-going and more results will be published in near future.

Acknowledgement

We appreciate the support from SUCCESS FME centre for CO2 storage under grant 193825/S60 from Research Council of Norway (RCN). We also thank for the financial and scientific contributions from NGI GBV 20120265.

References

1. Alemu, B.L., Aker, E., Soldal, M., Johnsen, Ø. and Aagaard, P. [2013] Effect of sub-core scale heterogeneities on acoustic and electrical properties of a reservoir rock: a CO2 flooding experiment of brine saturated sandstone in a computed tomography scanner, Geophysical Prospecting, 61(1), 235-250.
2. Alnes, H., Eiken, O., Nooner, S., Sasagawa, G., Steinvold, T. and Zumberg, M. [2011] Results from Sleipner gravity monitoring: Updated density and temperature distribution of the CO2 plume. Energy Procedia, 4, 5504-5511.
3. Archie, G.E. 1942. The Electrical Resistivity Log as an Aid in Determining Some Reservoir Characteristics.
4. Arts, R., Chadwick, A., Eiken, O., Thibeau, S. and Nooner, S. [2008] Ten years' experience of monitoring CO2 injection in the Utsira Sand at Sleipner offshore Norway, First Break, 26, 65-72.
5. Brie, A., Pampuri, F., Marasala, A.F. & Meazza, O. 1995. Shear sonic interpretation in gasbearing sands. *Society of Petroleum Engineers* SPE No. 30595.
6. Chadwick, R.A., Arts, R. and Eiken, O. [2005] 4D seismic quantification of a growing CO2 plume at Sleipner, North Sea, In: Doré, A.G. & Vining, B. (editors), Petroleum Geology: North-West Europe and Global Perspectives – Proceedings of the 6th Petroleum Geology Conference, 1385-1399.
7. Park, J., Vanneste, M., Bohloli, B., Viken, I., Bjørnarå, T.I. [2014] In situ resistivity of CO2 plume at Sleipner from CSEM and gravity data, Fourth EAGE CO2 Geological Storage Workshop, 22-24 April 2014, Stavanger, Norway

Title: Geophysical monitoring of CO2 flow during sandstone flooding experiments

Author list: Magnus Soldal, Joonsang Park, Lamech O. Omolo, Truong Tran, Øistein Johnsen, Guillaume Sauvin, and Nazmul Haque Mondol.

Summary:

In this study, liquid CO2 is injected into fully brine saturated reservoir core samples in the laboratory, and consequently changes in electrical resistivity, acoustic velocities (ultrasonic frequency) and their anisotropy are measured. To enhance the spatial resolution, a system enabling velocity and resistivity measurements at different points and in different directions along the specimen's axial direction has been developed. Electrical resistivity and acoustic velocity and amplitude are all clearly influenced by pore-scale heterogeneity and fluid flow pattern and it is important to study this interaction. So far, focus has been related to CO2 geological storage, but the outline of the study is believed to also be applicable for CO2 injection for enhanced oil recovery (EOR). The study is still ongoing and some preliminary results are presented here and discussed.

2. Multidirectional acoustic velocity measurement during CO_2 flooding in sandstones

L.O. Omolo[a], T. Tran[a], M. Soldal[b], N. H. Mondol[a,b], L. Grande[b], J. Park[b] and Ø. Johnsen[c]

[a]Department of Geosciences, University of Oslo, [b]Norwegian Geotechnical Institute (NGI) Oslo, [c]Polytec Research Institute, Haugesund, Norway

Corresponding author's e-mail address: lamechoo@mail.uio.no

Keywords Vp –Vs relation, imbibition, drainage.

ABSTRACT

Subsurface storage of CO_2 is considered to have a large potential to mitigate and reduce anthropogenic CO_2 emission. Some of the best candidates for large scale CO_2 storage includes saline aquifers and depleted hydrocarbon reservoirs. Several laboratory-based studies have been carried out in recent years to find the influence of CO_2 on the acoustic properties of reservoir rocks including Lei and Xue (2009), Nakagawa et al. (2013) and Siggins et al. (2010). They show that Gassmann's prediction of both P- and S-wave velocities during fluid substitution can be proven by experimental results. The success of CCS (Carbon Capture and Storage) technique depends, among other thing on, storage capacity and injectivity of CO_2 without any leakage to the surface. Indirect geophysical monitoring can provide information about the CO_2 behavior including distribution, migration and change in saturation (Kitamura et al., 2014), and estimate the CO_2 storage volume in a given reservoir.

In this experimental study, we investigate the potential of seismic techniques for monitoring and quantifying saturation changes in the space-time domain for CO_2 reservoirs by simulating 1 km deep reservoir with a pore pressure of 10 MPa using three well-known sandstones: Berea, Red Wildmoor and Gres des Vosges. The experiment protocol comprises of mechanical loading phase, succeeded by a CO_2 drainage and imbibition phase. The inherent and stress-induced material anisotropy, the effect of pore fluid composition, as well as the dynamic changes during CO_2 drainage and imbibition are quantified, mechanically and in terms of rock physical signatures. The experimental laboratory investigations are conducted in a hydrostatic pressure vessel (Fig. 1c) with a confining pressure of 25 MPa. Pressure sensors measure confining pressures and pore pressures, and Linear Variable Differential Transformer (LVDT) mounted directly onto the nitrile sleeve with an array of P- and S-wave piezo-ceramic crystals embedded at three different levels across the length in order to measure velocity both in axial and radial directions (Fig. 1d). The pore pressure is controlled using an ISCO™ pump. To avoid dropping in pressure during drainage, we used a GDS pump for maintaining backpressure.

Prior to CO_2 injection, the samples underwent cyclic hydrostatic loading from 1MPa to 15 MPa for dry, fully CO_2 saturated, and fully brine saturated conditions to characterize the mechanical properties. During both drainage and imbibition, we use a flow rate of 0.5 ml/min from 0 pore volume (PV) to 1 PV in 0.2 PV steps and increased the flow rate to 2.5 ml/min from 2 PV to 8 PV in 2 PV steps. Liquid CO_2 was injected from top of the sample during drainage while brine was injected from the bottom during imbibition to avoid gravity segregation. During both drainage and imbibition, axial Vs does not change much and this is attributed to non-response nature of Vs during fluid substitution. The axial Vp decreases from 0-1 PV then flattens out during drainage while bottom and middle radial Vp sensors record drastical decrease from 0-1 PV then stabilizes up to 8 PV as compared to top Vp sensor. In the imbibition phase, the axial Vp increases gradually with the greatest increment occurring

between 2-9 PV. For the radial Vp, all the three (top, middle and bottom) measurements are more or less stable between 0-1 PV. Bottom Vp increases most between 1 and 4 PV as compared to the rest then stabilizes up to 9 PV.

From our experimental results, we clearly see opposite tendencies in Vp and Vs during drainage and imbibition. The acoustic P-wave velocities decreases during drainage (Figs. 1a and 1b) due to negative change in bulk modulus and density as a result of pore fluid substitution (brine to CO_2) and this is in agreement with Gassmann's prediction (Gassmann, 1951). According to Mavko et al. (1995), presence of reservoir fluid is identified on seismic data using relationships between the P- and S-wave arrival times and attenuation. At the end of imbibition, Vp does not recover fully to a pre-drainage due to the effect of residual trapped CO_2. These results are consistent with previous studies on Vp-Vs relation suggested by Han et al. (1986) and Kitamura et al. (2014). By analyzing the experimental data, we can clearly see the effect of injected CO_2 on the formation, which should be critical in interpreting geophysical field data in practice including mapping its distribution.

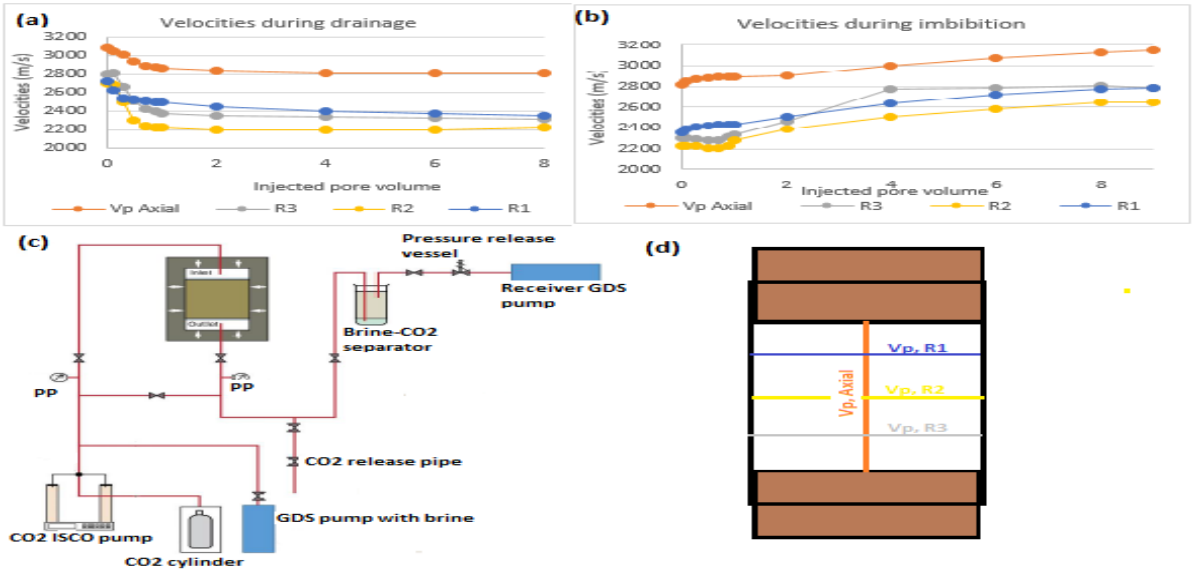

Figure 1: a) Measured velocities during drainage, (b) Measured velocities during imbibition. (c) Experimental setup and (d) schematic diagram showing measurement direction, R1, R2 and R3 refers to Vp measurements at the top, middle and bottom respectively.

ACKNOWLEDGEMENTS

We appreciate the support from SUCCESS FME centre for CO2 storage under grant 193825/S60 from Research Council of Norway (RCN). We also thank for the financial and scientific contributions from NGI GBV Project 20120265.

REFERENCES

BACHU, S. 2000. Sequestration of CO2 in geological media: Criteria and approach for site selection in response to climate change. *Energy Conversion and Management,* 41**,** 953-970.

GASSMANN, F. 1951. *Uber die Elastizitat poroser Medien,* Zurich, Vierteljahrsschrift der Naturforschenden Gesellschaft.

HAN, D.-H., NUR, A. & MORGAN, D. 1986. Effects of porosity and clay content on wave velocities in sandstones. *Geophysics,* 51**,** 2093-2107.

KITAMURA, K., XUE, Z., KOGURE, T. & NISHIZAWA, O. 2014. The potential of Vs and Vp–Vs relation for the monitoring of the change of CO2-saturation in porous sandstone. *International Journal of Greenhouse Gas Control,* 25**,** 54-61.

LEI, X. & XUE, Z. 2009. Ultrasonic velocity and attenuation during CO2 injection into water-saturated porous sandstone: Measurements using difference seismic tomography. *Physics of the Earth and Planetary Interiors,* 176**,** 224-234.

MAVKO, G., MUKERJI, T. & GODFREY, N. 1995. Predicting stress-induced velocity anisotropy in rocks. *Geophysics,* 60**,** 1081-1087.

NAKAGAWA, S., KNEAFSEY, T. J., DALEY, T. M., FREIFELD, B. M. & REES, E. V. 2013. Laboratory seismic monitoring of supercritical CO2 flooding in sandstone cores using the Split Hopkinson Resonant Bar technique with concurrent x-ray Computed Tomography imaging. *Geophysical Prospecting,* 61**,** 254-269.

SIGGINS, A. F., LWIN, M. & WISMAN, P. 2010. Laboratory calibration of the seismo-acoustic response of CO2 saturated sandstones. *International Journal of Greenhouse Gas Control,* 4**,** 920-927.

3. Tracking CO_2 front development with electrical resistivity measurements-an experimental study

T. Tran[1], L.O. Omolo[1], M. Soldal[2], N.H. Mondol[1,2], J. Park[2] and Ø. Johnsen[3]

[1]Department of Geosciences, University of Oslo, P.O. Box 1047 Blindern, 0316 Oslo [2]Norwegian Geotechnical Institute (NGI), P.O. Box 3930 Ullevål Stadion, 0806 Oslo [3]Polytec Research Institute, Sørhauggata 128, 5527 Haugesund, Norway

Corresponding author's e-mail address: truongxt@student.geo.uio.no

Keywords: CO2, resistivity, monitoring

ABSTRACT

Subsurface storage of carbon dioxide (CO_2) is considered to be a possible solution to reduce atmospheric CO_2 emissions and to mitigate global warming. Saline aquifers and depleted hydrocarbon reservoirs can be good candidates for storing large amount of CO_2. Due to the variable depths of possible geological storage of CO_2, direct monitoring of change in the fluid properties is not feasible. Several authors (e.g. Alemu et al., 2013; Onishi et al., 2006; Xue et al., 2009) have studied electrical resistivity monitoring as an indirect method that could help to detect saturation changes of CO_2 storage reservoirs. In this experimental study, resistivity changes during injection of both liquid CO_2 and brine (30g/l NaCl) are measured across and at three different locations along a sandstone core plug (Gres des Vosges Sandstone from France). The tested core plug has an average porosity of 20% and the height and diameter are 79 mm and 38 mm respectively.

The experiment is conducted in a hydrostatic pressure vessel in which the confinement pressure is hydraulically controlled by a pressure controller to keep it at 25MPa. The sandstone core plug is placed inside a nitril rubber sleeve with mounted LVDT for radial and axial strain measurement, and possibility of measuring resistance in the axial and three radial positions (top, middle and bottom of the sample shown in Fig**.** 9a. To avoid gravity segregation, liquid CO_2 is injected from the top of the sample and during imbibition brine is injected from the bottom (Fig**.** 9b). Both liquids are pressurized to 10 MPa, and volumes corresponding to a certain number of pore volumes (0.1, 0.3, 0.5, 0.7, 0.9, 1.0, 2.0, 4.0, 6.0, 8.0, 9.0 and 10 PV) are injected and subsequent measurements of electrical resistivity are made. For 0-1 PV and 1-10 PV the injection rate were set at 0.5 mL/min and 2.5 mL/min respectively.

The measured electrical resistivity during drainage and imbibition are shown in Fig**.** 9c and 1d. The axial resistivity increases steadily until 9 PV during drainage, while it decreases until 4 PV during brine imbibition. The radial resistivity measurements are able to detect the CO_2 front during drainage; a resistivity increase is first seen at the sensor nearest the injection point and then gradually towards the outlet. During imbibition resistivity decreases for bottom (brine inlet) and middle part at 0.1 PV injected while for the top it is at 0.2 PV. After 10 PV of brine imbibition the measured resistivity is approximately as it was at the start of drainage.

From our experimental study, we conclude the electrical resistivity method and sensor array configuration is a handy tool to track development of CO_2 front during CO_2 injection. The flow rate influences the saturation of CO_2 as the resistivity development before and after 1 PV does not match (Fig**.** 9c). Imbibition of 0.2 PV brine is enough to decrease the resistivity by about 70%, but pushing the remaining CO_2 out requires injection of several pore volumes of brine. The change in flow rate

does not seem to have a big impact during imbibition due to the gravity effect. More work will be done in this study on sandstones with varying anisotropy focusing more closely on the effects of injection rate.

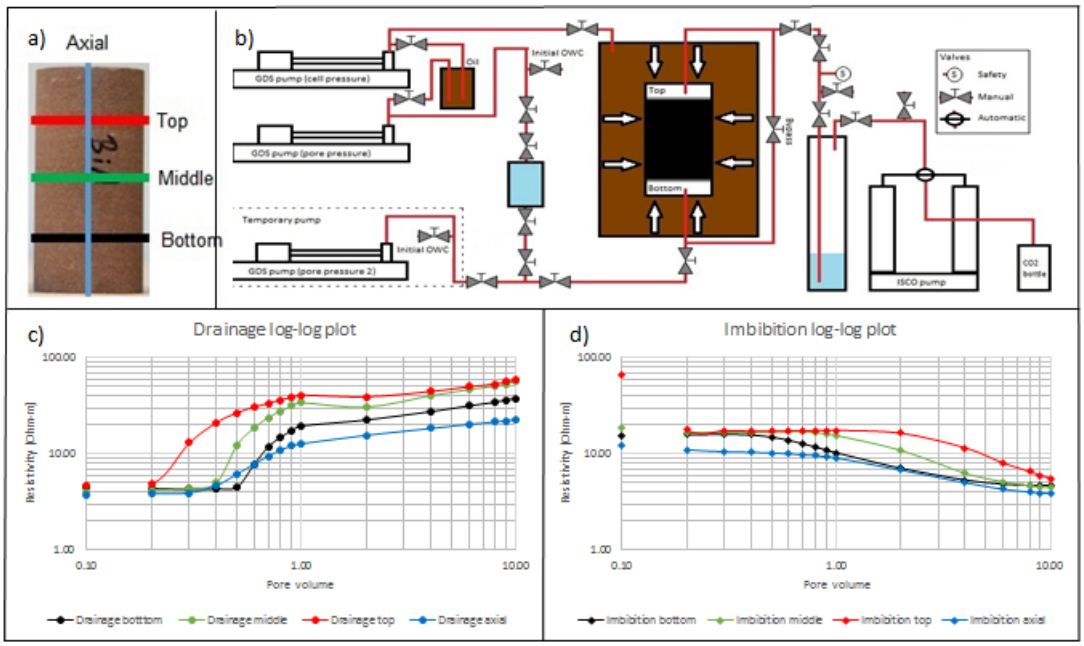

Fig. 9: a) Gres des Vosges Sandstone core plug, b) Experimental set up, c) Measured electrical resistivity during drainage of CO2 and d) Measured electrical resistivity during imbibition of brine.

ACKNOWLEDGEMENTS

We appreciate the support from SUCCESS FME centre for CO2 storage under grant 193825/S60 from Research Council of Norway (RCN). We also thank for the financial and scientific contributions from NGI GBV Project 20120265.

REFERENCES

Alemu, B. L., Aker, E., Soldal, M., Johnsen, Ø., and Aagaard, P., 2013, Effect of sub-core scale heterogeneities on acoustic and electrical properties of a reservoir rock: a CO2 flooding experiment of brine saturated sandstone in a computed tomography scanner: Geophysical Prospecting, v. 61, no. 1, p. 235-250.

Onishi, K., Ishikawa, Y., Yamada, Y., and Matsuoka, T., 2006, Measuring Electric Resistivity of Rock Specimens Injected With Gas, Liquid And Supercritical CO2, Society of Exploration Geophysicists.

Xue, Z., Kim, J. W., Mito, S., Kitamura, K., and Matsuoka, T., 2009, Detecting and Monitoring CO2 With P-Wave Velocity and Resistivity From Both Laboratory and Field Scales, Society of Petroleum Engineers.